Fall 11-15-2016

Fokker-Planck-Based Acceleration for SN Equations with Highly Forward Peaked Scattering in Slab Geometry

Japan K. Patel
University of New Mexico

Japan Patel

Candidate

Nuclear Engineering

Department

This dissertation is approved, and it is acceptable in quality and form for publication:

Approved by the Dissertation Committee:

Dr. Anil Prinja , Chairperson

Dr. James Warsa

Dr. Gary Cooper

Dr. Mohammad Motamed

Fokker-Planck-Based Acceleration for S_N Equations with Highly Forward Peaked Scattering in Slab Geometry

by

Japan Patel

H.B.S., Nuclear Engineering, Oregon State University, 2011

M.S., Nuclear Engineering, University of New Mexico, 2014

DISSERTATION

Submitted in partial fulfillment of the

Requirements for the Degree of

Doctor of Philosophy

Engineering

The University of New Mexico

Albuquerque, New Mexico

December, 2016

Dedication

To my parents and grandparents.

Acknowledgements

At this point, I would like to thank Dr. Anil Prinja and Dr. Jim Warsa for their patience and constant support. Their advise is invaluable and discussion with them are always enlightening. This dissertation would have been impossible without them.

I would like to thank Dr. Gary Cooper and Dr. Mohammad Motamed for being on my committee and for their patience with me.

I would like to Dr. Barry Ganapol. Discussions with him were very informative and fun. I'm lucky to have had the opportunity to talk to him about transport and convergence acceleration.

My friend, Dr. David Dixon, was my first charged particle transport teacher. Thank you very much for introducing me to transport problems with anisotropic scattering and the Fokker-Planck equation. Thank you, Eric Benner, for helping me with LaTex.

I would like to thank Dr. Cassiano de Oliveira, Dr. Ryosuke Park, Dr. Salvador Rodriguez, Dr. Patrick McDaniel, Dr. Adam Hecht, Dr. Dimiter Petsev, Dr. Todd Palmer, Dr. Andrew Klein, Dr. Qiao Wu, Dr. Elena Paulinova, Mr. Todd Keller, Mrs. Vandana Gajjar, Mr. Pinak Vyas, Mr.

Ashutosh Pandya, Mr. Kandarp Shah, Mr. Parth Tank and all my other teachers and professors that have taught me something throughout the course of my existence so far.

I would also like to thank all the previous researchers in the fields of mathematics and transport whose research made this work possible.

I would like to thank my parents, Mohna and Ketan Patel. Words can't describe my gratitude.

Fokker-Planck-Based Acceleration for S_N Equations with Highly Forward Peaked Scattering in Slab Geometry

by

Japan Patel

H.B.S., Nuclear Engineering, Oregon State University, 2011

M.S., Nuclear Engineering, University of New Mexico, 2014

PhD, Engineering, University of New Mexico, 2016

Abstract

Short mean free paths are characteristic of charged particles. High energy charged particles often have highly forward peaked scattering cross sections. Transport problems involving such charged particles are also highly optically thick. When problems simultaneously have forward peaked scattering and high optical thickness, their solution, using standard iterative methods, becomes very difficult and inefficient. In this dissertation, we explore Fokker-Planck-based acceleration for solving such problems.

Keywords: Charged particle transport, highly anisotropic scattering, synthetic acceleration, Fokker-Planck

Contents

List of Figures

List of Tables

Chapter 1

Introduction

Modeling of transport with forward-peaked scattering operators is encountered in several applications related to plasma physics, radiation shielding, X-ray machine design, astrophysics etc. [7]. Such problems are characterized by extremely small mean free paths with nearly singular differential scattering cross sections in the forward direction. The energy loss per collision is also very small [7]. The discrete ordinates method [19] is quite accurate in modeling such transport problems but these physical characteristics render convergence of standard iterative procedures arbitrarily slow [32].

Standard acceleration techniques to improve convergence such as diffusion synthetic acceleration (DSA) [2] and nonlinear diffusion acceleration (NDA) [5] are quite ineffective in accelerating such problems with forward-peaked scattering due to their inability to accurately model higher order error moments with significant magnitudes [32]. When we accelerate such problems with DSA, we assume that any error moment higher than the first moment is zero even when the error moment is actually nonzero. This is as good as not accelerating the higher moments. Such acceleration methods are ineffective [32].

Standard synthetic acceleration [14] techniques essentially break the solution down into higher-order transport sweep [19], and a lower-order error-correction solve [1]. Sometimes, the scheme is broken down into several stages where the first stage is still the higher-order transport sweep but the error-correction stage is broken down into several sub-stages [18, 1]. In this dissertation, we will develop and test a synthetic acceleration method - Fokker-Planck synthetic acceleration (FPSA) - where the lower-order approximation (Fokker-Planck) for the error-correction stage is obtained using asymptotic analysis [3, 30, 26]. We call this approach of acceleration asymptotics-based acceleration.

1.1 Literature Review

Attempts have been made in the past to accelerate such problems primarily keeping electrons transport as the subject of convergence acceleration. In 1988, Valougeorgis, Williams, and Larsen [32] presented their work on stability analysis of P_L acceleration schemes applied to anisotropic neutron transport problems. The cross sections used in this paper were fictitious but the paper presented a framework for theoretical development and testing of future methods to accelerate transport problems with anisotropic scattering.

Morel and Manteuffel presented their angular multigrid method for solution of problems with high anisotropy in [24]. The angular multigrid method proved to be effective in 1D with a maximum spectral radius of 0.6. The method however had to be modified later to preserve stability for problems with higher spatial dimensions [31]. Pautz, Morel, and Adams modified this method to preserve stability in [25] and extended the angular multigrid method to 2D. Turcksin and Morel

integrated diffusion synthetic acceleration and angular multigrid to develop their diffusion synthetic acceleration-angular multigrid method in [31].

Khattab and Larsen presented with their modified P_L acceleration method that used a modified form of P_L equations with modified scattering cross section moments in [13]. Very few other famous attempts have been noted to accelerate the solution of such problems with high anisotropy.

Several innovations have been made to approximate the transport equation such that a fair amount of accuracy is preserved. Most prominent of these is the Fokker-Planck approximation. The Fokker-Planck approximation assumes extremely forward-peaked scattering with small scattering angles and energy loss. Under such conditions, Fokker-Planck equation is an asymptotic limit of the Boltzmann equation [26].

Renormalization techniques [3] are applied for generating higher order approximations to the scattering operator in the Fokker-Planck limit. These equations, with higher order truncations, are called Generalized-Fokker-Planck equations (GFP). Several authors - Pomraning, Prinja, Larsen, Leakes have presented their work on this approximation in [27, 30, 17].

Boltzmann-Fokker-Planck (BFP) approximation can model forward-peaked scattering fairly well [15]. The BFP approximation decomposes the scattering kernel into smooth and singular parts [7]. After decomposing the scattering kernel into smooth and singular components, we model the smooth component using Legendre expansion and singular component using Fokker-Planck. This method has proven to be quite useful [7]. It is tricky to choose the optimal decomposition [31]. One may use data-mining algorithms to train a model to choose the right decomposition given a

specific set of scattering cross-section data.

1.2 Basic Idea and Purpose

It is noteworthy that problems with forward-peaked scattering kernels require acceleration of all relevant moments. This calls for an acceleration scheme that accelerates the angular flux itself. We need a good low-order approximation for the angular flux. For problems that are highly forward-peaked, the Fokker-Planck approxmation can be good. Therefore, we want to use Fokker-Planck as a preconditioner. In this dissertation, we will introduce the idea of Fokker-Planck Synthetic Acceleration (FPSA) and evaluate its effectiveness.

In the next chapter, we introduce the transport equation and the Fokker-Planck equation. In Ch. 3, we introduce the idea of acceleration and describe the FPSA method. In Ch. 4, we will discuss angularly discrete Fourier analysis for FPSA, and its numerical implementation. In Ch. 5 we present numerical experiments. Finally, we will conclude with Ch. 6.

Chapter 2

Transport Equation

Modeling of distribution of radiation in physical systems begins with development of a general mathematical framework. Transport theory provides this framework via transport equation. The transport equation was first derived by Ludwig Boltzmann more than a century ago. The equation was used to describe the kinetic behavior of gases, and is still used for that purpose. The same equation is used describe the transport of neutral and charged particles.

This integro-differential equation accounts for the number of particles entering, number of particles leaving, the number of particles created, and the number of particles extinguished (absorbed) in the phase-space volume of interest over time. Analytical solution of the transport equation is not possible in most realistic situations. Numerical solution methods are usually employed. The solution of this equation can require a significant amount of computational effort and mathematical skill as its solution can be a complex function of seven independent variables space (3), direction (2), time (1) and energy (1). In this chapter, we introduce the transport equation in slab geometry, standard source iteration to solve the transport equation, and synthetic acceleration for source iteration. We will also present Fourier analysis for source iteration and see how it can be arbitrarily

slow to converge.

2.1 Transport Equation in Slab Geometry

In this section, we will introduce the steady state, slab geometry, one group, fixed source, transport equation with anisotropic scattering. This equation, even in its reduced form, is a 2D equation with dependence on space and angle. Several standard derivations of the transport equation and its reduction to the desired form exist [19, 29]. We begin by writing the transport equation in its full 7D form [29]:

$$\begin{aligned} &\frac{1}{v}\frac{\partial\psi(\overline{r},\hat{\Omega},E,t)}{\partial t} + \hat{\Omega}.\overline{\nabla}\psi(\overline{r},\hat{\Omega},E,t) + \sigma_t(\overline{r},E,t)\psi(\overline{r},\hat{\Omega},E,t) \\ &= Q(\overline{r},\hat{\Omega},E,t) + \int_0^{\infty} dE' \int_0^{4\pi} d\Omega' \sigma_s(\overline{r},\hat{\Omega}'.\hat{\Omega},E'\rightarrow E,t)\psi(\overline{r},\hat{\Omega}',E,t) \end{aligned} \tag{2.1}$$

Here, t represents time. E and E' represent initial and after-scatter energies of the particle respectively. Particle position in space is represented by $\overline{r}$, and $\hat{\Omega}$ and $\hat{\Omega}'$ are the initial and after-scatter unit vectors in directions of flight respectively. Further, $\hat{\Omega}$ and $\hat{\Omega}'$ are characterized by azimuthal angle, ω, and cosine of polar angle, μ on the unit sphere. We represent external source by Q. Here, ψ is the angular flux which represents the total number of particles per unit phase space element. The phase space element is characterized by a volume dV about position $\overline{r}$, cone of directions $d\Omega$ about $\hat{\Omega}$, energy dE between E and $E+dE$, and time dt between t and dt. The units of angular flux are $\frac{particles}{eV.Sr.cm^2.s}$. Finally, the total and scattering cross sections have been represented by $\sigma_t(\overline{r},E,t)$ and $\sigma_s(\overline{r},\hat{\Omega}'.\hat{\Omega},E'\rightarrow E,t))$ respectively.

In order to reduce the transport equation to its steady state form, we let the rate of change of angular flux be zero. Therefore, the above equation becomes:

$$\hat{\Omega}.\overline{\nabla}\psi(\overline{r},\hat{\Omega},E)+\sigma_t(\overline{r},E)\psi(\overline{r},\hat{\Omega},E)=Q(\overline{r},\hat{\Omega},E)$$
$$+\int_0^{\infty}dE'\int_0^{4\pi}d\Omega'\sigma_s(\overline{r},\hat{\Omega}'.\hat{\Omega},E'\rightarrow E)\psi(\overline{r},\hat{\Omega}',E) \tag{2.2}$$

We get the mono-energetic transport equation by assuming that all scattering interactions are elastic and that the kinetic energy of particles does not change after scattering. Mathematically, this is represented by introduction of a delta function in the representation of quantities defined in the above equation as [29]:

$$\sigma_s(\overline{r},\hat{\Omega}'.\hat{\Omega},E\rightarrow E') = \sigma_s(\overline{r},\hat{\Omega}'.\hat{\Omega})\delta(E'-E_0), \tag{2.3}$$

$$Q(\overline{r},\hat{\Omega},E) = Q(\overline{r},\hat{\Omega})\delta(E-E_0), \tag{2.4}$$

$$\psi(\overline{r},\hat{\Omega},E) = \psi(\overline{r},\hat{\Omega})\delta(E-E_0). \tag{2.5}$$

Here, E_0 is the characteristic energy of the particle. Upon application of the definitions above, we obtain the following monoenergetic, steady state transport equation:

$$\hat{\Omega}.\overline{\nabla}\psi(\overline{r},\hat{\Omega},E_0)+\sigma_t(\overline{r},E_0)\psi(\overline{r},\hat{\Omega},E_0)=Q(\overline{r},\hat{\Omega},E_0)$$
$$+\int_0^{4\pi}d\Omega'\sigma_s(\overline{r},\hat{\Omega}'.\hat{\Omega},E_0)\psi(\overline{r},\hat{\Omega}',E_0) \tag{2.6}$$

Further, we drop E_0 from the above equation since it is invariant for a given calculation to obtain:

$$\hat{\Omega}.\overline{\nabla}\psi(\overline{r},\hat{\Omega})+\sigma_t(\overline{r})\psi(\overline{r},\hat{\Omega})=Q(\overline{r},\hat{\Omega})$$
$$+\int_0^{4\pi}d\Omega'\sigma_s(\overline{r},\hat{\Omega}'.\hat{\Omega})\psi(\overline{r},\hat{\Omega}') \tag{2.7}$$

In most cases, scattering is assumed to be rotationally invariant. Moreover, since the scattering cross-section depends on $\mu_0=\hat{\Omega}'.\hat{\Omega}$, we can write scattering cross-section in Legendre polynomial expansion as:

$$\sigma_s(\overline{r},\mu_0) = \sum_{l=0}^{L} \frac{2l+1}{4\pi}\sigma_{s,l}P_l(\mu_0), \tag{2.8}$$

where, $\sigma_{s,l}$ is the l^{th} moment of the scattering cross-section:

$$\sigma_{s,l} = \int_{-1}^{1} d\mu_0 \sigma_s(\mu_0)P_l(\mu_0), \tag{2.9}$$

with, $P_l(\mu_0)$ is the l^{th} order Legendre polynomial, L is the order of expansion. For exact representation of the scattering cross-section, $L = \infty$. The Legendre polynomials are represented using spherical harmonics as:

$$P_l(\mu_0) = \frac{4\pi}{2l+1} \sum_{m=-l}^{l} Y_{l,m}(\hat{\Omega})Y^*_{l,m}(\hat{\Omega}'). \tag{2.10}$$

Here $*$ denotes the complex conjugate. For $0 \leq |m| \leq l < \infty$, the spherical harmonic function $Y_{l,m}(\hat{\Omega})$ is written using the associated Legendre polynomials as [29]:

$$Y_{l,m}(\hat{\Omega}) = Y_{l,m}(\mu,\omega) = a_{l,m}P_l^{|m|}(\mu)e^{im\omega}. \tag{2.11}$$

Here, $P_l^{|m|}(\mu)$ is the associated Legendre polynomial:

$$P_l^{|m|}(\mu) = (1-\mu^2)^{\frac{|m|}{2}} \left(\frac{d^{|m|}}{d^{|m|}\mu}\right) P_l(\mu), \tag{2.12}$$

with,

$$a_{l,m} = (-1)^{\frac{m+|m|}{2}} \left(\frac{2l+1}{4\pi}\frac{(l-|m|)!}{(l+|m|)!}\right). \tag{2.13}$$

Therefore, we rewrite the scattering cross sections in spherical harmonics as:

$$\sigma_s(\overline{r},\mu_0) = \sum_{l=0}^{L} \sum_{m=-l}^{l} \sigma_{s,l}Y_{l,m}(\hat{\Omega})(\overline{r})Y^*_{l,m}(\hat{\Omega}'), \tag{2.14}$$

Likewise, the scattering integral can be rewritten as:

$$\int_0^{4\pi} d\Omega' \sigma_s(\overline{r}, \hat{\Omega}'.\hat{\Omega})\psi(\overline{r}, \hat{\Omega}) = \int_0^{4\pi} d\Omega' \sum_{l=0}^{L} \sum_{m=-l}^{l} \sigma_{s,l} Y_{l,m}(\hat{\Omega}) Y_{l,m}^*(\hat{\Omega}')\psi(\overline{r}, \hat{\Omega}') \tag{2.15}$$

Rearranging the above equation and rewriting the integral in terms of polar and azimuthal components returns:

$$\int_0^{4\pi} d\Omega' \sigma_s(\overline{r}, \hat{\Omega}'.\hat{\Omega})\psi(\overline{r}, \hat{\Omega}) = \sum_{l=0}^{L} \sum_{m=-l}^{l} \sigma_{s,l} Y_{l,m}(\hat{\Omega}) \int_{-1}^{1} \int_0^{2\pi} d\omega' d\mu' Y_{l,m}^*(\hat{\Omega}')\psi(\overline{r}, \hat{\Omega}') \tag{2.16}$$

Now, assuming cartesian coordinates, we have:

$$\begin{aligned}
\overline{r} &= x\hat{i} + y\hat{j} + z\hat{k}, && (2.17)\\
\hat{\Omega} &= \Omega_x\hat{i} + \Omega_y\hat{j} + \Omega_z\hat{k}, && (2.18)\\
&= \sqrt{1-\mu^2}(cos\omega\hat{i} + sin\omega\hat{j} + \mu\hat{k}, && (2.19)\\
d\Omega &= d\mu d\omega. && (2.20)
\end{aligned}$$

Then, we may write the streaming term of the transport equation as:

$$\hat{\Omega}.\overline{\nabla}\psi(\overline{r}, \hat{\Omega}) = \left(\Omega_x \frac{\partial}{\partial x} + \Omega_y \frac{\partial}{\partial y} + \Omega_z \frac{\partial}{\partial z}\right) \psi(x, y, z, \mu, \omega). \tag{2.21}$$

Substituting the definition of the streaming term from Eq. (2.21), and Eq. (2.17) along with the definition of scattering integral from Eq. (2.16) in Eq. (2.6), we obtain the following equation:

$$\begin{aligned}
&\left[\sqrt{1-\mu^2}\left(cos\omega\frac{\partial}{\partial x} + sin\omega\frac{\partial}{\partial y}\right) + \mu\frac{\partial}{\partial z}\right]\psi(x, y, z, \mu, \omega) + \sigma_t(x, y, z)\psi(x, y, z, \mu, \omega)\\
&= \sum_{l=0}^{L} \sum_{m=-l}^{l} \sigma_{s,l} Y_{l,m}(\hat{\Omega}) \int_{-1}^{1} \int_0^{2\pi} d\omega' d\mu' Y_{l,m}^*(\hat{\Omega}')\psi(x, y, z, \mu', \omega') + Q(x, y, z, \mu, \omega).
\end{aligned} \tag{2.22}$$

Now, we reduce the above equation to a 1D equation, in space, by assuming the system to be a planar slab with finite dimensions only along the z direction. This returns the following equation [29]:

$$\mu\frac{\partial\psi}{\partial z}(z,\mu,\omega)+\sigma_t(z)\psi(z,\mu,\omega)=\sum_{l=0}^{L}\sum_{m=-l}^{l}\sigma_{s,l}Y_{l,m}(\hat{\Omega})\int_{-1}^{1}\int_{0}^{2\pi}d\omega' d\mu' Y^*_{l,m}(\hat{\Omega}')\psi(z,\mu',\omega')+Q(z,\mu,\omega). \tag{2.23}$$

Finally, in order to obtain the steady state, slab geometry, one-group, fixed source transport equation, we assume azimuthal symmetry. We eliminate the azimuthal angle dependence by integrating Eq. (2.23) over $0 \leq \omega \leq 2\pi$. Therefore,

$$\int_0^{2\pi} d\omega \left(\mu\frac{\partial\psi}{\partial z}(z,\mu,\omega)+\sigma_t(z)\psi(z,\mu,\omega)=\sum_{l=0}^{L}\sum_{m=-l}^{l}\sigma_{s,l}Y_{l,m}(\hat{\Omega})\int_{-1}^{1}\int_{0}^{2\pi}d\omega' d\mu' Y^*_{l,m}(\hat{\Omega}')\psi(z,\mu',\omega')+Q(z,\mu,\omega)\right), \tag{2.24}$$

returns:

$$\mu\frac{\partial\psi}{\partial z}(z,\mu)+\sigma_t(z)\psi(z,\mu)=\sum_{l=0}^{L}\sum_{m=-l}^{l}\sigma_{s,l}\int_0^{2\pi}d\omega Y_{l,m}(\hat{\Omega})\int_{-1}^{1}\int_{0}^{2\pi}d\omega' d\mu' Y^*_{l,m}(\hat{\Omega}')\psi(z,\mu',\omega')+Q(z,\mu). \tag{2.25}$$

Now using Eq. (2.11) we have,

$$\begin{aligned}\int_0^{2\pi} d\omega Y_{l,m}(\hat{\Omega}) &= \int_0^{2\pi} d\omega a_{l,m}P_l^{|m|}(\mu)e^{im\omega} &(2.26)\\ &= 2\pi\left(\frac{2l+1}{4\pi}\right)^{\frac{1}{2}}P_l(\mu)\delta_{m,0}. &(2.27)\end{aligned}$$

Evaluating the double integral in Eq. (2.25) and restricting m to 0 because of azimuthal symmetry, we have:

$$\int_{-1}^{1}\int_{0}^{2\pi} d\omega' d\mu' Y_{l,m}^{*}(\hat{\Omega}')\psi(z,\hat{\Omega}') = \int_{-1}^{1}\int_{0}^{2\pi} d\omega' d\mu' Y_{l,0}^{*}(\hat{\Omega}')\psi(z,\hat{\Omega}') \quad (2.28)$$

$$= \int_{-1}^{1}\int_{0}^{2\pi} d\omega' d\mu' \left(\frac{2l+1}{4\pi}\right)^{\frac{1}{2}} P_l(\mu')\psi(z,\mu',\omega') \quad (2.29)$$

$$= \left(\frac{2l+1}{4\pi}\right)^{\frac{1}{2}} \int_{-1}^{1} d\mu' P_l(\mu')\psi(z,\mu'). \quad (2.30)$$

Now substituting Eq. (2.27) and Eq. (2.30) in Eq. (2.25), we obtain the following final slab geometry equation:

$$\mu\frac{\partial\psi(z,\mu)}{\partial z} + \sigma_t(z)\psi(z,\mu) = \sum_{l=0}^{L}\frac{2l+1}{2}P_l(\mu)\sigma_{s,l}(z)\phi_l(z) + Q(z,\mu), \quad (2.31)$$

where, $\phi_l(z)$ are the moments of angular flux:

$$\phi_l(z) = \int_{-1}^{1} d\mu' P_l(\mu')\psi(z,\mu'). \quad (2.32)$$

In order to write the steady-state, mono-energetic, slab geometry transport equation in its continuous, integro-differential form, we go back to Eq. (2.7). Noting that $\overline{r}$ will reduce to z, $\hat{\Omega}$ will reduce to μ and $\hat{\Omega}.\hat{\Omega}'$ will reduce to μ_0. The integration limits will transform to -1 and 1 from 0 and 4π, we write the exact slab geometry equation as:

$$\mu\frac{\partial\psi(z,\mu)}{\partial z} + \sigma_t(z)\psi(z,\mu) = 2\pi\int_{-1}^{1} d\mu'\sigma_s(\mu_0)\psi(z,\mu') + Q(z,\mu), \quad (2.33)$$

2.2 Source Iteration

Source iteration is one of the most basic iterative method used to solve the S_N equations. It is equivalent to Richardson iteration. In order to describe source iteration [1, 19, 33], we begin by rewriting the transport equation, Eq. (2.31), in its operator form:

$$L\psi(z,\mu) = S\psi(z,\mu) + q(z,\mu) \tag{2.34}$$

where,

$$L = \mu\frac{\partial}{\partial z} + \sigma_t(z), \tag{2.35}$$

$$S = \sum_{l=0}^{L} \frac{(2l+1)}{2} P_l(\mu)\sigma_{s,l}(z) \int_{-1}^{1} d\mu' P_l(\mu'), \tag{2.36}$$

and,

$$q(z,\mu) = \frac{Q(z,\mu)}{2}. \tag{2.37}$$

We will now lag the angular flux in the scattering term on the right hand side of the transport equation by one iteration and iterate until the relevant Legendre moments of angular flux converge in the L_∞ norm (L_2 norm can also be chosen without any loss of generality). We have the following equation:

$$L\psi^{m+1}(z,\mu) = S\psi^{m}(z,\mu) + q(z,\mu), \tag{2.38}$$

which can be rewritten as:

$$\psi^{m+1}(z,\mu) = L^{-1}S\psi^{m}(z,\mu) + L^{-1}q(z,\mu), \tag{2.39}$$

to see what source iteration exactly does. Source iteration can be shown to be equivalent to Richardson iteration [1]. We begin by applying L^{-1} to Eq. (2.38):

$$L^{-1}L\psi^{m+1}(z,\mu) = L^{-1}S\psi^{m}(z,\mu) + L^{-1}q(z,\mu). \tag{2.40}$$

Now, define new operators as follows:

$$A = I - L^{-1}S, \quad \text{and} \quad \hat{q}(z,\mu) = L^{-1}q(z,\mu). \tag{2.41}$$

Now using the definition in Eq. (2.41) with Eq. (2.40), we obtain:

$$\psi^{m+1}(z,\mu) = (I - A)\psi^{m}(z,\mu) + \hat{q}(z,\mu). \tag{2.42}$$

This is Richardson iteration for the problem, $A\psi(z,\mu) = q(z,\mu)$. Now, using Eq. (2.41), we know that $I - A = L^{-1}S$. This means we can rewrite Eq. (2.42) as Eq. (2.39) which represents source iteration. Therefore, we now know that source iteration and Richardson iteration are mathematically equivalent. Source iteration is a stationary method. One of the biggest flaws of this method is that it is slow to converge for thick, and diffusive problems with forward-peaked scattering kernels as we will now demonstrate using Fourier analysis.

2.2.1 Fourier Analysis for Source Iteration

We begin by subtracting Eq. (2.38) from Eq. (2.34). By doing so, we get the following error equation:

$$L\epsilon^{m+1}(z,\mu) = S\epsilon^{m}(z,\mu), \tag{2.43}$$

where, $\epsilon^{m}(z,\mu) = \psi(z,\mu) - \psi^{m}(z,\mu)$ is the error in the angular flux after m^{th} iteration. Now, we write out the operators in their full form to obtain:

$$\mu\frac{\partial\epsilon^{m+1}(z,\mu)}{\partial z} + \sigma_t(z)\epsilon^{m+1}(z,\mu) = \sum_{l=0}^{L}\frac{2l+1}{2}P_l(\mu)\sigma_{s,l}(z)\int_{-1}^{1}d\mu' P_l(\mu')\epsilon^{m}(z,\mu). \tag{2.44}$$

For analysis, we assume constant material properties. We drop spatial dependence of material cross-sections to obtain:

$$\mu\frac{\partial\epsilon^{m+1}(z,\mu)}{\partial z}+\sigma_t\epsilon^{m+1}(z,\mu)=\sum_{l=0}^{L}\frac{2l+1}{2}P_l(\mu)\sigma_{s,l}\int_{-1}^{1}d\mu' P_l(\mu')\epsilon^m(z,\mu). \tag{2.45}$$

Now, we separate the error components into their angle and space dependent components by writing $\epsilon^{m+1}(z,\mu)$ and $\epsilon^m(z,\mu)$ as Fourier integral [1]:

$$\epsilon^{m+1}(z,\mu)=\int_{-\infty}^{\infty}d\lambda\hat{\epsilon}_\lambda^{m+1}(\mu)e^{i\lambda\sigma_t z}, \tag{2.46}$$

where, λ is the wave number. Substituting this form of error into the error equation, Eq. (2.44), we get:

$$\int_{-\infty}^{\infty}d\lambda\left(\mu\frac{\partial\hat{\epsilon}_\lambda^{m+1}(\mu)e^{i\lambda\sigma_t z}}{\partial z}+\sigma_t\hat{\epsilon}_\lambda^{m+1}(\mu)e^{i\lambda\sigma_t z}=\sum_{l=0}^{L}\frac{2l+1}{2}P_l(\mu)\sigma_{s,l}\int_{-1}^{1}d\mu' P_l(\mu')\hat{\epsilon}_\lambda^{m}(\mu)e^{i\lambda\sigma_t z}\right). \tag{2.47}$$

Upon carrying out necessary simplifications and noting that Fourier modes, $e^{i\lambda\sigma_t z}$, are linearly independent for all λ, we obtain:

$$(1+i\lambda\mu)\sigma_t\hat{\epsilon}_\lambda^{m+1}(\mu)=\sum_{l=0}^{L}\frac{2l+1}{2}P_l(\mu)\sigma_{s,l}\int_{-1}^{1}d\mu' P_l(\mu')\hat{\epsilon}_\lambda^{m}(\mu) \tag{2.48}$$

We define l^{th} Legendre moment of angle-dependent component of error and l^{th} Legendre moment of error respectively as:

$$\hat{\epsilon}_l^m=\int_{-1}^{1}d\mu' P_l(\mu')\hat{\epsilon}_\lambda^m(\mu'),\epsilon_l^m \quad = \quad \int_{-1}^{1}d\mu' P_l(\mu')\epsilon^m. \tag{2.49}$$

Dropping λ and μ in notation of $\hat{\epsilon}$ in Eq. (2.48) for convenience, and using Eq. (2.49), we get:

$$(1+i\lambda\mu\sigma_t)\sigma_t\hat{\epsilon}^{m+1}=\sum_{l=0}^{L}\frac{2l+1}{2}P_l(\mu)\sigma_{s,l}\hat{\epsilon}_l^m. \tag{2.50}$$

Then, rearranging the equation and taking n^{th} Legendre moment of Eq. (2.50), we obtain the following:

$$\int_{-1}^{1} d\mu P_n(\mu)\hat{\epsilon}_{\lambda}^{m+1} = \int_{-1}^{1} d\mu P_n(\mu) \sum_{l=0}^{L} \frac{\sigma_{s,l}}{\sigma_t} \frac{2l+1}{2} \frac{P_l(\mu)}{1+i\lambda\mu\sigma_t} \hat{\epsilon}_l^m. \tag{2.51}$$

Further rearranging and using Eq. (2.49) in the above equation returns:

$$\hat{\epsilon}_l^{m+1} = \sum_{l=0}^{L} \frac{\sigma_{s,l}}{\sigma_t} \frac{2l+1}{2} \int_{-1}^{1} d\mu \frac{P_n(\mu)P_l(\mu)}{1+i\lambda\mu\sigma_t} \hat{\epsilon}_l^m. \tag{2.52}$$

We note that Eq. (2.52) represents the following matrix equation:

$$[\hat{\epsilon}_l^{m+1}] = A(\lambda)[\hat{\epsilon}_l^m], \tag{2.53}$$

where, $[\hat{\epsilon}_l^m]$ is a vector of scalar flux moment error at iteration m, and,

$$A(\lambda) = \sum_{l=0}^{L} \frac{\sigma_{s,l}}{\sigma_t} \frac{2l+1}{2} \int_{-1}^{1} d\mu \frac{P_n(\mu)P_l(\mu)}{1+i\lambda\mu\sigma_t}, \tag{2.54}$$

is the iteration matrix. We note that we can rewrite Eq. (2.53) in terms of the error in the first guess:

$$[\hat{\epsilon}_l^{m+1}] = A^m(\lambda)[\hat{\epsilon}_l^0]. \tag{2.55}$$

Now, we note that the absolute value of the maximum eigenvalue of the iteration matrix is called the spectral radius:

$$\rho(\lambda) = max(|\Lambda_l(A(\lambda)|), \tag{2.56}$$

where, $\Lambda_l(A(\lambda))$ are the eigenvalues of $A(\lambda)$ where $l = 1, 2, ..., L$. Spectral radius measures the upper bound of a consistent matrix norm of the iteration matrix [10].

$$\rho(\lambda) \geq ||(A(\lambda)||. \tag{2.57}$$

Using the Schwarz inequality [10] and Eq. (2.55) we note that the spectral radius of the iteration matrix, $A(\lambda)$, will dictate the convergence rate of the iterative scheme [1]. The spectral radius of the iterative method:

$$\rho = \max_{-\infty<\lambda<\infty} ||A(\lambda)|| \leq \max_{-\infty<\lambda<\infty} \rho(\lambda). \tag{2.58}$$

If spectral radius is greater than unity, the scheme is unstable. If it is 1 exactly unity, it will neither converge nor diverge. We see convergence when the spectral radius is less than unity.

Eigenvalues of the iteration matrix obtained above for $\lambda = 0$ are $\frac{\sigma_{s,l}}{\sigma_t}$ for $l = 0, 1, 2, ...$ Therefore, when scattering kernel is forward-peaked, the eigenvalues of the iteration matrix are close together, and slowly reducing. Moreover, as $\frac{\sigma_{s,l}}{\sigma_t}$ gets arbitrarily close to unity, the iterative method becomes arbitrarily slow to converge.

Example

Now that we have seen what Fourier analysis for source iteration returns, we look at an example in order to understand it further. Consider a problem with parameters given in Table 2.2.1. For this problem, the spectral radius lies at $\lambda = 0$ as seen in Fig. 2.2.1. The eigenvalues at $\lambda = 0$ are given in Table 2.2.1. We can see how the spectral radius is $\frac{\sigma_{s,0}}{\sigma_t}$ and eigenvalues at $\lambda = 0$ are $\frac{\sigma_{s,l}}{\sigma_t}$ as we saw during our analysis.

Parameter	Value
Legendre Expansion Order (L)	1
σ_t	1 cm^{-1}
$\sigma_{s,0}$	999/1000 cm^{-1}
$\sigma_{s,1}$	1/3 cm^{-1}

Table 2.1: Parameters for Fourier Analysis

Number	Eigenvalue
1	999/1000
2	1/3

Table 2.2: Eigenvalues for $\lambda = 0$

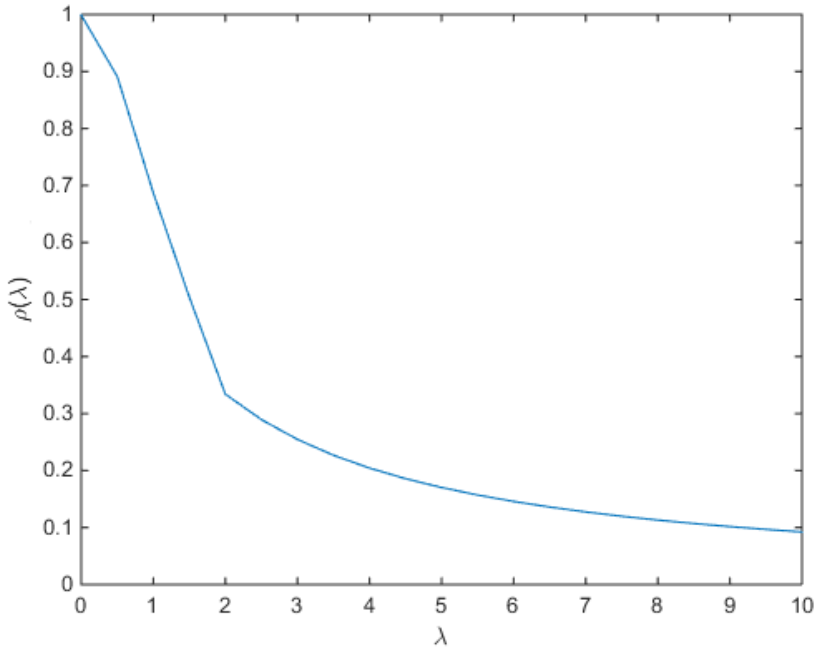

Figure 2.1: Spectral Radius Measurement from Fourier Analysis of Source Iteration

2.3 Synthetic Acceleration Basics

We know that it is expensive to obtain a transport solution in optically thick media using standard iteration techniques. In order to remedy that, we introduce a lower order (less expensive and fairly accurate) error approximation into our iteration scheme and synthetically accelerate the convergence of transport solution. This synthetic acceleration is equivalent to preconditioning. In a way, synthetic acceleration is like physics based preconditioning since we choose our lower order equation based on the form of error which, in turn, depends on the physics of the problem. In the this section, we describe basic synthetic acceleration approach, then we go on to show its equivalence with preconditioning.

Kopp came up with the idea of synthetic acceleration for source iteration in 1963 [14]. To accelerate the solution, the iterative scheme is broken into multiple stages. Standard methods consist of two stages. The first stage is a single iteration of source iteration (transport sweep). The second stage is an error-correction stage that uses an approximation of the transport equation for error estimation. The purpose of this second stage is to accelerate convergence of the iterative scheme.

In its operator form, source iteration is given by Eq. (2.38). In the context of synthetic acceleration for transport solve, after dropping notation for z and μ dependence for convenience, the first stage becomes [1]:

$$\psi^{m+\frac{1}{2}} = L^{-1}S\psi^{m} + L^{-1}q, \tag{2.59}$$

where, $\psi^{m+\frac{1}{2}}$ is the post $(m+1)^{th}$ sweep angular flux iterate. We use the index $m+\frac{1}{2}$ to emphasize the fact that the sweep is only the first stage of the solution algorithm and that the second stage

is still to be executed.

We want to obtain a significantly more accurate prediction of ψ than $\psi^{m+\frac{1}{2}}$. Theoretically, this can be accomplished by adding a second stage to the solution process - error-correction stage. To derive this, first, we subtract Eq. (2.59) from Eq. (2.34), where Eq. (2.34) represents the exact solution. We have:

$$L(\psi - \psi^{m+\frac{1}{2}}) = S(\psi - \psi^{m}). \tag{2.60}$$

Now, we add and subtract $\psi^{m+\frac{1}{2}}$ in the scattering term on the right hand side of the (2.60) and rearrange terms to obtain:

$$L(\psi - \psi^{m+\frac{1}{2}}) = S(\psi - \psi^{m+\frac{1}{2}}) + S(\psi^{m+\frac{1}{2}} - \psi^{m}). \tag{2.61}$$

Further, we can rearrange (2.61) to obtain the following equation for exact solution in terms of iteration residual, $\psi^{m+\frac{1}{2}} - \psi^{m}$:

$$\psi = \psi^{m+\frac{1}{2}} + (L - S)^{-1} S(\psi^{m+\frac{1}{2}} - \psi^{m}). \tag{2.62}$$

From Eq. (2.62), in order to obtain the solution, we would have to invert the $(L - S)$ operator exactly. This essentially means that we would have to solve the entire transport problem before actually solving it iteratively. Therefore, instead of doing that, we find an approximation to the $(L-S)$ operator of the transport equation that is relatively easy to invert. We call this operator F. Using this approximation with (2.62), we get the following synthetic acceleration equation (2.62):

$$\psi^{m+\frac{1}{2}} = L^{-1}S\psi^{m} + L^{-1}q, \tag{2.63}$$

$$\psi^{m+1} = \psi^{m+\frac{1}{2}} + F^{-1}S(\psi^{m+\frac{1}{2}} - \psi^{m}). \tag{2.64}$$

Note, here, that S is still the corresponds to the scattering operator of the transport equation. Depending on what we choose for our approximation operator, F, we get different synthetic acceleration schemes. For example, if we choose a P_5 representation of the $(L-S)$, we get a P_5 synthetic acceleration scheme.

Thus, in general, a synthetic acceleration scheme is as follows:

1. Initialize problem - define all the problem parameters.
2. Evaluate: $\psi^{m+\frac{1}{2}} = L^{-1}S\psi^{m} + L^{-1}q$.
3. Calculate: $S(\psi^{m+\frac{1}{2}} - \psi^{m})$.
4. Find: $F^{-1}S(\psi^{m+\frac{1}{2}} - \psi^{m})$.
5. Evaluate: $\psi^{m+1} = \psi^{m+\frac{1}{2}} + F^{-1}S(\psi^{m+\frac{1}{2}} - \psi^{m})$.
6. Check for convergence and loop back to step 2.

Now that we have described what we mean by synthetic acceleration, we demonstrate its equivalence with preconditioning in the next section.

2.3.1 Preconditioning and Synthetic Acceleration Equivalence

In order to demonstrate how easily the idea of synthetic acceleration can be applied to solution methods other than source iteration, we prove mathematical equivalence between synthetic acceleration, and preconditioning. The procedure closely follows that in [1]. Using Eq. (2.42), we have,

$$\psi^{m+\frac{1}{2}} = (I - A)\psi^m + \hat{q}, \tag{2.65}$$

where, A, and $\hat{q}$ are according to Eq. (2.41). Now, substitute the definition of $\psi^{m+\frac{1}{2}}$ from Eq. (2.65) into Eq. (2.64) to obtain:

$$\psi^{m+1} = (I - A)\psi^m + \hat{q} + F^{-1}S\left((I - A)\psi^m + \hat{q} - \psi^m\right). \tag{2.66}$$

We can further simplify (2.66) by noting that

$$\psi^{m+1} = \psi^m + (I + F^{-1}S)(-A\psi^m + \hat{q}). \tag{2.67}$$

If we define,

$$P = I + F^{-1}S, \tag{2.68}$$

we can write Eq. (2.67) as the preconditioned Richardson iteration form of the synthetic acceleration equation:

$$\psi^{m+1} = (I - PA)\psi^m + P\hat{q}. \tag{2.69}$$

Thus we now know that synthetic acceleration and preconditioning are equivalent while source iteration and Richardson iteration are equivalent. Therefore, when we do our analysis for source iteration, we are implicitly doing it for Richardson iteration also. Ideas from synthetic acceleration can seamlessly be integrated into preconditioning for linear solvers.

2.4 Summary

In this chapter, we derived the transport equation, described source iteration, demonstrated Fourier analysis for source iteration. We saw that the slowest converging mode for source iteration is the flat (zero-frequency) mode. For this particular mode, the eigenvalues of error are $\frac{\sigma_{s,l}}{\sigma_t}$. Thus when the scattering kernel is highly forward-peaked, attenuating only the first eigenvalue is not enough in order to achieve acceleration. We must attenuate a majority of eigenvalues (if not all) in order to achieve acceleration. This means we must correct for a majority of angular-flux moments in order to achieve acceleration. This calls for an angular-flux based acceleration scheme rather than a moment-based scheme. We also went over the basics of synthetic acceleration and demonstrated how a generic synthetic acceleration scheme would work. We also saw how synthetic acceleration for source iteration is equivalent to preconditioning for Richardson iteration.

In the next chapter we will systematically derive a lower-order equation for approximating the error. We will describe the FPSA algorithm and present P_N-based analysis for FPSA.

Chapter 3

Fokker-Planck Synthetic Acceleration

In the previous chapter we saw how to synthetically accelerate source iteration. In this chapter, we will look at how to systematically derive a lower order approximation to the error equation using asymptotics [3, 26, 30]. We will use this equation in the error-correction stage of our iterative method and then analyze it using Fourier analysis. Since the error equation has the same form as the transport equation, the scattering kernel of the error equation is the same as that of the transport equation. Moreover because the material parameters remain the same as the transport equation, convergence characteristics of the error equations will be identical to those of the transport equation. Here, we will derive the limit of error equation as the scattering kernel gets extremely forward-peaked. In other words, the average scattering angle for particles is arbitrarily close to unity.

3.1 Asymptotic Limit of the Error Equation

In this section, we will derive the limit of the error equation as the average scattering angle, $\mu_0 \to 1$. This limit is called the Fokker-Planck limit and the equation we get is called the Fokker-Planck equation.

First, we explicitly write down the exact error equation in its continuous form by using Eq. (2.33):

$$\mu\frac{\partial\epsilon(z,\mu)}{\partial z}+(\sigma_a(z)+\sigma_s(z))\epsilon(z,\mu)=2\pi\int_{-1}^{1}d\mu'\sigma_s(\mu_0)P_l(\mu')\epsilon(z,\mu'), \tag{3.1}$$

where,

$$\sigma_s(z)=\int_{-1}^{1}d\mu_0\sigma_s(z,\mu_0). \tag{3.2}$$

and,

$$\sigma_s(z,\mu_0)=2\pi\sum_{l=0}^{\infty}\frac{2l+1}{4\pi}P_l(\mu_0)\sigma_{s,l}(z)=\sum_{l=0}^{\infty}\frac{2l+1}{2}P_l(\mu_0)\sigma_{s,l}(z). \tag{3.3}$$

Note the absence of a source in the error equation as compared to the transport equation. This is because when we subtract the exact transport equation from the iteration equation, the source gets canceled out as we saw in Ch. 2. Moreover we will ignore iteration indices since they are not relevant to this derivation (they would only be relevant if the material properties changed over iterations but that is not the case here). Now, we introduce the following normalization for scattering cross-section moments:

$$\sigma_{s,l}(z)=\sigma_s(z)f_l(z), \tag{3.4}$$

where,

$$f_l(z)=\int_{-1}^{1}d\mu_0 f(z,\mu_0)P_l(\mu_0). \tag{3.5}$$

Upon introduction of Eq. (3.3), and (3.4) in Eq. (3.1) becomes:

$$\mu\frac{\partial\epsilon(z,\mu)}{\partial z}+\sigma_a(z)\epsilon(z,\mu)=\sigma_s(z)\sum_{l=0}^{\infty}\frac{2l+1}{2}P_l(\mu)f_l(z)\int_{-1}^{1}d\mu'P_l(\mu')\epsilon(z,\mu')-\sigma_s(z)\epsilon(z,\mu). \tag{3.6}$$

Now, we assume that $f(z, \mu_0)$ is significant only for $\mu_0 \to 1$. This means scattering cross-section and moments are insignificant away from μ_0. Therefore, we can Taylor-expand $P_l(\mu_0)$ about unity. We retain the first two terms to get [30]:

$$P_l(\mu_0) \approx 1 - \frac{dP_l(\mu_0)}{d\mu_0} \Big|_{\mu_0=1} (1 - \mu_0) \tag{3.7}$$

Now, recall Legendre equation:

$$(1 - \mu^2)\frac{\partial^2 P_l(\mu)}{\partial \mu^2} - 2\mu\frac{\partial P_l(\mu)}{\partial \mu} = -l(l+1)P_l(\mu). \tag{3.8}$$

Evaluating Eq. (3.8) at $\mu = 1$, and using the fact that $P_l(1) = 1, \forall l$, for $\mu_0 \to 1$, we get:

$$P_l(1) \approx 1 - \frac{l(l+1)}{2}(1 - \mu_0). \tag{3.9}$$

Inserting the relation from Eq. (3.9) in Eq. (3.5), and dropping the z's for convenience in our quantities, for $\mu_0 \to 1$, we have:

$$f_l = \int_{-1}^{1} d\mu_0 f(\mu_0) \left(1 - \frac{l(l+1)}{2}(1 - \mu_0)\right), \tag{3.10}$$

which becomes:

$$f_l = \int_{-1}^{1} d\mu_0 f(\mu_0) - \int_{-1}^{1} d\mu_0 \frac{l(l+1)}{2} f(\mu_0) + \int_{-1}^{1} d\mu_0 \frac{l(l+1)}{2} \mu_0 f(\mu_0). \tag{3.11}$$

We note that $\int_{-1}^{1} d\mu_0 f(\mu_0) = 1$ due to normalization. Using that and simplifying Eq. (3.11), for $\mu_0 \to 1$, we get:

$$f_l = 1 - \frac{l(l+1)}{2} (1 - \overline{\mu}_0), \tag{3.12}$$

where,

$$\overline{\mu}_0 = \int_{-1}^{1} d\mu_0 \mu_0 f(\mu_0). \tag{3.13}$$

Now, we insert relation from Eq. (3.12) into the right hand side of Eq. (3.6), we get right hand side:

$$RHS = \sigma_s(z) \sum_{l=0}^{\infty} \frac{2l+1}{2} P_l(\mu) \left(1 - \frac{l(l+1)}{2}(1-\overline{\mu}_0)\right) \int_{-1}^{1} d\mu' P_l(\mu')\epsilon(z,\mu') - \sigma_s(z)\epsilon(z,\mu). \tag{3.14}$$

Upon simplifying and rearranging terms in Eq. (3.14), we get:

$$\begin{aligned} RHS = \sigma_s(z) \sum_{l=0}^{\infty} \frac{2l+1}{2} P_l(\mu) \int_{-1}^{1} d\mu' P_l(\mu')\epsilon(z,\mu') - \sigma_s(z)\epsilon(z,\mu) \\ -\sigma_s(z)(1-\overline{\mu}_0) \sum_{l=0}^{\infty} \frac{2l+1}{2} \frac{l(l+1)}{2} P_l(\mu) \int_{-1}^{1} d\mu' P_l(\mu')\epsilon(z,\mu'). \end{aligned} \tag{3.15}$$

Now, using the Legendre equation for substituting the differential Laplacian for $l(l+1)P_l(\mu)$ in Eq. (3.15), and defining the momentum transfer crosssection as $\sigma_{tr} = \sigma_s(z)(1-\overline{\mu}_0)$, we get:

$$\begin{aligned} RHS = \sigma_s(z) \sum_{l=0}^{\infty} \frac{2l+1}{2} P_l(\mu) \int_{-1}^{1} d\mu' P_l(\mu')\epsilon(z,\mu') - \sigma_s(z)\epsilon(z,\mu) \\ +\frac{\sigma_{tr}(z)}{2} \sum_{l=0}^{\infty} \frac{2l+1}{2} \frac{\partial}{\partial\mu}(1-\mu^2) \frac{\partial}{\partial\mu} P_l(\mu) \int_{-1}^{1} d\mu' P_l(\mu')\epsilon(z,\mu'). \end{aligned} \tag{3.16}$$

Now, using the definition of error moments from Eq. (2.49), we have:

$$\begin{aligned} RHS = \sigma_s(z) \sum_{l=0}^{\infty} \frac{2l+1}{2} P_l(\mu)\epsilon_l(z) - \sigma_s(z)\epsilon(z,\mu) \\ +\frac{\sigma_{tr}(z)}{2} \sum_{l=0}^{\infty} \frac{2l+1}{2} \frac{\partial}{\partial\mu}(1-\mu^2) \frac{\partial}{\partial\mu} P_l(\mu)\epsilon_l(z). \end{aligned} \tag{3.17}$$

Simple rearrangement of Eq. (3.17) returns:

$$RHS = \sigma_s(z)\sum_{l=0}^{\infty}\frac{2l+1}{2}P_l(\mu)\epsilon_l(z) - \sigma_s(z)\epsilon(z,\mu) + \frac{\sigma_{tr}(z)}{2}\frac{\partial}{\partial\mu}(1-\mu^2)\frac{\partial}{\partial\mu}\sum_{l=0}^{\infty}\frac{2l+1}{2}P_l(\mu)\epsilon_l(z). \tag{3.18}$$

Finally, we note that:

$$\epsilon(z) = \sum_{l=0}^{\infty}\frac{2l+1}{2}P_l(\mu)\epsilon_l(z), \tag{3.19}$$

and substitute it in Eq. (3.18) and substitute RHS in Eq. (3.6) to get Fokker-Planck form of the error equation:

$$\mu\frac{\partial\epsilon(z,\mu)}{\partial z} + \sigma_a(z)\epsilon(z,\mu) = \frac{\sigma_{tr}(z)}{2}\frac{\partial}{\partial\mu}(1-\mu^2)\frac{\partial}{\partial\mu}\epsilon(z,\mu). \tag{3.20}$$

This is the Fokker-Planck approximation. Now, note in Eq. (3.19) that we use an infinite series expansion for defining angle-dependent error. If enough error moments are not taken into account, the scattering terms in Eq. (3.18) will cancel out and the Fokker-Planck approximation will have residual terms. In other words, we do not get Fokker-Planck approximation if enough moments are not taken into account for the continuous form of transport equation. In case we have discretized the angular domain using S_N method, we define the angular flux by the same number of moments in both the scattering terms which means they always cancel. So in discrete case, the Fokker-Planck approximation will always be valid as long as the scattering kernel has a Fokker-Planck limit. We will study the validity of the Fokker-Planck approximation for different scattering kernels next.

3.1.1 Validity of Fokker-Planck Approximation for Different Scattering Kernels

In order to see whether a given scattering kernel has a valid Fokker-Planck limit [30, 26, 4, 16], we closely follow class notes from [28]. We go back to Eq. (3.7) and keep higher order terms in Taylor expansion :

$$P_l(1) = \sum_{j=0}^{\infty} \frac{(-1)^j}{j!}(1-\mu_0)^j P_l^{(j)}(1), \tag{3.21}$$

where,

$$P_l^{(j)}(1) = \frac{d^j P_l(\mu_0)}{d\mu_0^j}\Big|_{\mu_0=1}. \tag{3.22}$$

Substituting Eq. (3.21) in Eq. (3.5), and doing necessary simplifications, we get:

$$f_l(z) = \sum_{j=0}^{\infty} \frac{(-1)^j}{j!} P_l^{(j)}(1) I_j, \tag{3.23}$$

where,

$$I_j = \int_{-1}^{1} d\mu_0 (1-\mu_0)^j f(z,\mu_0). \tag{3.24}$$

Now, we note that,

$$P_l^{(0)}(1) = 1, \tag{3.25}$$

$$P_l^{(j)}(1) = \frac{1}{2^j j!} \prod_{i=0}^{j-1} \left(l(l+1) - i(i+1)\right). \tag{3.26}$$

Then, inserting these definitions in Eq. (3.23), and inserting that in Eq. (3.6), we get:

$$\mu \frac{\partial \epsilon(z,\mu)}{\partial z} + \sigma_a(z)\epsilon(z,\mu) = \sigma_s(z) \sum_{l=0}^{\infty} \frac{2l+1}{2} P_l(\mu) \sum_{j=0}^{\infty} \frac{(-1)^j}{j!^2} P_l^{(j)}(1) I_j \epsilon_l(z) - \sigma_s(z)\epsilon(z,\mu). \tag{3.27}$$

Now, separating the $j=0$ term returns from the expansion above, we get:

$$\begin{aligned} \mu \frac{\partial \epsilon(z,\mu)}{\partial z} + \sigma_a(z)\epsilon(z,\mu) &= \sigma_s(z) \sum_{l=0}^{\infty} \frac{2l+1}{2} P_l(\mu)\epsilon_l(z) \\ +\sigma_s(z) \sum_{l=0}^{\infty} \frac{2l+1}{2} P_l(\mu) \sum_{j=1}^{\infty} \frac{(-1)^j}{2^j j!^2} P_l^{(j)}(1) I_j \epsilon_l(z) &- \sigma_s(z)\epsilon(z,\mu). \end{aligned} \tag{3.28}$$

Using the definition of error moments, the first and the last terms on the RHS cancel. After using Eq. (3.26) and slightly rearranging of the middle term, we have:

$$RHS = \sigma_s(z) \sum_{j=1}^{\infty} \frac{(-1)^j}{2^j j!^2} I_j \sum_{l=0}^{\infty} \frac{2l+1}{2} \prod_{i=0}^{j-1} (l(l+1) - i(i+1)) P_l(\mu) \epsilon_l(z). \tag{3.29}$$

Using the Legendre equation we described previously, we get:

$$RHS = \sigma_s(z) \sum_{j=1}^{\infty} \frac{1}{2^j j!^2} I_j \sum_{l=0}^{\infty} \frac{2l+1}{2} \prod_{i=0}^{j-1} (L_{FP} + i(i+1)) P_l(\mu) \epsilon_l(z), \tag{3.30}$$

with L_{FP} being defined according to Eq. (3.8). Rearranging the above equation and using the definition of error moments, we have:

$$RHS = \sigma_s(z) \sum_{j=1}^{\infty} \frac{1}{2^j j!^2} I_j \prod_{i=0}^{j-1} (L_{FP} + i(i+1)) \sum_{l=0}^{\infty} \frac{2l+1}{2} P_l(\mu) \epsilon_l(z), \tag{3.31}$$

and,

$$RHS = \sigma_s(z) \sum_{j=1}^{\infty} \frac{1}{2^j j!^2} I_j \prod_{i=0}^{j-1} (L_{FP} + i(i+1)) \epsilon(z, \mu), \tag{3.32}$$

If we let:

$$L_j = \sum_{j=1}^{\infty} \frac{1}{2^j j!^2} \prod_{i=0}^{j-1} (L_{FP} + i(i+1)), \tag{3.33}$$

we have:

$$RHS = \sigma_s(z) \sum_{j=1}^{\infty} I_j L_j \epsilon(z, \mu). \tag{3.34}$$

Separating $j = 1$ term from the above equation and using the definition of L_{FP} returns:

$$RHS = \frac{\sigma_{tr}}{2} \left(\frac{\partial}{\partial \mu} (1 - \mu^2) \frac{\partial \epsilon(z, \mu)}{\partial \mu} + 2 \sum_{j=2}^{\infty} \frac{I_n}{I_1} L_j \epsilon(z, \mu) \right). \tag{3.35}$$

This means we get the Fokker-Planck approximation like we got before but with extra terms given by:

$$L_{FP}^{Extra}\epsilon(z,\mu) = 2\sum_{j=2}^{\infty}\frac{I_n}{I_1}L_j\epsilon(z,\mu). \tag{3.36}$$

Therefore, for the FP representation to be valid, if $\frac{I_n}{I_1} \to 0$ as $\overline{\mu_0} \to 0$.

For forward-peaked scattering, scattering in backward direction is negligible. Therefore,

$$I_j = \int_{-1}^{1} d\mu_0(1-\mu_0)^j f(z,\mu_0) \quad \approx \quad f_0\int_{0}^{1} d\mu_0(1-\mu_0)^j P_l(\mu_0) \quad \leq \quad I_2. \tag{3.37}$$

Therefore, for a valid FP approximation, for the FP representation to be valid, if $\frac{I_2}{I_1} \to 0$ as $\overline{\mu_0} \to 1$.

Screened Rutherford Kernel

The screened Rutherford scattering kernel is widely used in modeling scattering behavior of electrons [7]. For this kernel,

$$f(\mu_0) = \frac{\eta(\eta+1)}{(1+2\eta-\mu_0)^2}. \tag{3.38}$$

According to [4],

$$\overline{\mu_0} = 1 - 2\eta ln(\frac{1}{\eta}), \tag{3.39}$$

and,

$$\lim_{\overline{\mu_0}\to 1}\frac{I_2}{I_1} = 1 - \frac{2}{ln(\frac{1}{\eta})} \to 0. \tag{3.40}$$

Note the logarithmic dependence on η in Eq. (3.40). This means the Fokker-Planck limit is only marginally valid for the screened Rutherford scattering kernel. In other words, it is only truly valid

when η is extremely small.

Exponential Kernel

Pomraning, Prinja and Vandenburg came up with this fictitious kernel, called the exponential kernel, in [8]. For this exponential kernel,

$$f(\mu_0) = \frac{e^{-\frac{1-\mu_0}{\gamma}}}{\gamma(1-e^{-\frac{2}{\gamma}})}, \tag{3.41}$$

where, $\gamma << 1$, $\overline{\mu_0} = 1 - \gamma$. Moreover according to [28, 8]:

$$\lim_{\overline{\mu_0}\to 1} \frac{I_2}{I_1} = 2(1-\overline{\mu_0}) = 0. \tag{3.42}$$

The exponential kernel has a valid Fokker-Planck limit because $\frac{I_2}{I_1}$ goes to zero as $\overline{\mu_0}$ goes to one in the Fokker-Planck limit.

Henyey Greenstein Kernel

The Henyey-Greenstein kernel is widely used in modeling transport of photons in clouds. For this kernel [26],

$$f(\mu_0) = \frac{1-g^2}{2(1-g\mu_0+g^2)^{\frac{3}{2}}}, \tag{3.43}$$

where, g is the asymmetry factor and $f(\mu_0)$ becomes a valid representation of the Dirac delta function as $g \to 1$ [26]. This kernel does not have a valid Fokker-Planck limit because [4]:

$$\lim_{\overline{\mu_0}\to 1} \frac{I_2}{I_1} = \frac{\overline{\mu_0}+1}{3} = \frac{2}{3}. \tag{3.44}$$

3.2 Fokker-Planck Synthetic Acceleration (FPSA)

We saw that for problems with forward-peaked scattering, Fokker-Planck can be a good approximation for the error. We will combine that with the idea of synthetic acceleration in this section. We will only be using Fokker-Planck as an accelerator so there will be no loss of accuracy even when the scattering kernel does not have a Fokker-Planck limit as long as the solution converges. The speedup rate will depend on the validity of Fokker-Planck limit to some extent. In this section, we will assume that F is the Fokker-Planck operator. The rest of the algorithm for FPSA is the same as presented in previous chapter. We present analysis for FPSA next.

3.2.1 P_L-based Fourier Analysis for FPSA

We begin by writing out the formulation for error equation. We know which physical quantities depend on which independent variables so we will skip writing them out for those specific physical quantities for convenience. We will assume constant material properties throughout this analysis. Subtract the exact solution, ψ, from both sides of Eq. (2.63) to obtain:

$$\psi^{m+1} - \psi = \psi^{m+\frac{1}{2}} - \psi + F^{-1}S(\psi^{m+\frac{1}{2}} - \psi^m). \tag{3.45}$$

The, we add and subtract the exact solution, ψ, in the scattering term on the right hand side to obtain:

$$\psi^{m+1} - \psi = \psi^{m+\frac{1}{2}} - \psi + F^{-1}S(\psi^{m+\frac{1}{2}} - \psi + \psi - \psi^m). \tag{3.46}$$

Further, we introduce error definitions. We have:

$$\psi - \psi^{m+\frac{1}{2}} = \epsilon^{m+\frac{1}{2}}, \quad \psi - \psi^{m+\frac{1}{2}} = \epsilon^{m+\frac{1}{2}}, \quad \text{and} \quad \psi - \psi^m = \epsilon^m. \tag{3.47}$$

Now, we substitute Eq. (3.47) into Eq. (3.46) to obtain:

$$-\epsilon^{m+1} = -\epsilon^{m+\frac{1}{2}} + F^{-1}S(\epsilon^m - \epsilon^{m+\frac{1}{2}}). \tag{3.48}$$

Multiplication of Eq. (3.48) with -1 yields the final form of the error equation:

$$\epsilon^{m+1} = \epsilon^{m+\frac{1}{2}} - F^{-1}S(\epsilon^m - \epsilon^{m+\frac{1}{2}}). \tag{3.49}$$

Since, here, our analysis is moment based, we introduce moments of error defined as follows:

$$\epsilon_l^m = \int_{-1}^{1} d\mu P_l(\mu)\epsilon^m = \sum_{n=1}^{N} w_n P_l(\mu_n)\epsilon^m. \tag{3.50}$$

Note that when we introduce the correction equation in terms of moments, our scattering operator from (2.36), upon using the orthogonality property of Legendre polynomials, becomes:

$$S = \sum_{l=0}^{L} \frac{(2l+1)}{2} P_l(\mu)\sigma_{s,l}. \tag{3.51}$$

Now, take the moment of operator $F^{-1}S$ from (3.49):

$$T = \int_{-1}^{1} d\mu P_l(\mu)F^{-1}S. \tag{3.52}$$

Using these new moment based definitions, we get the following equation in terms of error moments:

$$\epsilon_l^{m+1} = \epsilon_l^{m+\frac{1}{2}} - T(\epsilon_l^m - \epsilon_l^{m+\frac{1}{2}}). \tag{3.53}$$

Now that we have obtained the error equations, we analyze P_L acceleration. First, we sketch out general steps of analysis:

1. Obtain an expression for $\epsilon_l^{m+\frac{1}{2}}$ by doing Fourier analysis on source iteration.

2. Obtain an expression for $T(\epsilon_l^m - \epsilon_l^{m+\frac{1}{2}})$ by doing Fourier analysis on the error correction equation.

3. Obtain the matrix equation that will return spectral radius of the P_L accelerated solution scheme.

Step 1: Obtain an expression for $\epsilon_l^{m+\frac{1}{2}}$

This step is exactly the same as doing Fourier analysis for stand-alone source iteration. We did that in the previous chapter. From Eq. (2.52), (2.53), and (2.54), we have:

$$\hat{\epsilon}_l^{m+\frac{1}{2}} = \sum_{l=0}^{L} \frac{\sigma_{s,l}}{\sigma_t} \frac{2l+1}{2} \int_{-1}^{1} d\mu \frac{P_n(\mu)P_l(\mu)}{1+i\lambda\mu\sigma_t} \hat{\epsilon}_l^m. \tag{3.54}$$

We note that Eq. (3.54) represents the following matrix equation:

$$[\hat{\epsilon}_l^{m+\frac{1}{2}}] = A[\hat{\epsilon}_l^m], \tag{3.55}$$

where,

$$A = \sum_{l=0}^{L} \frac{\sigma_{s,l}}{\sigma_t} \frac{2l+1}{2} \int_{-1}^{1} d\mu \frac{P_n(\mu)P_l(\mu)}{1+i\lambda\mu\sigma_t}, \tag{3.56}$$

We multiply Eq. (3.55) by $e^{i\lambda\sigma_t z}$ and use Eq. (3.50) to get:

$$[\epsilon_l^{m+\frac{1}{2}}] = A[\epsilon_l^m], \tag{3.57}$$

Now that we have an equation for $\epsilon_l^{m+\frac{1}{2}}$, we move on to the next step.

Step 2: Obtain an expression for $T(\epsilon_l^m - \epsilon_l^{m+\frac{1}{2}})$

We use the Fokker-Planck approximation to estimate error. In other words, T, in (3.50), will be the inverse of the streaming-minus-scattering operator of the Fokker-Planck equation. We get the following error correction equation:

$$\mu\frac{\partial \upsilon^{m+1}}{\partial z}+\sigma_a\upsilon^{m+1}-\frac{\sigma_{tr}}{2}\frac{\partial}{\partial\mu}(1-\mu^2)\frac{\partial \upsilon^{m+1}}{\partial\mu}=\sum_{l=0}^{L}\frac{2l+1}{2}P_l(\mu)\sigma_{s,l}(\epsilon_l^m-\epsilon_l^{m+\frac{1}{2}}) \tag{3.58}$$

Now, we introduce Fourier mode assumption for error-estimate, υ^{m+1}:

$$\upsilon^{m+1}=\hat{\upsilon}_\lambda^{m+1}(\mu)e^{i\lambda z\sigma_t}. \tag{3.59}$$

Upon introducing Eq. (3.50), and Eq. (3.59) in Eq. (3.58), we obtain:

$$\begin{aligned}\mu\frac{\partial \hat{\upsilon}_\lambda^{m+1}(\mu)e^{i\lambda z\sigma_t}}{\partial z}+\sigma_a\hat{\upsilon}_\lambda^{m+1}(\mu)e^{i\lambda z\sigma_t}-\frac{\sigma_{tr}}{2}\frac{\partial}{\partial\mu}(1-\mu^2)\frac{\partial \hat{\upsilon}_\lambda^{m+1}(\mu)e^{i\lambda z\sigma_t}}{\partial\mu}\\ =\sum_{l=0}^{L}\frac{2l+1}{2}P_l(\mu)\sigma_{s,l}(e^{i\lambda\sigma_t z}\hat{\epsilon}_l^m-e^{i\lambda\sigma_t z}\hat{\epsilon}_l^{m+\frac{1}{2}}).\end{aligned} \tag{3.60}$$

Upon simplifying Eq. (3.60), taking its Legendre moment, and using the orthogonality property of Legendre polynomials, we get:

$$\begin{aligned}i\lambda\sigma_t\int_{-1}^{1}d\mu P_l(\mu)\mu\hat{\upsilon}_\lambda^{m+1}(\mu)+\sigma_a\int_{-1}^{1}d\mu P_l(\mu)\hat{\upsilon}_\lambda^{m+1}(\mu)\\ -\frac{\sigma_{tr}}{2}\int_{-1}^{1}d\mu\frac{\partial}{\partial\mu}(1-\mu^2)\frac{\partial\hat{\upsilon}_\lambda^{m+1}(\mu)}{\partial\mu}=\sigma_{s,l}(\hat{\epsilon}_l^m-\hat{\epsilon}_l^{m+\frac{1}{2}}).\end{aligned} \tag{3.61}$$

Now, using the recurrence relation for Legendre polynomials on the first term of Eq. (3.61), expanding $\hat{\upsilon}_\lambda^{m+1}(\mu)$ in the third term of Eq. (3.61) using Legendre expansion, and dropping notation for z dependence for moments for convenince, we get:

$$\frac{l}{2l+1}i\lambda\sigma_t\hat{v}_{l-1}^{m+1}+\frac{l+1}{2l+1}i\lambda\sigma_t\hat{v}_{l+1}^{m+1}+\sigma_a\hat{v}_l^{m+1}-\frac{\sigma_{tr}}{2}\int_{-1}^{1}d\mu\frac{\partial}{\partial\mu}(1-\mu^2)\frac{\partial}{\partial\mu}\sum_{n=0}^{\infty}\frac{2l+1}{2}P_n(\mu)\hat{v}_n^{m+1}$$
$$=\sigma_{s,l}(\hat{\epsilon}_l^m-\hat{\epsilon}_l^{m+\frac{1}{2}}). \tag{3.62}$$

Simple rearrangement of the third term in Eq. (3.62), followed by use of Legendre's equation, Eq. (3.8), and orthogonality property of Legendre polynomials returns:

$$\frac{l}{2l+1}i\lambda\sigma_t\hat{v}_{l-1}^{m+1}+\frac{l+1}{2l+1}i\lambda\sigma_t\hat{v}_{l+1}^{m+1}+\sigma_a\hat{v}_l^{m+1}+\frac{\sigma_{tr}}{2}l(l+1)\hat{v}_n^{m+1}=\sigma_{s,l}(\hat{\epsilon}_l^m-\hat{\epsilon}_l^{m+\frac{1}{2}}), \tag{3.63}$$

where,

$$\hat{v}_l^m=\int_{-1}^{1}d\mu P_l(\mu)\hat{v}_\lambda^m(\mu). \tag{3.64}$$

Eq. (3.63) can be written in matrix form as:

$$[\hat{v}_l^{m+1}]=B^{-1}XE[\hat{\epsilon}_l^m] \tag{3.65}$$

where,

$$X = diag(\sigma_{s,l}), \tag{3.66}$$
$$E = I-A, \tag{3.67}$$
$$B_{l,l} = \sigma_a+\frac{\sigma_{tr}}{2}l(l+1), \tag{3.68}$$
$$B_{l,l+1} = \frac{l+1}{2l+1}i\lambda\sigma_t, \tag{3.69}$$
$$B_{l-1,l} = \frac{l}{2l+1}i\lambda\sigma_t. \tag{3.70}$$

Here, for example, with $L=3$,

$$X = \begin{bmatrix} \sigma_{s,0} & 0 & 0 & 0 \\ 0 & \sigma_{s,1} & 0 & 0 \\ 0 & 0 & \sigma_{s,2} & 0 \\ 0 & 0 & 0 & \sigma_{s,3} \end{bmatrix}, \tag{3.71}$$

and,

$$B = \begin{bmatrix} \sigma_a & i\lambda\sigma_t & 0 & 0 \\ \frac{1}{3}i\lambda\sigma_t & \sigma_a + \sigma_{tr} & \frac{2}{3}i\lambda\sigma_t & 0 \\ 0 & \frac{2}{5}i\lambda\sigma_t & \sigma_a + 3\sigma_{tr} & \frac{3}{5}i\lambda\sigma_t \\ 0 & 0 & \frac{3}{7}i\lambda\sigma_t & \sigma_a + 6\sigma_{tr} \end{bmatrix}. \tag{3.72}$$

Here, $l = 0, 1, 2, 3$ in rows $1, 2, 3, 4$ respectively in X, and B. These matrices can be generalized for arbitrary L.

Now that we have an expression for $\hat{v}_l^{m+1}$, we effectively have an expression for $T(\epsilon^m - \epsilon^{m+\frac{1}{2}})$ because:

$$\hat{v}_l^{m+1} e^{i\lambda\sigma_t z} = T(\epsilon^m - \epsilon^{m+\frac{1}{2}}). \tag{3.73}$$

Now, we move on to the next step.

Step 3: Obtain the overall iteration matrix to calculate spectral radius

If we insert Fourier mode assumption from Eq. (3.59), and the definition of $T(\epsilon^m - \epsilon^{m+\frac{1}{2}})$ from Eq. (3.73) into Eq. (3.53), we get,

$$\hat{\epsilon}_l^{m+1} e^{i\lambda\sigma_t z} = \hat{\epsilon}_l^{m+\frac{1}{2}} e^{i\lambda\sigma_t z} - \hat{v}_l^m e^{i\lambda\sigma_t z}. \tag{3.74}$$

Using the relations obtained in previous two steps, Eq. (3.57) and Eq. (3.65), and substituting relevant terms into Eq. (3.74), we get,

$$[\epsilon_l^{m+1}] = (A - B^{-1}XE)[\epsilon_l^m]. \tag{3.75}$$

Thus our iteration matrix becomes $(A - B^{-1}XE)$. We note that the spectral radius of this iteration matrix will be the spectral radius of a FP preconditioned Richardson iteration.

3.2.2 P_L Acceleration

We will first derive the P_L equations. In order to do that, we recall the transport equation, Eq. (2.31). We take the l^{th} Legendre moment of the transport:

$$\int_{-1}^{1} P_l(\mu)d\mu \left[\mu\frac{\partial\psi}{\partial z} + \sigma_t\psi = \sum_{n=0}^{\infty}(2n+1)P_n(\mu)\sigma_{s,l}\phi_l + q\right]. \tag{3.76}$$

Upon rearrangement of (3.76), we get:

$$\frac{\partial}{\partial z}\int_{-1}^{1}\mu P_l(\mu)\psi + \sigma_t\int_{-1}^{1}P_l(\mu)\psi = \sum_{l=0}^{\infty}(2l+1)\sigma_{s,l}\phi_l\int_{-1}^{1}P_n(\mu)P_l(\mu)d\mu + \int_{-1}^{1}P_l(\mu)qd\mu. \tag{3.77}$$

Using the recurrence relation, orthogonality property of Legendre polynomials [19], and moment definitions from (2.32) we get the following form of P_l equations:

$$\frac{l}{2l+1}\frac{d\phi_{l-1}}{dz} + \frac{l+1}{2l+1}\frac{d\phi_{l+1}}{dz} + (\sigma_t - \sigma_{s,l})\phi_l = q_l, \tag{3.78}$$

where, $l = 0, 1, ..., L$, and,

$$q_l = \int_{-1}^{1} P_l(\mu)qd\mu. \tag{3.79}$$

A set of L coupled equations must be solved to obtain the P_L solution of the problem. One closure to P_L approximation is obtained by setting the derivative of $(L+1)^{th}$ Legendre moment to zero. Thus the last equation of the P_L equation series takes the following form:

$$\frac{l}{2l+1}\frac{d\phi_{l-1}}{dz} + (\sigma_t - \sigma_{s,l})\phi_l = q_l, \tag{3.80}$$

Now that we have derived the P_L equations, we move on to see how they can be used in the error-correction stage of the two stage iteration algorithm. In the next subsection, we will derive iteration matrix for P_L acceleration using Fourier analysis.

Fourier Analysis for P_L Acceleration

For analysis of P_L acceleration, we will use the same error notations and Fourier mode assumptions as those used in the case of analysis of FPSA. The only thing different from FPSA will be the equation used to calculate the error estimate. First, we recall general steps of analysis:

1. Obtain an expression for $\epsilon_l^{m+\frac{1}{2}}$ by doing Fourier analysis on source iteration.
2. Obtain an expression for $T(\epsilon_l^m - \epsilon_l^{m+\frac{1}{2}})$ by doing Fourier analysis on the error correction equation.
3. Obtain the matrix equation that will return spectral radius of the P_L accelerated solution scheme.

Step 1: Obtain an expression for $\epsilon^{m+\frac{1}{2}}$

Since we are accelerating the same transport equation, the first step here is identical to that of FPSA. We obtain the same matrix equation for $\epsilon^{m+\frac{1}{2}}$ as we did at the end of first step of FPSA analysis, Eq. (3.57). We move on to the next step.

Step 2: Obtain an expression for $T(\epsilon_l^m - \epsilon_l^{m+\frac{1}{2}})$

We use the P_L approximation to estimate error. Thus, in other words, T, in (3.50), will be the inverse of the streaming-minus-scattering operator of the P_L equations. We get the following from of the error correction equation in terms of moments:

$$\frac{l}{2l+1}\frac{d\upsilon_{l-1}^{m+1}}{dz} + \frac{l+1}{2l+1}\frac{d\upsilon_{l+1}^{m+1}}{dz} + (\sigma_t - \sigma_{s,l})\upsilon_l^{m+1} = \sigma_{s,l}\left(\epsilon_l^m - \epsilon_l^m\right), \tag{3.81}$$

where, $l = 0, 1, ..., L$.

We introduce Fourier mode assumption for υ_l^m. We will also ignore the notation for z and μ to get:

$$\upsilon_l^m = \hat{\upsilon}_l e^{i\lambda\sigma_t z}. \tag{3.82}$$

Upon substituting the Fourier mode assumption for υ_l, and ϵ_l into (3.81), and simplifying it by carrying out relevant derivatives and canceling exponential term from both sides, we get:

$$\frac{l}{2l+1}i\lambda\sigma_t\hat{\upsilon}_{l-1}^{m+1} + \frac{l+1}{2l+1}i\lambda\sigma_t\hat{\upsilon}_{l+1}^{m+1} + (\sigma_t - \sigma_{s,l})\hat{\upsilon}_l^{m+1} = \sigma_{s,l}\left(\hat{\epsilon}_l^m - \hat{\epsilon}_l^m\right). \tag{3.83}$$

with P_L closure:

$$\frac{l}{2l+1}i\lambda\sigma_t\hat{\upsilon}_{l-1}^{m+1} + (\sigma_t - \sigma_{s,l})\hat{\upsilon}_l^{m+1} = \sigma_{s,l}\left(\hat{\epsilon}_l^m - \hat{\epsilon}_l^m\right). \tag{3.84}$$

We get the following matrix equation using (3.83), and (3.84):

$$[\upsilon_l^{m+1}] = B^{-1}XE[\epsilon_l^m], \tag{3.85}$$

where,

$$X = diag(\sigma_{s,l}), \tag{3.86}$$

$$E = I - A, \tag{3.87}$$

$$B_{l,l} = \sigma_a + \sigma_{s,l}, \tag{3.88}$$

$$B_{l,l+1} = \frac{l+1}{2l+1} i\omega\sigma_t, \tag{3.89}$$

$$B_{l-1,l} = \frac{l}{2l+1} i\omega\sigma_t. \tag{3.90}$$

For example, with $L = 3$, we have:

$$X = \begin{bmatrix} \sigma_{s,0} & 0 & 0 & 0 \\ 0 & \sigma_{s,1} & 0 & 0 \\ 0 & 0 & \sigma_{s,2} & 0 \\ 0 & 0 & 0 & \sigma_{s,3} \end{bmatrix}, \tag{3.91}$$

and,

$$B = \begin{bmatrix} \sigma_t - \sigma_{s,0} & i\lambda\sigma_t & 0 & 0 \\ \frac{1}{3} i\lambda\sigma_t & \sigma_t - \sigma_{s,1} & \frac{2}{3} i\lambda\sigma_t & 0 \\ 0 & \frac{2}{5} i\lambda\sigma_t & \sigma_t - \sigma_{s,2} & \frac{3}{5} i\lambda\sigma_t \\ 0 & 0 & \frac{3}{7} i\lambda\sigma_t & \sigma_t - \sigma_{s,3} \end{bmatrix}. \tag{3.92}$$

Here, $l = 0, 1, 2, 3$ in rows $1, 2, 3, 4$ respectively in X, and B. These matrices can be generalized for arbitrary L and therefore, we have a general expression for $T(\epsilon_l^m - \epsilon_l^{m+\frac{1}{2}})$, where,

$$T(\epsilon_l^m - \epsilon_l^{m+\frac{1}{2}}) = \upsilon_l^{m+1} e^{i\lambda\sigma_t z}. \tag{3.93}$$

Now, we move on to the next step.

Step 3: Obtain the overall iteration matrix to calculate spectral radius

This step is, again, identical to that for FPSA. We have the same form of iteration matrix as for FPSA. Thus our iteration matrix becomes $(A - B^{-1}XE)$, and its spectral radius returns the spectral radius of P_L accelerated solution scheme.

3.2.3 FPSA as a Special Case of P_L Acceleration

Notice from the Fourier analysis of FPSA and P_L acceleration that the only difference between the two schemes is in the diagonal term of the matrix, B, where:

$$B_{l,l}^{FPSA} = \sigma_a + \frac{\sigma_{tr}}{2} l(l+1) = \sigma_a + \frac{\sigma_{s,0} - \sigma_{s,1}}{2} l(l+1) \tag{3.94}$$

$$B_{l,l}^{P_L} = \sigma_t - \sigma_{s,l} = \sigma_a + \sigma_{s,0} - \sigma_{s,l}. \tag{3.95}$$

Using the above equations from Fourier analyses of FPSA and P_L acceleration, we note that FPSA is a special case of P_L acceleration when:

$$\sigma_{s,l} = \sigma_{s,0} - \frac{\sigma_{s,0} - \sigma_{s,1}}{2} l(l+1). \tag{3.96}$$

Another way of obtaining this equivalence relation is by recognizing that Legendre polynomials are eigenfunctions of both Boltzmann scattering operator and the Fokker-Planck operator [15, 21]:

$$\Gamma_B P_l(\mu) = (\sigma_{s,l} - \sigma_{s,0}) P_l(\mu), \tag{3.97}$$

$$\Gamma_{FP} P_l(\mu) = -\frac{(\sigma_{s,0} - \sigma_{s,1})}{2} l(l+1) P_l(\mu), \tag{3.98}$$

and equating the eigenvalues of Fokker-Planck and the Boltzmann scattering operators:

$$\sigma_{s,l} - \sigma_{s,0} = -\frac{(\sigma_{s,0} - \sigma_{s,1})}{2} l(l+1). \tag{3.99}$$

Simple rearrangement of Eq. (3.99) returns Eq. (3.96). Morel came up with a way of using modified scattering cross-section moments with the transport operator to obtain the Fokker-Planck solution by exploiting the above relation in [21].

3.3 Summary

In this chapter, we derived the limiting equation for the error equation as mean scattering angle tends to unity. We also described the conditions under which the Fokker-Planck approximation is a valid limit of the error equation in order to see where to expect FPSA to work well. We noted that in case of continuous transport equation, we only obtain the Fokker-Planck limit (irrespective of the scattering kernel) when sufficient number of Legendre moments are used to represent angular flux. This 'sufficient number' of moments is subjective and completely depends on the scattering kernel used in the calculations. We also noted that the Fokker-Planck approximation is a valid asymptotic limit for the exponential scattering kernel. For the screened Rutherford kernel, it is only valid when the screening parameter, η is sufficiently small. The Henyey-Greenstein kernel does not have the Fokker-Planck approximation as a valid asymptotic limit. Moreover, we introduced FPSA and provided analysis for this method. We compared it to P_L acceleration and derived the conditions under which FPSA is equivalent to P_L acceleration.

Chapter 4

FPSA Fourier Analysis for Accelerating S_N Equations

We have seen in previous chapters that because our scattering kernel is forward-peaked, the flat mode of error also has forward-peaked scattering. Asymptotic analysis returns Fokker-Planck approximation for error. Therefore, we use Fokker-Planck approximation for acceleration. We note that because we estimate error itself (and not just a predetermined number of error moments) with FPSA, all relevant error moments are accelerated.

The numerical implementation of FPSA can be tricky to analyze because depending on the discretization of the Fokker-Planck operator (angular derivative term of Fokker-Planck equation) all error moments may or may not be preserved [22, 34]. For this reason, and for the reason that P_N based analysis of FPSA requires using extremely high precision calculations, we will present an angularly discrete framework for analyzing FPSA.

In the next section, we will present spatial and angular discretization for the transport and Fokker-

Planck equations. We present two ways to discretize the Fokker-Planck operator - weighted finite difference (WFD), and moment preserving discretization (MPD). The WFD discretization only preserves the first two moments while MPD can preserve upto $N-1$ moments of the discrete Fokker-Planck S_N equations, where N is the S_N order.

4.1 S_N Equations with Linear Discontinuous (LD) Spatial Discretization

The discrete ordinates (S_N) method is one of the most widely used methods to solve the transport equation. The S_N method requires the transport equation to hold exactly for N distinct angles [19]. Further, the scattering integral term is evaluated using a compatible quadrature rule. Angles are chosen so that the angular flux moment integrals are evaluated accurately. Thus if we choose a quadrature formula on interval $-1 \leq \mu \leq 1$, with N ordinates, μ_n, and corresponding weights, w_n, we get a discrete ordinates approximation of order N [19]. In slab geometry the Gauss-Legendre quadrature (GLQ) [9] is often used because GLQ evaluates polynomials of order 2N-1 exactly . We will use the same.

4.1.1 S_N Equations

In slab geometry, the discrete ordinates approximation is follows:

$$\mu_n \frac{\partial \psi(z,\mu_n)}{\partial z} + \sigma_t(z)\psi(z,\mu_n) = \sum_{l=0}^{L} \frac{2l+1}{2} P_l(\mu_n)\sigma_{s,l}(z)\phi_l(z) + Q(z,\mu_n), \tag{4.1}$$

with,

$$\phi_l(z) = \sum_{n=1}^{N} w_n P_l(\mu_n)\psi(z,\mu_n). \tag{4.2}$$

These equations then form a system of S_N equations:

$$\mu_n \frac{\partial \Psi(z)}{\partial z} + \sigma_t(z)\Psi(z) = \sum_{l=0}^{L} \frac{2l+1}{2} P_l(\mu_n)\sigma_{s,l}(z)\Phi_l(z) + Q_N(z), \tag{4.3}$$

where,

$$\Psi(z) = [\psi(z,\mu_n)]^T, \quad n = 1,2,3...N, \tag{4.4}$$

is the angular flux vector,

$$\Phi_l(z) = [\phi_l(z)]^T, \quad l = 1,2,3...L, \tag{4.5}$$

is the moments vector and,

$$Q_N(z) = [Q(z,\mu_n)]^T, \quad n = 1,2,3...N. \tag{4.6}$$

is the angular source vector.

4.1.2 Linear Discontinuous Finite Element Discretization of S_N Equations

We discretize the S_N equations in space using linear-discontinuous finite element method. We represent flux using linear discontinuous elements on the following mesh [11, 33]. An illustration of the linear discontinuous angular flux for $\mu > 0$ and $\mu < 0$ is shown in Fig. 4.1 and 4.2 respectively, for a one-dimensional, slab-geometry mesh. The angular fluxes on the left and right of a mesh cell are denoted by L and R, respectively, and the open and closed circles indicate which angular fluxes

are used to introduce discontinuities between mesh cells. That is, for $\mu > 0$ the incoming flux for mesh cell $i+1$ is taken to be $\psi_{i,R}$, and for $\mu < 0$, the incoming flux for cell i is taken to be $\psi_{i+1,L}$.

Figure 4.1: LD mesh for a slab $\mu > 0$ [11]

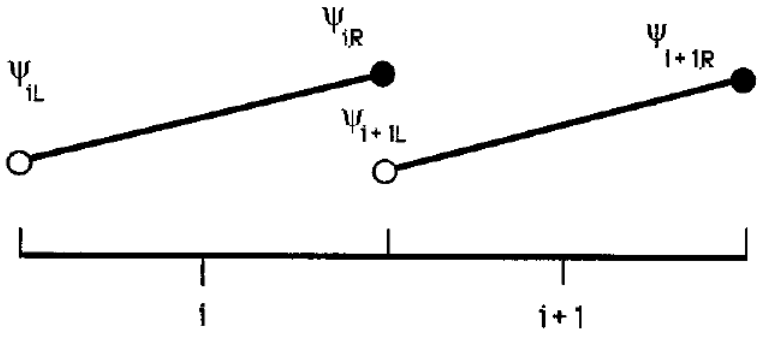

Figure 4.2: LD mesh for a slab $\mu < 0$ [11]

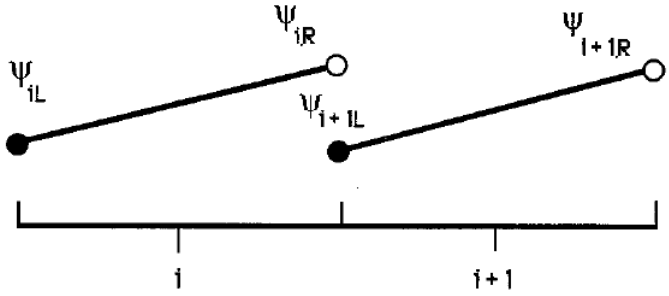

In order to derive the linear discontinuous discretization for S_N equations, we begin by introducing linear basis and weight functions [33]. We introduce the following approximation for angular flux for i^{th} element along z for the angular flux vector, $\tilde{\Psi}_i(z)$, as the following linear combination:

$$\tilde{\Psi}_i(z) = \Psi_{i,L} B_{i,L}(z) + \Psi_{i,R} B_{i,R}(z), \tag{4.7}$$

where, edge fluxes:

$$\Psi_i(z_{i,L}) = \Psi_{i,L}, \tag{4.8}$$

$$\Psi_i(z_{i,R}) = \Psi_{i,R}, \tag{4.9}$$

and, $B_{i,L}(z)$, and $B_{i,R}(z)$ are linear basis functions in z defined as:

$$B_{i,L}(z) = \frac{z_{i,R} - z}{z_{i,R} - z_{i,L}}, \tag{4.10}$$

$$B_{i,R}(z) = \frac{z - z_{i,L}}{z_{i,R} - z_{i,L}}. \tag{4.11}$$

Therefore, note that:

$$B_{i,L}(z_{i,L}) = 1, \tag{4.12}$$

$$B_{i,R}(z_{i,L}) = 0, \tag{4.13}$$

$$B_{i,L}(z_{i,R}) = 0, \tag{4.14}$$

$$B_{i,R}(z_{i,R}) = 1. \tag{4.15}$$

Now, the weighted residual form for element i will have two equations:

$$\int_{z_{i,L}}^{z_{i,R}} dz B_{i,L}(z) \left(\mu_n \frac{\partial \tilde{\Psi}_i}{\partial z} + \sigma_t(z_i)\tilde{\Psi}_i = \sum_{l=0}^{L} \frac{2l+1}{2} P_l(\mu_n)\sigma_{s,l}(z_i)\Phi_{l,i} + Q_N(z_i) \right) = 0, \tag{4.16}$$

$$\int_{z_{i,L}}^{z_{i,R}} dz B_{i,R}(z) \left(\mu_n \frac{\partial \tilde{\Psi}_i}{\partial z} + \sigma_t(z_i)\tilde{\Psi}_i = \sum_{l=0}^{L} \frac{2l+1}{2} P_l(\mu_n)\sigma_{s,l}(z_i)\Phi_{l,i} + Q_N(z_i) \right) = 0. \tag{4.17}$$

Now, we insert the definition of $\tilde{\psi}_{i,n}$ from Eq. (4.7) into Eq. (4.16), and carry out the necessary simplifications using Eq. (4.10) and Eq. (4.12), and use upwinding illustrated previously in Fig. 4.1 and 4.2, where, for $-1 \leq \mu_n \leq 0$, we have,

$$\Psi_i(z_{i,R}) = \Psi_{i+1,L}. \tag{4.18}$$

and, for $0 \leq \mu_n \leq 1$, we have,

$$\Psi_i(z_{i,L}) = \Psi_{i-1,R} \tag{4.19}$$

Now order quadrature such that $0 \leq \mu_n < 1$ for $n = 1, ...\frac{N}{2}$, and $-1 < \mu_n \leq 0$ for $n = \frac{N}{2} + 1, ...N$. For $n = 1, ...\frac{N}{2}$, we have the following matrix equations:

$$\begin{aligned}\begin{bmatrix} \frac{\mu_n}{2} + \frac{\sigma_t(z_i)\Delta z_i}{3} & \frac{\mu_n}{2} + \frac{\sigma_t(z_i)\Delta z_i}{6} \\ \frac{-\mu_n}{2} + \frac{\sigma_t(z_i)\Delta z_i}{6} & \frac{\mu_n}{2} + \frac{\sigma_t(z_i)\Delta z_i}{3} \end{bmatrix} \begin{bmatrix} \Psi_{i,L} \\ \Psi_{i,R} \end{bmatrix} &= \begin{bmatrix} \mu_n \Psi_{i-1,R,n} \\ 0 \end{bmatrix} + \begin{bmatrix} q_{i,L} \\ q_{i,R} \end{bmatrix} \\ &+ \sum_{l=0}^{L} \frac{2l+1}{2} P_l(\mu_n)\sigma_{s,l}(z_i) \begin{bmatrix} \frac{\Delta z_i}{3} & \frac{\Delta z_i}{6} \\ \frac{\Delta z_i}{6} & \frac{\Delta z_i}{3} \end{bmatrix} \begin{bmatrix} \Phi_{l,i,L} \\ \Phi_{l,i,R}, \end{bmatrix}\end{aligned} \tag{4.20}$$

where,

$$\begin{bmatrix} q_{i,L} \\ q_{i,R} \end{bmatrix} = \begin{bmatrix} \int_{z_{i,L}}^{z_{i,R}} B_{i,L}(z) Q_N(z_i) \\ \int_{z_{i,L}}^{z_{i,R}} B_{i,R}(z) Q_N(z_i). \end{bmatrix} \tag{4.21}$$

Similarly, for $n = \frac{N}{2} + 1, ...N$, we get the following:

$$\begin{aligned}\begin{bmatrix} \frac{-\mu_n}{2} + \frac{\sigma_t(z_i)\Delta z_i}{3} & \frac{\mu_n}{2} + \frac{\sigma_t(z_i)\Delta z_i}{6} \\ \frac{-\mu_n}{2} + \frac{\sigma_t(z_i)\Delta z_i}{6} & \frac{-\mu_n}{2} + \frac{\sigma_t(z_i)\Delta z_i}{3} \end{bmatrix} \begin{bmatrix} \Psi_{i,L} \\ \Psi_{i,R} \end{bmatrix} &= \begin{bmatrix} 0 \\ -\mu_n \Psi_{i+1,L} \end{bmatrix} + \begin{bmatrix} q_{i,L} \\ q_{i,R} \end{bmatrix} \\ &+ \sum_{l=0}^{L} \frac{2l+1}{2} P_l(\mu_n)\sigma_{s,l}(z_i) \begin{bmatrix} \frac{\Delta z_i}{3} & \frac{\Delta z_i}{6} \\ \frac{\Delta z_i}{6} & \frac{\Delta z_i}{3} \end{bmatrix} \begin{bmatrix} \Phi_{l,i,L} \\ \Phi_{l,i,R}, \end{bmatrix}\end{aligned} \tag{4.22}$$

The equations (4.20) and (4.22) are solved the following way. For every angle $\mu_n > 0$, we march the left boundary to solve Eq. (4.20) for $\Psi_{i,L}$ and $\Psi_{i,R}$ in every mesh cell, updating the incoming value of $\Psi_{i-1,R}$ in Eq. (4.20) for the next cell to the right. Then, for all $\mu_n < 0$, we start on the right boundary and march from right-to-left to solve Eq. (4.22) for $\Psi_{i,L}$ and $\Psi_{i,R}$ in each mesh cell, updating $\psi_{i+1,L}$ for the next cell to the left. This is referred to as an S_N sweep [19], and has been represented in our previous discussions by the operator L^{-1}. Alternatively, we can assemble the matrix equations above for every angle and every mesh cell into a single linear system that can be inverted either directly or iteratively. In practice, this is not usually the case, and the S_N equations are solved iteratively, without forming the full linear system directly. Krylov methods (GMRES) are generally used to solve this linear system [12]. We will talk more about this in the next chapter.

4.2 Angular Discretization of Fokker-Planck Operator

We saw how to do LD-S_N discretization for the transport equation. The spatial discretization of the FP equation is analogous to that of the transport. The only difference between the transport and FP equations lies in how the scattering operator is represented. In this section, we will only describe angular discretization of the Fokker-Planck operator. We begin with the WFD discretization.

4.2.1 Weighted Finite Difference

A weighted finite difference [22] approximation is used to represent the Fokker-Planck operator:

$$L_{FP} = \frac{\sigma_{tr}}{2}\frac{\partial}{\partial\mu}(1-\mu^2)\frac{\partial\psi(z,\mu)}{\partial\mu}|_{\mu=n} \approx \frac{\sigma_{tr}}{2}\frac{\alpha_{n+\frac{1}{2}}\dot{\psi}_{n+\frac{1}{2}} - \alpha_{n-\frac{1}{2}}\dot{\psi}_{n+\frac{1}{2}}}{w_n}, \tag{4.23}$$

where, w_n is the quadrature weight for n^{th} angular cosine,

$$\dot{\psi}_{n+\frac{1}{2}} = \frac{\psi_{n+1} - \psi_n}{\mu_{n+1} - \mu_n}, \tag{4.24}$$

$$\dot{\psi}_{n-\frac{1}{2}} = \frac{\psi_n - \psi_{n-1}}{\mu_n - \mu_{n-1}}, \tag{4.25}$$

and,

$$\alpha_{n+\frac{1}{2}} = \alpha_{n+\frac{1}{2}} + C\mu_n w_n, \quad \alpha_{\frac{1}{2}} = 0, \tag{4.26}$$

with, $C = \sum_{n=1}^{N} w_n$, is the normalization constant. Thus, we can write the angular Laplacian term as:

$$L_{FP} = \frac{\sigma_{tr}}{2}\frac{\partial}{\partial\mu}(1-\mu^2)\frac{\partial\psi(z,\mu_n)}{\partial\mu} \approx a_n\psi_{n+1} - b_n\psi_n + c_n\psi_{n-1}, \tag{4.27}$$

where,

$$a_n = \frac{\sigma_{tr}}{2w_n}\frac{\alpha_{n+\frac{1}{2}}}{\mu_{n+1} - \mu_n}, \tag{4.28}$$

$$b_n = -\frac{\sigma_{tr}}{2w_n}\left(\frac{\alpha_{n+\frac{1}{2}}}{\mu_{n+1} - \mu_n} + \frac{\alpha_{n-\frac{1}{2}}}{\mu_n - \mu_{n-1}}\right), \tag{4.29}$$

and,

$$c_n = \frac{\sigma_{tr}}{2w_n}\frac{\alpha_{n-\frac{1}{2}}}{\mu_n - \mu_{n-1}}, \tag{4.30}$$

We can write the S_N form of the Fokker-Planck equation in operator notation as:

$$H\frac{\partial\Psi}{\partial z} + \sigma_a\Psi - W\Psi = Q_N, \tag{4.31}$$

where, H is $diag(\mu_n)$, Ψ is the vector of angular fluxes (which is evaluated at each spatial location along the mesh), σ_a is $diag(\sigma_a)$, Q_N is the source vector along each angle, and operator W is given by:

$$W_{n,n} = -\frac{\sigma_{tr}}{2w_n}\left(\frac{\alpha_{n+\frac{1}{2}}}{\mu_{n+1}-\mu_n}+\frac{\alpha_{n-\frac{1}{2}}}{\mu_n-\mu_{n-1}}\right), \tag{4.32}$$

$$W_{n,n+1} = \frac{\sigma_{tr}}{2w_n}\frac{\alpha_{n+\frac{1}{2}}}{\mu_{n+1}-\mu_n}, \tag{4.33}$$

$$W_{n,n-1} = \frac{\sigma_{tr}}{2w_n}\frac{\alpha_{n-\frac{1}{2}}}{\mu_n-\mu_{n-1}}. \tag{4.34}$$

This particular angular discretization only preserves the zeroth and the first moment of the angular flux [22]. This means that P_N based Fourier analysis of FPSA will not necessarily match numerically measured results. Now that we know how to discretize the angular Laplacian using WFD, we present a method that allows us to preserve upto N moments of Fokker-Planck angular flux next.

4.2.2 Moment Preserving Discretization

MPD of the angular derivative term of the Fokker-Planck equation is based on [34]. In that paper, Warsa and Prinja present a method which allows N angular flux moments of the Fokker-Planck equation to be preserved. Note that it only preserves the angular flux moments of the Fokker-Planck equation and must not be confused with the preservation of angular flux moments of the transport equation. To describe their method in more detail, we recall the Fokker-Planck equation and the Fokker-Planck angular differential operator. Then, we recognize that in one dimension, the Legendre polynomials are eigenfunctions of the Fokker-Planck operator:

$$L_{FP}P_l(\mu) = -l(l+1)P_l(\mu). \tag{4.35}$$

Then we integrate by parts to show that for any function $f(\mu)$,

$$\int_{-1}^{1} L_{FP} P_l(\mu) f(\mu) d\mu = \int_{-1}^{1} P_l(\mu) L_{FP} f(\mu) d\mu. \tag{4.36}$$

Now, upon substituting (4.35) in (4.36), we obtain the following relation:

$$\int_{-1}^{1} P_l(\mu) L_{FP} f(\mu) d\mu = -l(l+1) \int_{-1}^{1} P_l(\mu) f(\mu) d\mu. \tag{4.37}$$

Then, upon evaluating integrals using S_N quadrature, we obtain the following:

$$\sum_{m=1}^{N} w_m P_l(\mu_m) L_{FP}^{MPD} \psi = -l(l+1) \sum_{m=1}^{N} w_m P_l(\mu_m) \psi_m. \tag{4.38}$$

Here, $l = 0, ...N-1$. (4.38) defines an equation system of $N \times N$ matrix for the angular flux vector, Ψ of length N for each spatial node. Thus we have,

$$L_{FP}^{MPD} \Psi = R\Psi, \tag{4.39}$$

where, L_{FP}^{MPD} is the discrete form of L_{FP} and, $R = O^{-1}G$. The elements of O and G are given as follows:

$$O_{i,j} = P_{i-1}(\mu_j) w_j, \quad \text{and} \quad G_{i,j} = -i(i-1) P_{i-1}(\mu_j) w_j. \tag{4.40}$$

Here, $i, j = 1, 2...N$. Using the relations derived above, we can write down the Fokker-Planck equation with MPD in the following form:

$$H \frac{\partial}{\partial z} \Psi + \sigma_a \Psi - \frac{\sigma_{tr}(x)}{2} R\Psi = Q_N. \tag{4.41}$$

Solving this form of the Fokker-Planck equation guarantees that at least N angular moments of the angular flux will be preserved. This allows us obtain a more accurate solution to the Fokker-Planck equation. While this allows us to obtain a more accurate Fokker-Planck solution, it is unclear as to

how this would affect the convergence of the transport solution when this is used for acceleration. We will do Fourier analysis in the next section.

4.3 Angularly Discrete Fourier Analysis for FPSA

In this section, we present angularly discrete Fourier analysis for FPSA. Each discretization of the Fokker-Planck operator will have different iteration matrices. First, we look why we do angularly discrete Fourier analysis.

4.3.1 Subtle Nuances About Angularly Discrete Transport and FP Equations

Firstly, as noted at the beginning of this chapter and in this section, different discretizations of the Fokker-Planck operator preserve different number of moments. While WFD only preserves zeroth and first Legendre moments of the angular flux, MPD preserves upto N Legendre moments. The angluarly continuous Fourier analysis (P_L-based analysis) presented in the previous chapter is moment based and therefore, requires the numerical implementation to preserve all L moments in order to get consistent spectral radius measurement.

Moreover, in the previous chapter, we noted that in case of continuous transport equation, we only obtain the Fokker-Planck limit (irrespective of the scattering kernel) when 'sufficient number' of Legendre moments are used to represent angular flux. This, however, is not true in discrete (S_N) case. When we discretize the transport equation and represent it as S_N equations (as discussed earlier in this chapter), we are essentially predetermining the number of moments we will use to represent angular flux. This means we represent the angular flux using N moments that are consistently being calculated using S_N equations. This means there are no residual terms even when expansion order of the scattering kernel is low. There is always a valid Fokker-Planck limit for

S_N equations as long as the scattering kernel allows it. This creates a discrepancy between the angularly continuous and angularly discrete Fourier analyses. This will play an important role in explaining why P_N-based and S_N-based Fourier analyses differ at low scattering expansion orders. The above mentioned reasoning also explains why it would be incorrect to use P_N-based Fourier analysis to analyze the FPSA algorithm for S_N equations.

Other than that, by $S_N - P_L$ equivalence [19], we know that when $N = L+1$, S_N and P_L equations are equivalent. Taking this and Eq. (3.96) into account, we note that FPSA will converge in one iteration when it is analytically equivalent to P_L acceleration. In other words, when the cross-section moments in the Boltzmann scattering operator are according to Eq. (3.96), we get convergence in one iteration. Moreover, it would be a valid to think that the convergence will be rapid in case the cross-section moments of the relevant transport problem are close to those obtained from Eq. (3.96). However, in the case when we truncate scattering expansion arbitrarily and N is no longer equal to $L + 1$, the FPSA-P_L acceleration equivalence will no longer hold because of inconsistent introduction of zero values for moments with $N \geq l > L$ due to truncation of the scattering expansion. For example, consider a problem with $L = 1$, and $N = 4$. For $B_{l,l}^{FPSA}$, we have:

$$B_{1,1}^{P_L} = \sigma_t - \sigma_{s,0}, \tag{4.42}$$

$$B_{2,2}^{P_L} = \sigma_t - \sigma_{s,1}, \tag{4.43}$$

$$B_{3,3}^{P_L} = \sigma_t, \tag{4.44}$$

$$B_{4,4}^{P_L} = \sigma_t. \tag{4.45}$$

For $B_{l,l}^{FPSA}$, we have:

$$B_{1,1}^{FPSA} = \sigma_t - \sigma_{s,0}, \tag{4.46}$$

$$B_{2,2}^{FPSA} = \sigma_t - \sigma_{s,1}, \tag{4.47}$$

$$B_{3,3}^{FPSA} = \sigma_t + 2\sigma_{s,0} - 3\sigma_{s,1}, \tag{4.48}$$

$$B_{4,4}^{FPSA} = \sigma_t + 5\sigma_{s,0} - 6\sigma_{s,1}. \tag{4.49}$$

Clearly, upon comparison of $B_{l,l}^{P_L}$, and $B_{l,l}^{FPSA}$, we find that FPSA-P_L acceleration equivalence can no longer hold due to the difference values of $B_{l,l}^{P_L}$, and $B_{l,l}^{FPSA}$, for $N \geq l > L$, here, $l = 2$, and 3.

Next we look at Fourier analysis for FPSA with WFD for Fokker-Planck.

4.3.2 Analysis with WFD

The FPSA scheme, in its present form, is completely angularly discrete. Therefore we calculate our solutions at discrete angular points. Moreover, we use these discrete points along with a weighted finite difference discretization in order to resolve the angular derivative in the Fokker-Planck error correction equation. This discrete finite difference based discretization preserves only first two moments and not higher moments. Thus any continuous-in-angle approach to Fourier analysis for this scheme is not expected to consistently represent error correction equation. In other words, continuous-in-angle representation of the differential term in the Fokker-Planck equation and finite difference based discrete-in-angle result in different moment values and therefore may represent the error differently. Therefore we do not expect continuous-in-angle Fourier analysis and discrete-in-angle numerical implementation to always be consistent. For this section, we will do discrete-in-angle Fourier analysis. The following steps outline how it is done:

1. Obtain an expression for angle dependent error after one transport sweep.

2. Obtain an expression for $MS(\epsilon^m - \epsilon^{m+\frac{1}{2}})$.

3. Obtain the overall matrix equation that represents the error growth of FPSA scheme and calculate the spectral radius.

Step 1: Obtain and expression for $\epsilon^{m+\frac{1}{2}}$

Since we have already seen some analysis in the previous chapters, we will skip the introduction of Fourier mode assumption and simplification steps. We will also ignore notification of μ and z dependence of relevant quantities for simplification. These quantities have been described at length in Ch. 3. Now, we introduce the Fourier mode assumption into the error (transport) equation. Then upon taking the n^{th} Legendre moment of the equation, we get:

$$\int_{-1}^{1} d\mu P_n(\mu) \left[(i\lambda\sigma_t\mu + \sigma_t)\hat{\epsilon}^{m+\frac{1}{2}} = \sum_{l=0}^{L} \frac{2l+1}{2} P_l(\mu)\sigma_{s,l}\hat{\epsilon}_l^m \right]. \tag{4.50}$$

Using orthogonality property on the right hand side of (4.50) returns:

$$\int_{-1}^{1} d\mu P_l(\mu) \left[(i\lambda\sigma_t\mu + \sigma_t)\hat{\epsilon}^{m+\frac{1}{2}} \right] = \sigma_{s,l}\hat{\epsilon}_l^m. \tag{4.51}$$

Recall the Fourier anzats for ϵ_l^m and introduce it in (4.51), we get:

$$\int_{-1}^{1} d\mu P_n(\mu) \left[(i\lambda\sigma_t\mu + \sigma_t)\hat{\epsilon}_l^{m+\frac{1}{2}} \right] = \sigma_{s,l} \int_{-1}^{1} P_l(\mu)\hat{\epsilon}_l^m. \tag{4.52}$$

Each integral is now written in discrete weighted-sum form using Gauss quadrature. We have:

$$\sum_{n=1}^{N} P_l(\mu_n) w_n \left[(i\lambda\sigma_t\mu_n + \sigma_t)\hat{\epsilon}_l^{m+\frac{1}{2}} \right] = \sigma_{s,l} \sum_{n=1}^{N} P_l(\mu_n) w_n \hat{\epsilon}_l^m. \tag{4.53}$$

We get the following matrix equation from (4.53):

$$[\hat{\epsilon}^{m+\frac{1}{2}}] = A[\hat{\epsilon}^m]. \tag{4.54}$$

where,

$$A = Y^{-1}Z, \tag{4.55}$$

and,

$$Y_{ln} = P_l(\mu_n)w_n(i\lambda\sigma_t\mu_n + \sigma_t) \quad \text{and} \quad Z_{ln} = \sigma_{s,l}P_l(\mu_n)w_n. \tag{4.56}$$

Here, A is the iteration matrix in discrete-in-angle from. This again returns $\frac{\sigma_{s,0}}{\sigma_t}$ as the spectral radius. Now that we have an expression for $\hat{\epsilon}^{m+\frac{1}{2}}$, we move on to the next step.

Step 2: Obtain an expression for $MS(\epsilon^m - \epsilon^{m+\frac{1}{2}})$

First, we rewrite the Fokker-Planck error-correction equation:

$$\mu\frac{\partial \upsilon^{m+1}}{\partial z} + \sigma_a\upsilon^{m+1} - \frac{\sigma_{tr}}{2}\frac{\partial}{\partial\mu}(1-\mu^2)\frac{\partial \upsilon^{m+1}}{\partial\mu} = \sum_{l=0}^{L}\frac{2l+1}{2}P_l(\mu)\sigma_{s,l}(\hat{\epsilon}_l^m - \hat{\epsilon}_l^{m+\frac{1}{2}}). \tag{4.57}$$

Upon introduction of Fourier mode assumption for υ, definition of error moment, carrying out the relevant spatial differentiation and simplifications, we obtain the following equation:

$$\int_{-1}^{1} d\mu P_l(\mu)\left[i\lambda\sigma_t\mu + \sigma_a - \frac{\sigma_{tr}}{2}\frac{\partial}{\partial\mu}(1-\mu^2)\frac{\partial}{\partial\mu}\right]\hat{\upsilon}^{m+1} = \sigma_{s,l}\int_{-1}^{1} P_l(\mu)(\hat{\epsilon}_l^m - \hat{\epsilon}_l^{m+\frac{1}{2}}). \tag{4.58}$$

Now we introduce angularly discrete formulation where each integral is written in the form of a weighted sum and the angular differential is written as a weighted finite difference [22] to obtain:

$$\begin{aligned} i\lambda\sigma_t\sum_{n=1}^{N}P_l(\mu_n)w_n\hat{\upsilon}_n^{m+1} + \sigma_a\sum_{n=1}^{N}P_l(\mu_n)w_n\hat{\upsilon}_n^{m+1} \\ - \sum_{n=1}^{N}P_l(\mu_n)w_n\left(a_n\hat{\upsilon}_{n+1}^{m+1} - b_n\hat{\upsilon}_n^{m+1} + c_n\hat{\upsilon}_{n-1}^{m+1}\right) = \sigma_{s,l}\sum_{n=1}^{N}P_l(\mu_n)w_n(\hat{\epsilon}^m - \hat{\epsilon}^{m+\frac{1}{2}}), \end{aligned} \tag{4.59}$$

where, a_n, b_n, and c_n are according to Eq. (4.28), (4.29), and (4.30).

From (4.59), we get the following matrix equation:

$$[\hat{\upsilon}^{m+1}] = B^{-1}CD[\hat{\epsilon}^{m}], \tag{4.60}$$

where,

$$D = I - A, \quad C_{l,n} = \sigma_{s,l} P_l(\mu_n) w_n, \quad \text{and} \quad B = B1 + B2 + B3, \tag{4.61}$$

with,

$$B1_{l,n} = P_l(\mu_n) w_n \left(i\lambda\sigma_t \mu_n + \sigma_a + b_n \right), \tag{4.62}$$

$$B2_{l,n+1} = P_l(\mu_n) w_n a_n, \tag{4.63}$$

and,

$$B2_{l,n-1} = P_l(\mu_n) w_n c_n. \tag{4.64}$$

Now that we have an expression for $\hat{\upsilon}^{m+1}$, we can obtain the expression for $MS(\epsilon^m - \epsilon^{m+\frac{1}{2}})$, since by definition,

$$\upsilon^{m+1} = \hat{\upsilon}^{m+1} e^{i\lambda\sigma_t z} = MS(\epsilon^m - \epsilon^{m+\frac{1}{2}}). \tag{4.65}$$

Now, we move on to the next step.

Step 3: Obtain the overall iteration matrix

Just like in the case of P_L based analysis for FPSA, we get the following equation:

$$\hat{\epsilon}^{m+1} = \hat{\epsilon}^{m+\frac{1}{2}} - \hat{\upsilon}^{m+1}. \tag{4.66}$$

This returns the following equation:

$$[\hat{\epsilon}^{m+1}] = (A - B^{-1}CD)[\hat{\epsilon}^{m}]. \tag{4.67}$$

Thus our iteration matrix is $A - B^{-1}CD$ whose spectral radius returns the spectral radius of the accelerated scheme. Now that we have seen angularly discrete analysis for FPSA with WFD, we will present angularly discrete analysis for FPSA with MPD.

4.3.3 Analysis with MPD

Angularly discrete Fourier analysis for MPD is done in the same way as we did for WFD. The only difference will be how the Fokker-Planck operator is represented in the error-correction equation. Formally, we follow the exact same three steps as for WFD:

1. Obtain an expression for angle dependent error after one transport sweep.
2. Obtain an expression for $MS(\epsilon^m - \epsilon^{m+\frac{1}{2}})$.
3. Obtain the overall matrix equation that represents the error growth of FPSA scheme and calculate the spectral radius.

Step 1: Obtain and expression for $\epsilon^{m+\frac{1}{2}}$

The expression for $\epsilon^{m+\frac{1}{2}}$ will be exactly the same as that for WFD. Therefore, we represent it using Eq. (4.54), (4.55), and (4.56). We move on to the next step.

Step 2: Obtain an expression for $MS(\epsilon^m - \epsilon^{m+\frac{1}{2}})$

We begin with Eq. (4.58):

$$\int_{-1}^{1} d\mu P_l(\mu) \left[i\lambda\sigma_t\mu + \sigma_a - \frac{\sigma_{tr}}{2}\frac{\partial}{\partial\mu}(1-\mu^2)\frac{\partial}{\partial\mu} \right] \hat{v}^{m+1} = \sigma_{s,l} \int_{-1}^{1} P_l(\mu)(\hat{\epsilon}^m - \hat{\epsilon}^{m+\frac{1}{2}}). \tag{4.68}$$

Now we introduce angularly discrete formulation where each integral is written in the form of a weighted sum just like we did for WFD. However, here, the angular differential term is replaced by $-l(l+1)$ using the Legendre equation [34] to obtain:

$$i\lambda\sigma_t \sum_{n=1}^{N} P_l(\mu_n) w_n \hat{v}_n^{m+1} + \sigma_a \sum_{n=1}^{N} P_l(\mu_n) w_n \hat{v}_n^{m+1} + \frac{\sigma_{tr}}{2} l(l+1) \sum_{n=1}^{N} P_l(\mu_n) w_n \hat{v}_n^{m+1}$$
$$= \sigma_{s,l} \sum_{n=1}^{N} P_l(\mu_n) w_n (\hat{\epsilon}^m - \hat{\epsilon}^{m+\frac{1}{2}}). \quad (4.69)$$

From (4.59), we get the following matrix equation:

$$[\hat{v}^{m+1}] = B^{-1} C D [\hat{\epsilon}^m], \quad (4.70)$$

where,

$$D = I - A, \quad (4.71)$$

$$C_{l,n} = \sigma_{s,l} P_l(\mu_n) w_n, \quad (4.72)$$

and,

$$B_{l,n} = i\lambda\sigma_t w_n P_l(\mu_n)\mu_n + \sigma_a w_n P_l(\mu_n) + l(l+1)\frac{\sigma_{tr}}{2} w_n P_l(\mu_n). \quad (4.73)$$

Now that we have an expression for $\hat{v}^{m+1}$, we can obtain the expression for $MS(\epsilon^m - \epsilon^{m+\frac{1}{2}})$, since by definition,

$$v^{m+1} = \hat{v}^{m+1} e^{i\lambda\sigma_t z} = MS(\epsilon^m - \epsilon^{m+\frac{1}{2}}). \quad (4.74)$$

Now, we move on to the next step.

Step 3: Obtain the overall iteration matrix

Just like in the case of P_L based analysis for FPSA, we get the following equation:

$$\hat{\epsilon}^{m+1} = \hat{\epsilon}^{m+\frac{1}{2}} - \hat{v}^{m+1}. \tag{4.75}$$

This returns the following equation:

$$[\hat{\epsilon}^{m+1}] = (A - B^{-1}CD)[\hat{\epsilon}^{m}]. \tag{4.76}$$

Thus our iteration matrix is $A - B^{-1}CD$ whose spectral radius returns the spectral radius of FPSA with MPD.

4.4 Spectral Radius Estimates

First, we will measure expected convergence rates using Fourier analysis presented in previous section. We will do our study using three different scattering kernels - exponential kernel, screened Rutherford kernel, and Henyey-Greenstein kernel. For each kernel, we will first keep L constant and vary N. Then after, we will fix N and vary L. Finally, we will vary both N and L simultaneously while making sure that $N = L + 1$. Other than that, we will vary the screening parameter [7], η, for screened Rutherford kernel, asymmetry factor [26], g, for the Henyey-Greenstein kernel, and parameter, Δ [8] for the exponential kernel. We begin with screened Rutherford kernel.

4.4.1 Screened Rutherford Kernel (SRK)

For SRK, we choose $C = 0.7805$ and $\eta = 2.836 \times 10^{-4}$, 2.836×10^{-5}, and 2.836×10^{-6}. We begin by choosing $\eta = 2.836 \times 10^{-4}$. The scattering cross-section moments for these parameters are given in Table 4.1. Note that we only present data for the first 16 moments. Higher moments can be generated easily using any symbolic math application. We present it in Appendix A.

Parameter	Value
S_N order	16, 32, 64
σ_a	1
σ_t	1376.667689 cm^{-1}
$\sigma_{s,0}$	1375.667689 cm^{-1}
$\sigma_{s,1}$	1370.072664 cm^{-1}
$\sigma_{s,2}$	1361.213931 cm^{-1}
$\sigma_{s,3}$	1349.856033 cm^{-1}
$\sigma_{s,4}$	1336.498659 cm^{-1}
$\sigma_{s,5}$	1321.507580 cm^{-1}
$\sigma_{s,6}$	1305.167316 cm^{-1}
$\sigma_{s,7}$	1287.707638 cm^{-1}
$\sigma_{s,8}$	1269.318837 cm^{-1}
$\sigma_{s,9}$	1250.161346 cm^{-1}
$\sigma_{s,10}$	1230.372215 cm^{-1}
$\sigma_{s,11}$	1210.069693 cm^{-1}
$\sigma_{s,12}$	1189.356585 cm^{-1}
$\sigma_{s,13}$	1168.322808 cm^{-1}
$\sigma_{s,14}$	1147.047368 cm^{-1}
$\sigma_{s,15}$	1125.599937 cm^{-1}

Table 4.1: Problem Parameters - SRK - $\eta = 2.836 \times 10^{-4}$

Keep $L(= 15)$ Constant, and Vary N (= 16, 32, 64)

First, we will keep L constant and vary N. The plots obtained from Fourier analyses are presented in Fig. 4.4, 4.4, 4.5, and 4.6. Numerical data obtained from Fourier analyses is also summarized in Table 4.2.

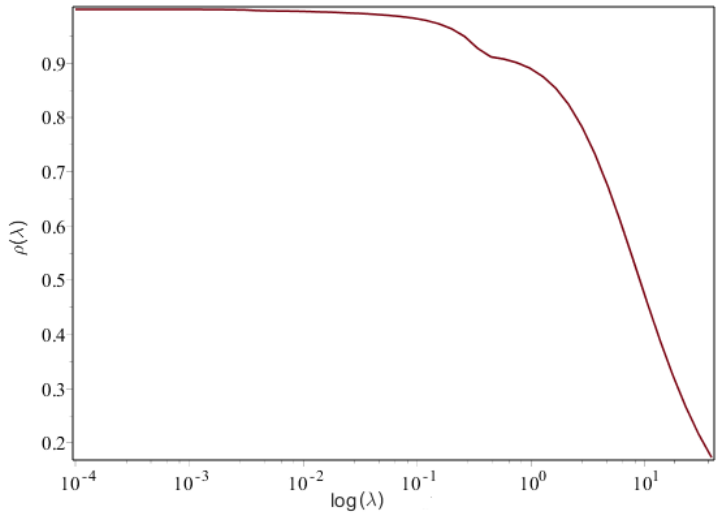

Figure 4.3: SRK - $\eta = 2.836 \times 10^{-4}$ - Unaccelerated - $L = 15$

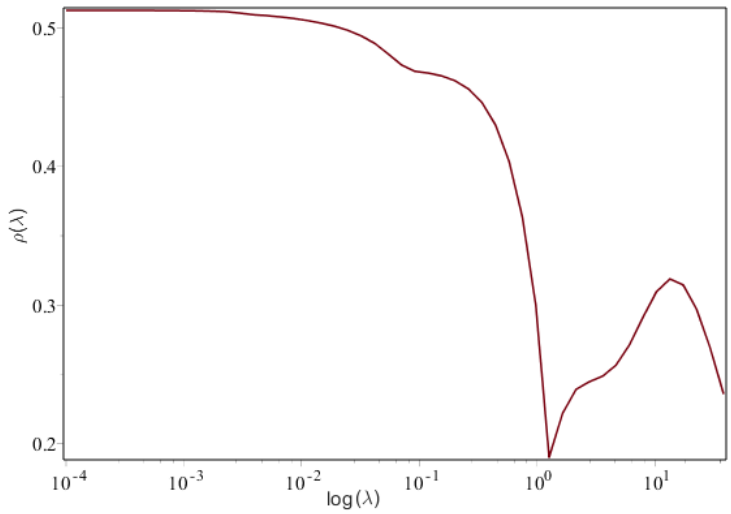

Figure 4.4: SRK - $\eta = 2.836 \times 10^{-4}$ - FPSA - $L = 15$

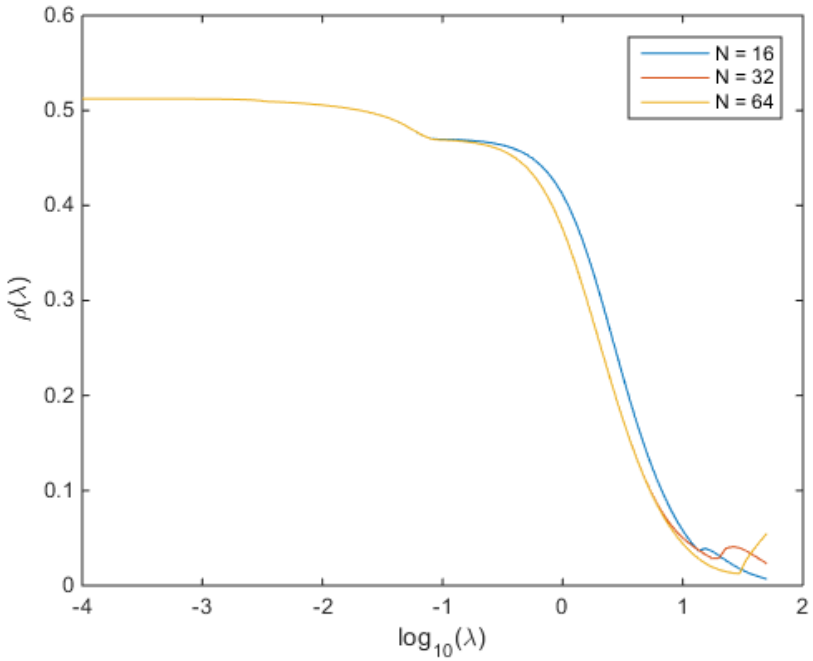

Figure 4.5: SRK - $\eta = 2.836 \times 10^{-4}$ - FPSA - MPD - $L = 15$

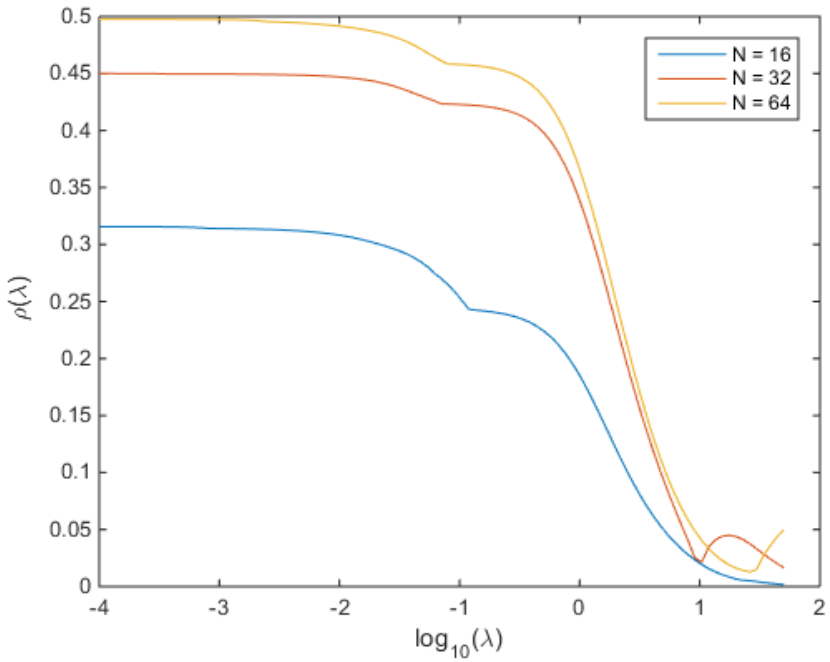

Figure 4.6: SRK - $\eta = 2.836 \times 10^{-4}$ - FPSA - WFD - $L = 15$

N	**Unaccelerated ρ**	**FPSA P_N-based ρ**	**FPSA-MPD ρ**	**FPSA-WFD ρ**
∞	0.9992	0.5123		
16			0.5123	0.3156
32			0.5123	0.4500
64			0.5123	0.4975

Table 4.2: Spectral Radius - SRK $\eta = 2.836 \times 10^{-4}$ - $L = 15$

We see how since MPD preserves N moments, spectral radii are identical with analytical spectral radius calculations. Spectral radii from WFD not preserve all relevant moments, therefore, we see only marginal agreement with increasing N. We also note for WFD that increasing N results in increased spectral radius. This is because increasing N represents improving representation of the analytical transport and FP equations.

N (= 64) constant and vary L (= 1, 7, 15, 31, 63)

Now we will keep N constant and vary L. The plots obtained from Fourier analyses are presented in Fig. 4.7, and 4.8. Moreover, the information obtained from Fourier analyses is summarized in Table 4.3.

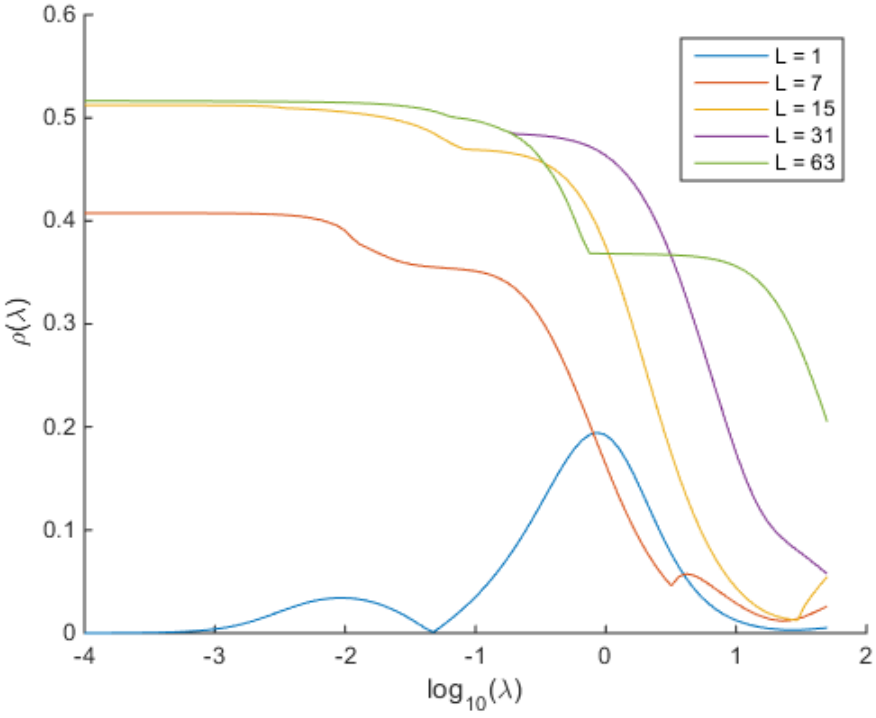

Figure 4.7: SRK - $\eta = 2.836 \times 10^{-4}$ - FPSA - MPD - $N = 64$

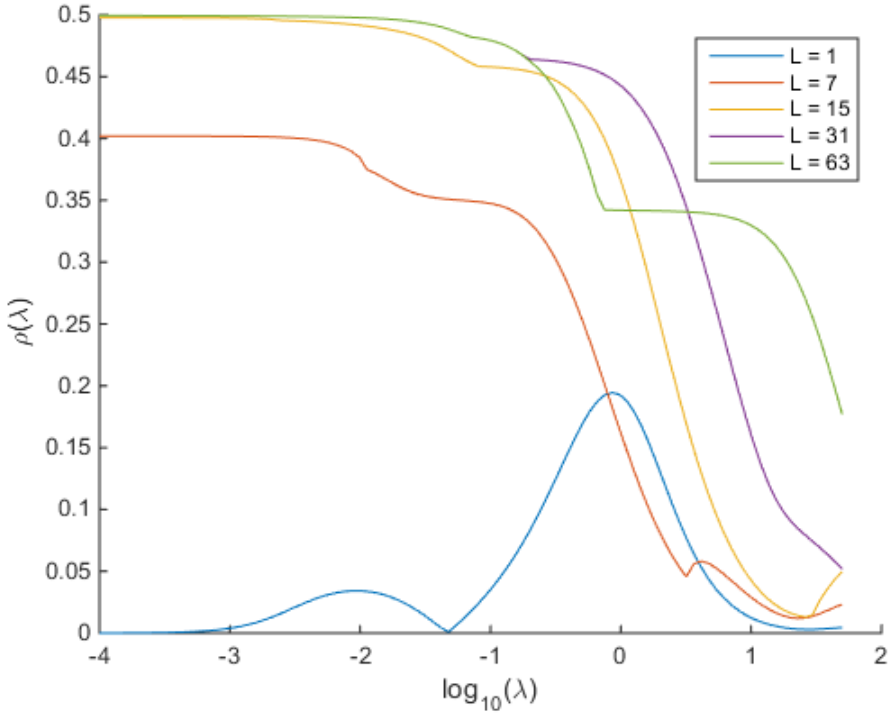

Figure 4.8: SRK - $\eta = 2.836 \times 10^{-4}$ - FPSA - WFD - $N = 64$

L	**FPSA-MPD ρ**	**FPSA-WFD ρ**
1	0.1945	0.1945
7	0.4075	0.4019
15	0.5123	0.4975
31	0.5163	0.4995
63	0.5163	0.4995

Table 4.3: Spectral Radius - SRK $\eta = 2.836 \times 10^{-4}$ - $N = 64$

We note convergence in spectral radius with increasing L. This is because increasing L represents convergence in scattering behavior of the transport equation.

Vary N, and L s.t. $L = N$-1

Now, we vary N and L together such that $N = 2, 16, 32, 64, 128$ and $L = 1, 16, 31, 63, 127$. Eigenvalue plots obtained by Fourier analyses have been presented in Fig. 4.9, 4.10, 4.11 and 4.12. The

spectral radius information is summarized in Table 4.4.

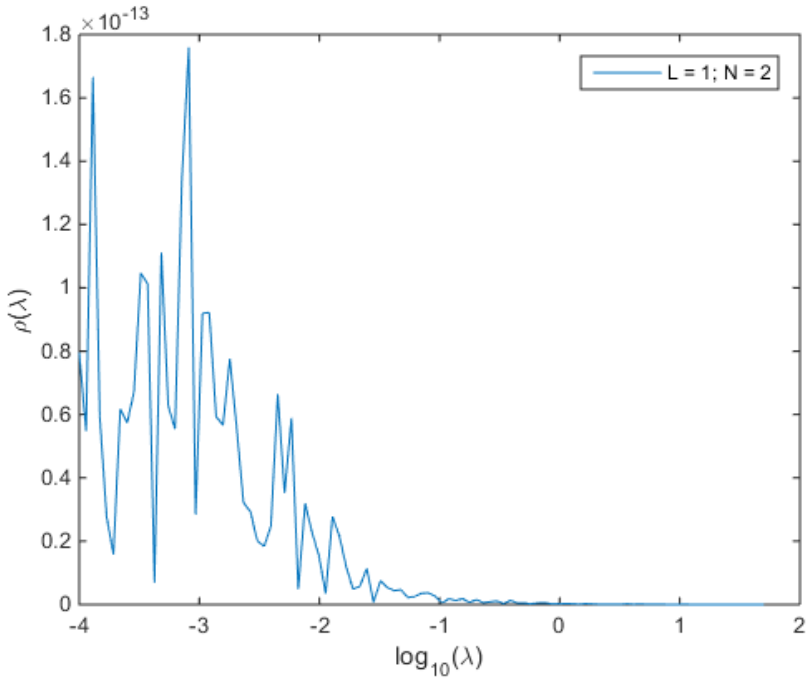

Figure 4.9: SRK - $\eta = 2.836 \times 10^{-4}$ - FPSA - MPD - P_1-S_2 Error Modeled Accurately

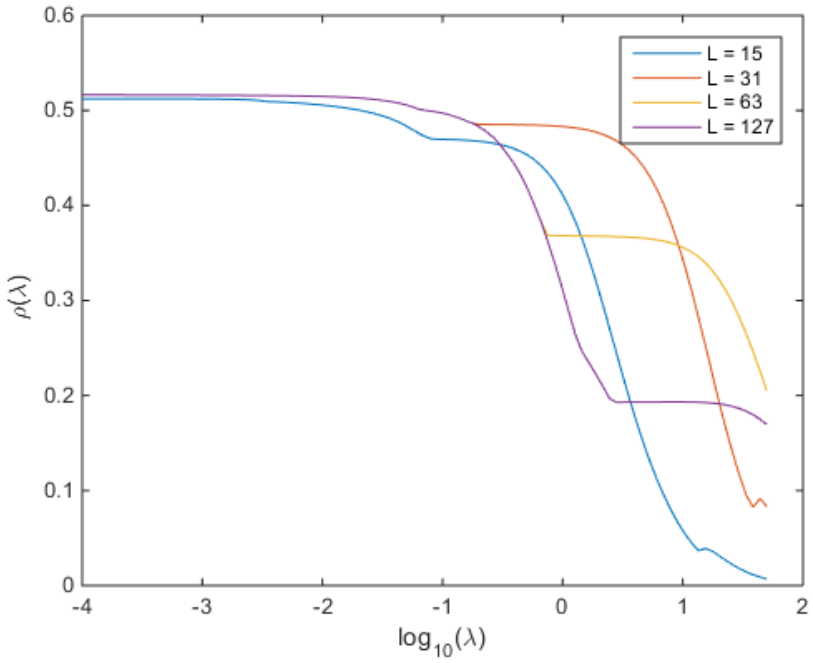

Figure 4.10: SRK - $\eta = 2.836 \times 10^{-4}$ - FPSA - MPD

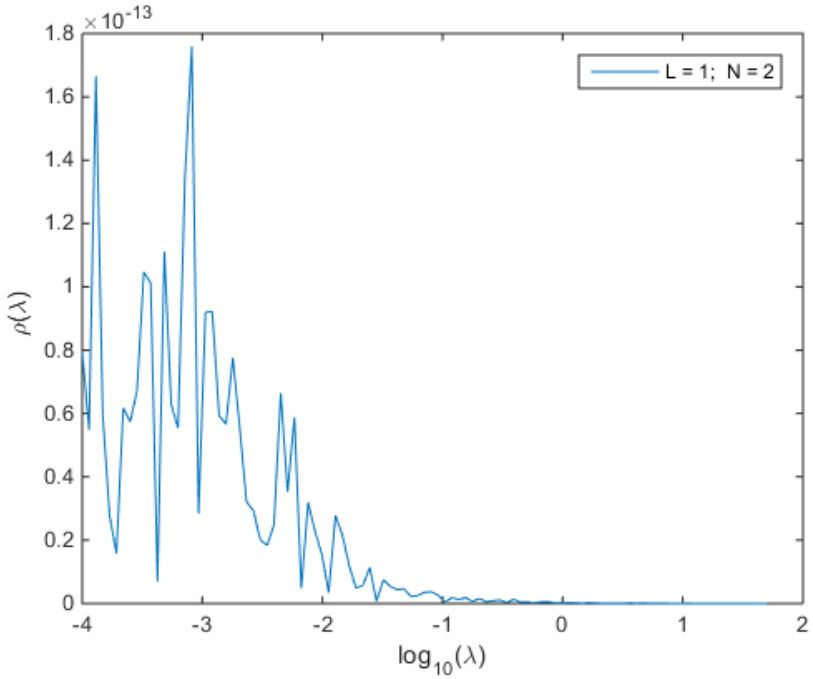

Figure 4.11: SRK - $\eta = 2.836 \times 10^{-4}$ - FPSA - WFD - P_1-S_2 Error Modeled Accurately

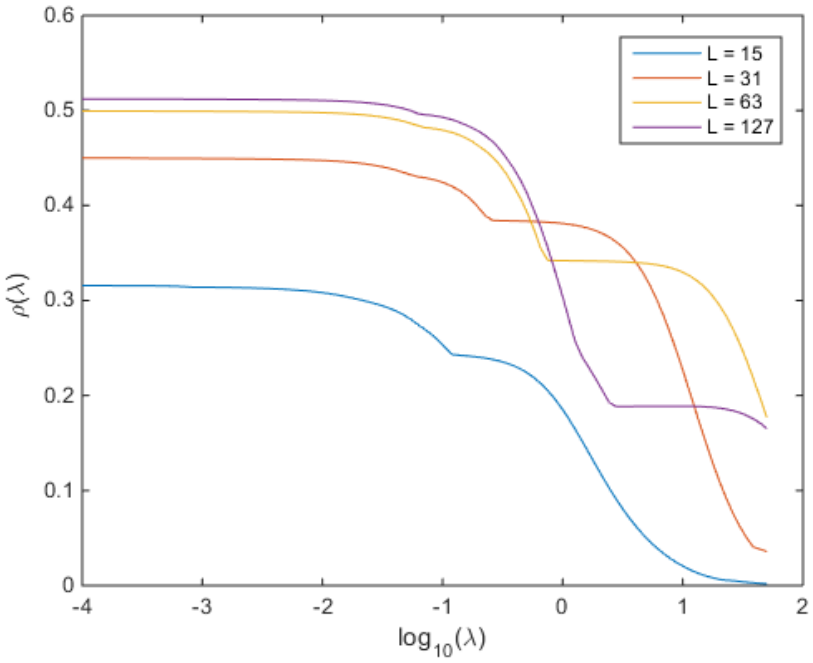

Figure 4.12: SRK - $\eta = 2.836 \times 10^{-4}$ - FPSA - WFD

L	**N**	**FPSA-MPD ρ**	**FPSA-WFD ρ**
1	2	1.7594×10^{-13}	1.7594×10^{-13}
15	16	0.5123	0.3156
31	32	0.5163	0.4500
63	64	0.5163	0.4995
127	128	0.5163	0.5122

Table 4.4: Spectral Radius - SRK $\eta = 2.836 \times 10^{-4}$

Note the near-zero spectral radius value for the $L = 1$, $N = 2$ run. This is because the first two scattering moments are represented exactly by the Fokker-Planck operator. Therefore, as long as $N = 2$, we get convergence in one iteration. Another way to look at this is through FPSA-P_L acceleration equivalence condition we described in Sec. 3.3. We note that Eq. (3.96) always holds for the first two scattering moments. Therefore, for any cross-section kernel, $L_1 - S_2$ solution will always have a zero spectral radius. Moreover we see increasing spectral radius until convergence

with increasing L. This represents convergence in the quality of FP representation of transport error with increasing L for the given scattering cross-section data.

Screening parameter - $\eta = 2.836 \times 10^{-5}$

Next, we choose a smaller screening parameter - $\eta = 2.836 \times 10^{-5}$. The scattering cross-section moments for this screening parameter is given in Table 4.5.

Parameter	**Value**
S_N order	16, 32, 64
σ_a	1
σ_t	13761.18804 cm^{-1}
$\sigma_{s,0}$	13760.18804 cm^{-1}
$\sigma_{s,1}$	13752.79625 cm^{-1}
$\sigma_{s,2}$	13740.35284 cm^{-1}
$\sigma_{s,3}$	13723.63610 cm^{-1}
$\sigma_{s,4}$	13703.16340 cm^{-1}
$\sigma_{s,5}$	13679.32132 cm^{-1}
$\sigma_{s,6}$	13652.41778 cm^{-1}
$\sigma_{s,7}$	13622.70811 cm^{-1}
$\sigma_{s,8}$	13590.40995 cm^{-1}
$\sigma_{s,9}$	13555.71257 cm^{-1}
$\sigma_{s,10}$	13518.78311 cm^{-1}
$\sigma_{s,11}$	13479.77096 cm^{-1}
$\sigma_{s,12}$	13438.81090 cm^{-1}
$\sigma_{s,13}$	13396.02553 cm^{-1}
$\sigma_{s,14}$	13351.52706 cm^{-1}
$\sigma_{s,15}$	13305.41882 cm^{-1}

Table 4.5: Problem Parameters - SRK - $\eta = 2.836 \times 10^{-5}$

$L = 15$**;** $N = 16, 32, 64$

Again, we keep L constant and vary N. The plots obtained from Fourier analyses are presented in Fig. (4.13), (4.14), (4.15), and (4.16). Spectral radius data has been summarized in Table 4.6.

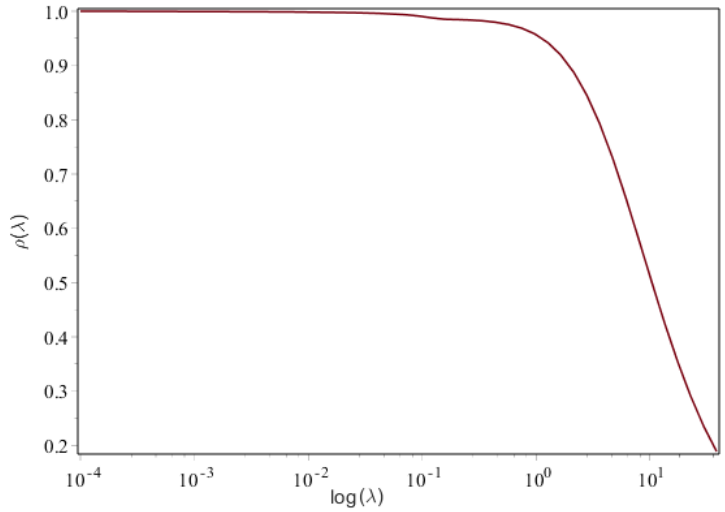

Figure 4.13: SRK - $\eta = 2.836 \times 10^{-5}$ - Unaccelerated - $L = 15$

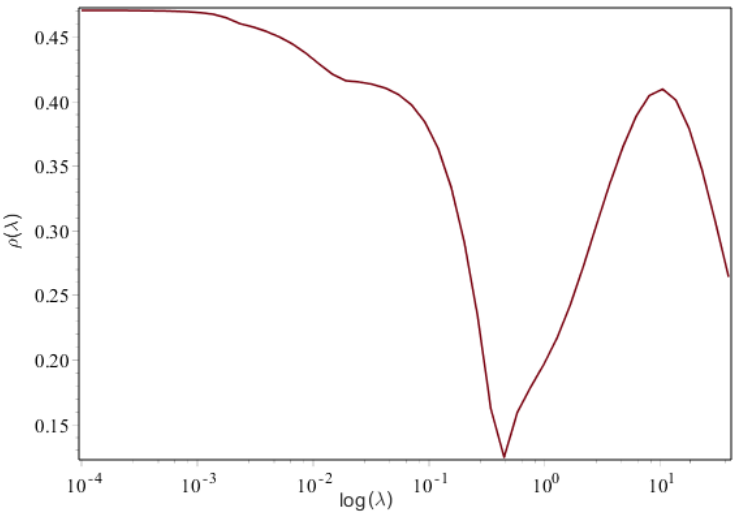

Figure 4.14: SRK - $\eta = 2.836 \times 10^{-5}$ - FPSA - $L = 15$

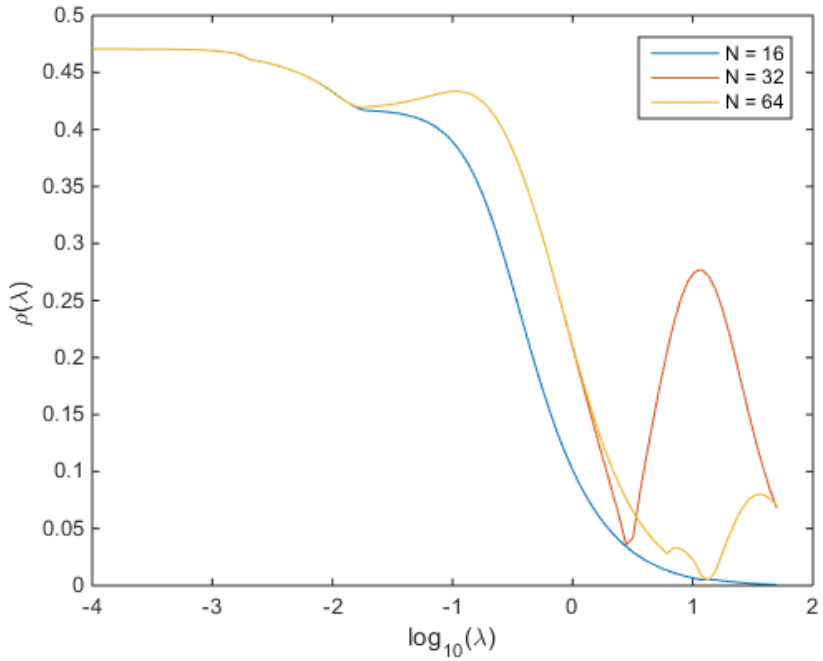

Figure 4.15: SRK - $\eta = 2.836 \times 10^{-5}$ - FPSA - MPD - $L = 15$

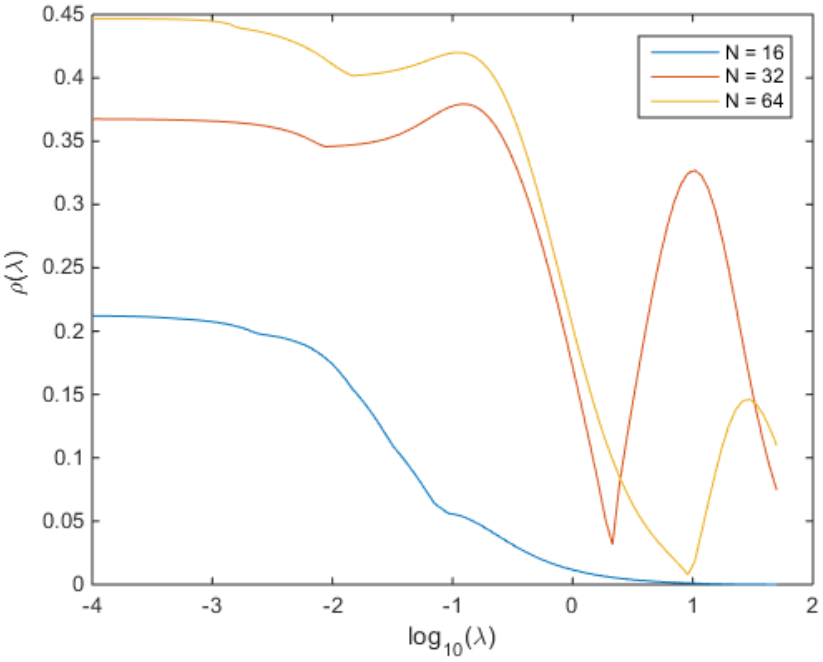

Figure 4.16: SRK - $\eta = 2.836 \times 10^{-5}$ - FPSA - WFD - $L = 15$

N	Unaccelerated ρ	FPSA P_N-based ρ	FPSA-MPD ρ	FPSA-WFD ρ
∞	0.9992	0.4706		
16			0.4706	0.2123
32			0.4706	0.3793
64			0.4706	0.4466

Table 4.6: Spectral Radius - SRK $\eta = 2.836 \times 10^{-5}$ - $L = 15$

We note similar behavior to what we saw for $\eta = 2.836 \times 10^{-4}$. However, one difference we see is a reduction in the spectral radius. This can be attributed to the fact that reducing η results in cross-section coming closer to actually having a Fokker-Planck limit. This means the Fokker-Planck equation will represent the error equation more accurately with decreasing η.

N (= 64) constant and vary L (= 1, 7, 15, 31, 63)

Now, we keep N constant and vary L like before. The plots obtained from Fourier analyses are presented in Fig. 4.17, and 4.18. The information obtained from Fourier analyses is summarized in Table 4.7.

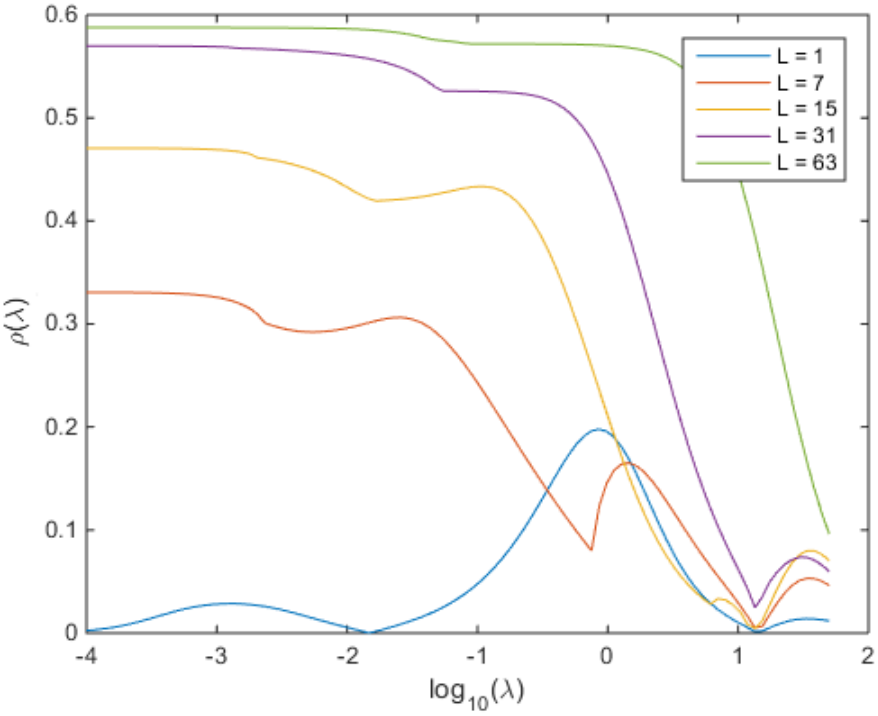

Figure 4.17: SRK - $\eta = 2.836 \times 10^{-5}$ - FPSA - MPD - $N = 64$

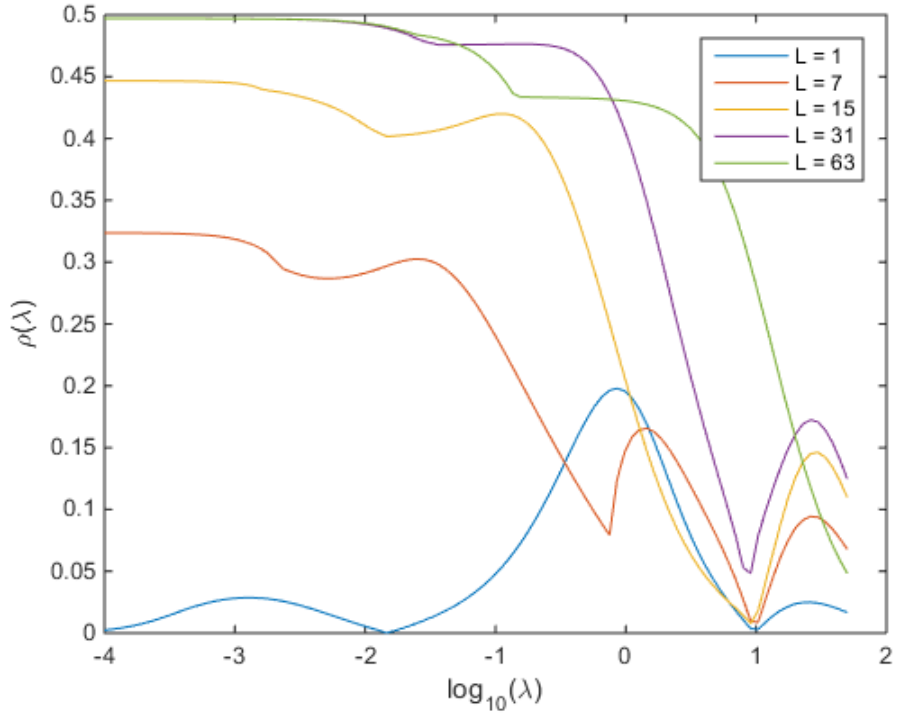

Figure 4.18: SRK - $\eta = 2.836 \times 10^{-5}$ - FPSA - WFD - $N = 64$

L	**FPSA-MPD ρ**	**FPSA-WFD ρ**
1	0.1978	0.1978
7	0.3307	0.3237
15	0.4706	0.4466
31	0.5697	0.4972
63	0.5877	0.4972

Table 4.7: Spectral Radius - SRK $\eta = 2.836 \times 10^{-5}$ - $N = 64$

Again, note convergence in ρ with increasing L. We see exactly the same behavior as we saw before.

Vary N, and L s.t. $L = N - 1$

Now, we vary N and L together. Eigenvalue plots obtained by Fourier analyses have been presented in Fig. 4.19, 4.20, 4.21 and 4.22. The spectral radius information is summarized in Table 4.8.

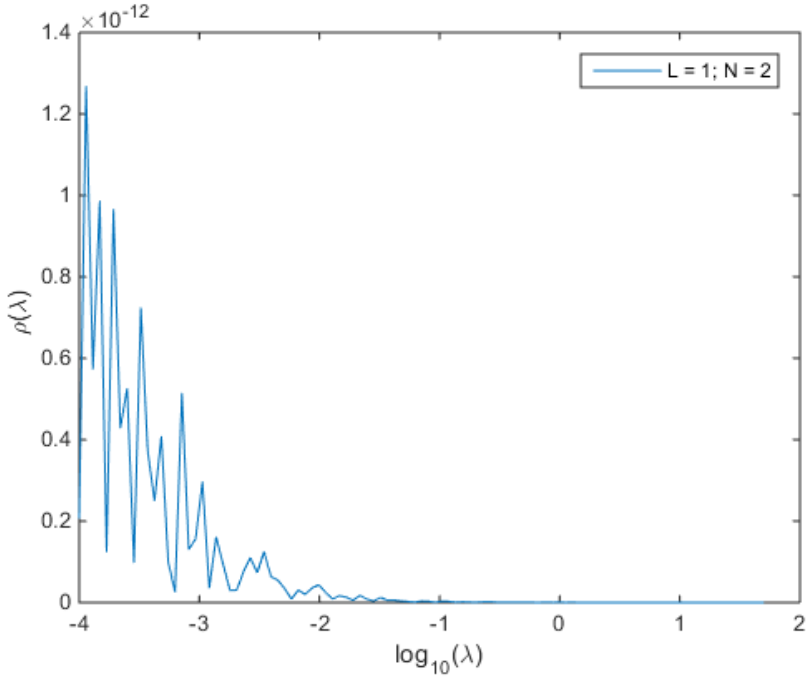

Figure 4.19: SRK - $\eta = 2.836 \times 10^{-5}$ - FPSA - MPD - P_1-S_2 Error Modeled Accurately

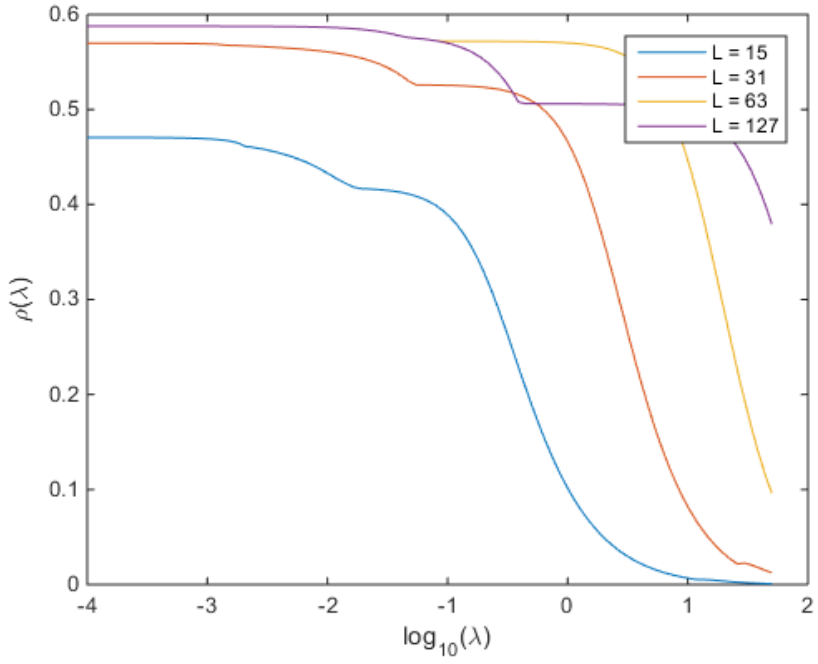

Figure 4.20: SRK - $\eta = 2.836 \times 10^{-5}$ - FPSA - MPD

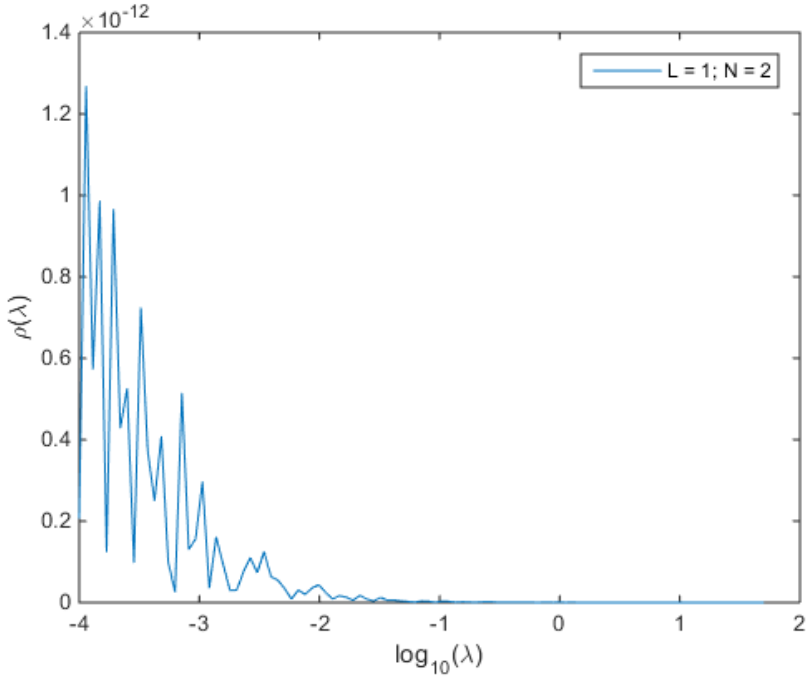

Figure 4.21: SRK - $\eta = 2.836 \times 10^{-5}$ - FPSA - WFD - P_1-S_2 Error Modeled Accurately

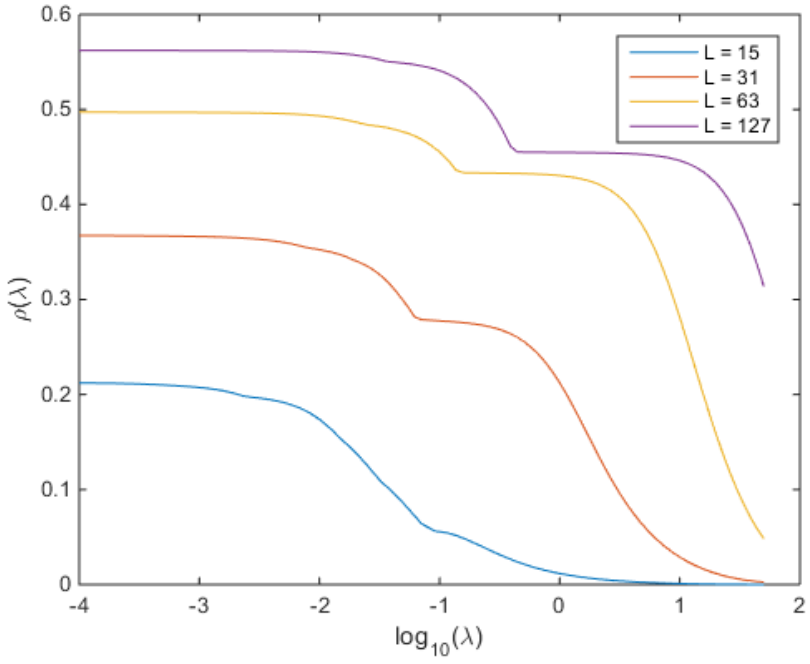

Figure 4.22: SRK - $\eta = 2.836 \times 10^{-5}$ - FPSA - WFD

L	N	FPSA-MPD ρ	FPSA-WFD ρ
1	2	1.268×10^{-12}	1.2683×10^{-12}
15	16	0.4706	0.2123
31	32	0.5697	0.3676
63	64	0.5877	0.4972
127	128	0.5877	0.5622

Table 4.8: Spectral Radius - SRK $\eta = 2.836 \times 10^{-5}$

Increasing L results in increasing spectral radius until convergence of spectral radius in L just like before. We also see a zero spectral radius for the $L_1 - S_2$ problem for the reasons we have already discussed previously.

Screening parameter - $\eta = 2.836 \times 10^{-6}$

Now we choose a smaller screening parameter - $\eta = 2.836 \times 10^{-6}$. The scattering cross-section moments for this screening parameter is given in Table 4.9.

Parameter	Value
S_N order	16, 32, 64
σ_a	1
σ_t	$1.376053926 \times 10^5\ cm^{-1}$
$\sigma_{s,0}$	$1.376053925 \times 10^5\ cm^{-1}$
$\sigma_{s,1}$	$1.375962036 \times 10^5\ cm^{-1}$
$\sigma_{s,2}$	$1.375801671 \times 10^5\ cm^{-1}$
$\sigma_{s,3}$	$1.375580632 \times 10^5\ cm^{-1}$
$\sigma_{s,4}$	$1.375304120 \times 10^5\ cm^{-1}$
$\sigma_{s,5}$	$1.374976030 \times 10^5\ cm^{-1}$
$\sigma_{s,6}$	$1.374599480 \times 10^5\ cm^{-1}$
$\sigma_{s,7}$	$1.374177065 \times 10^5\ cm^{-1}$
$\sigma_{s,8}$	$1.373711006 \times 10^5\ cm^{-1}$
$\sigma_{s,9}$	$1.373203248 \times 10^5\ cm^{-1}$
$\sigma_{s,10}$	$1.372655515 \times 10^5\ cm^{-1}$
$\sigma_{s,11}$	$1.372069359 \times 10^5\ cm^{-1}$
$\sigma_{s,12}$	$1.371446189 \times 10^5\ cm^{-1}$
$\sigma_{s,13}$	$1.370787293 \times 10^5\ cm^{-1}$
$\sigma_{s,14}$	$1.370093861 \times 10^5\ cm^{-1}$
$\sigma_{s,15}$	$1.369366996 \times 10^5\ cm^{-1}$

Table 4.9: Problem Parameters - SRK - $\eta = 2.836 \times 10^{-6}$

Keep $L(=15)$ Constant, and Vary N (= 16, 32, 64)

First, we keep L constant and vary N. The plots obtained from Fourier analyses are presented in Fig. (4.23), (4.24), (4.25), and (4.26). Spectral radius data has been summarized in Table 4.10.

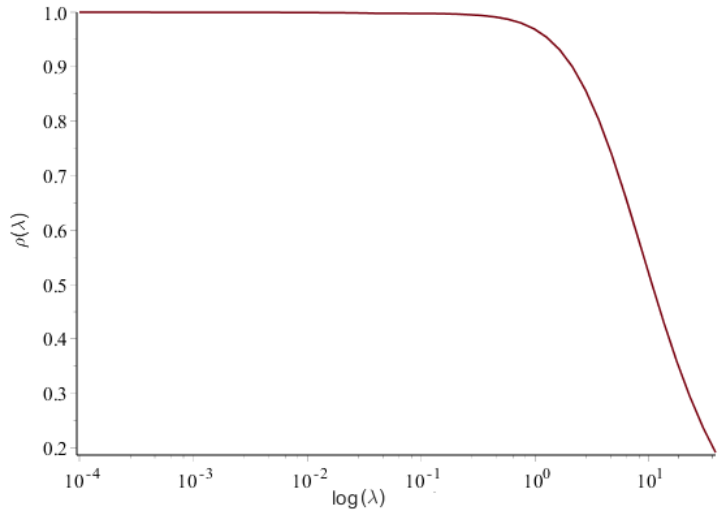

Figure 4.23: SRK - $\eta = 2.836 \times 10^{-6}$ - Unaccelerated - $L = 15$

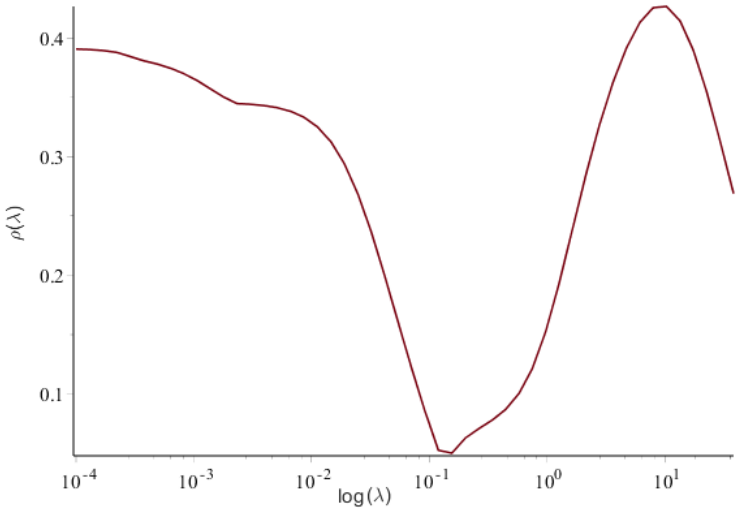

Figure 4.24: SRK - $\eta = 2.836 \times 10^{-6}$ - FPSA - $L = 15$

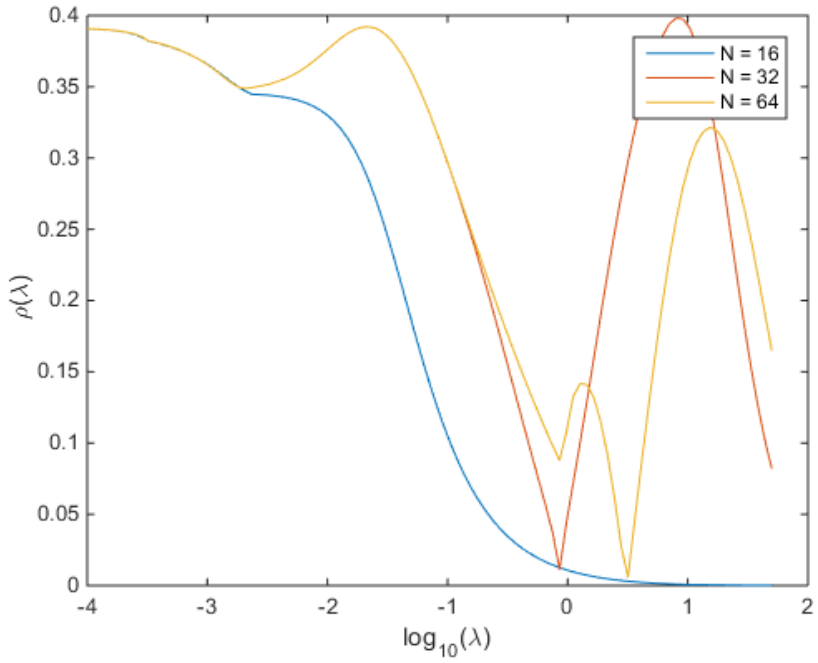

Figure 4.25: SRK - $\eta = 2.836 \times 10^{-6}$ - FPSA - MPD - $L = 15$

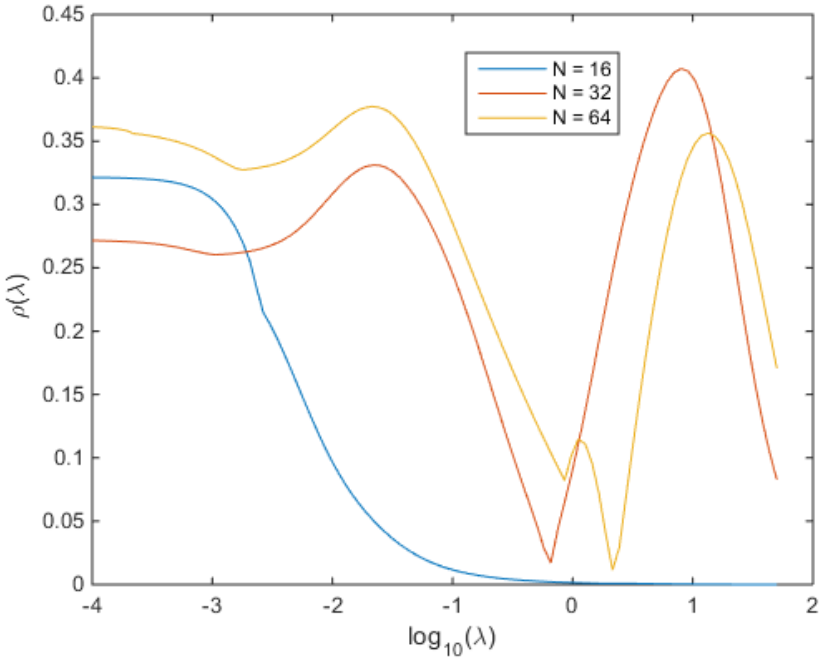

Figure 4.26: SRK - $\eta = 2.836 \times 10^{-6}$ - FPSA - WFD - $L = 15$

N	**Unaccelerated** ρ	**FPSA** P_N**-based** ρ	**FPSA-MPD** ρ	**FPSA-WFD** ρ
∞	0.9999	0.4266		
16			0.3906	0.3215
32			0.3982	0.4072
64			0.3921	0.3773

Table 4.10: Spectral Radius - SRK - $\eta = 2.836 \times 10^{-6}$ - $L = 15$

We note the further decrease in spectral radius, for a given (low) L, than for the previous two η's. This is because the lower FP moments, now, represent the transport moments more closely.

$N(= 64)$ **constant and vary** $L(= 1, 7, 15, 31, 63)$

Again, we will vary L while keeping N constant. The plots obtained from Fourier analyses are presented in Fig. 4.27, and 4.28. The information obtained from Fourier analyses is summarized in Table 4.11. We note convergence in ρ with increasing L.

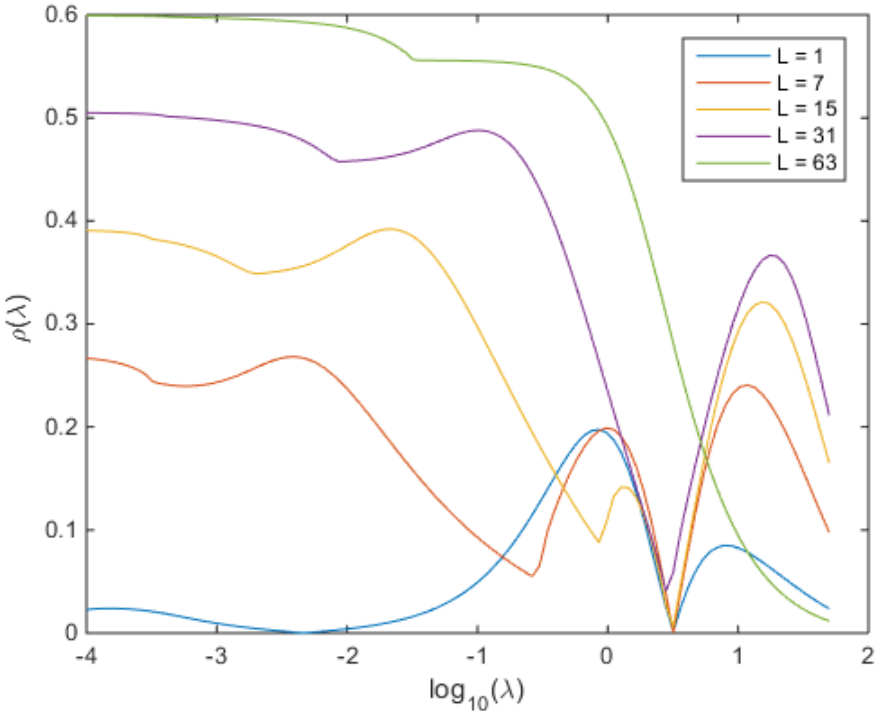

Figure 4.27: SRK - $\eta = 2.836 \times 10^{-6}$ - FPSA - MPD - $N = 64$

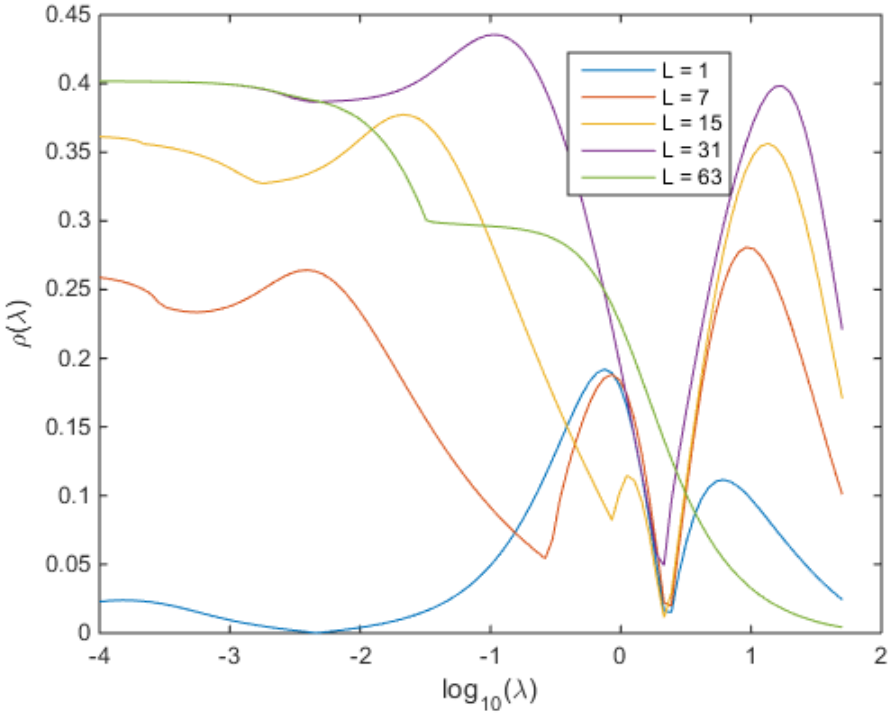

Figure 4.28: SRK - $\eta = 2.836 \times 10^{-6}$ - FPSA - WFD - $N = 64$

L	**FPSA-MPD ρ**	**FPSA-WFD ρ**
1	0.1976	0.1920
7	0.2681	0.2807
15	0.3921	0.3773
31	0.5048	0.4356
63	0.5990	0.4018

Table 4.11: Spectral Radius - SRK $\eta = 2.836 \times 10^{-6}$ - $N = 64$

The scattering kernel is so forward-peaked in this case that the number of flux moments (15) is not enough to accurately represent the angular dependence of the angular flux. As we discussed in previous section, in continuous case, there are residual terms that do not cancel out in the derivation of Fokker-Planck equation if sufficient number of moments are not accounted for. These residual terms do not exist in the discrete case, however. Therefore, the continuous FPSA analysis

will be inherently inconsistent with the angularly-discrete case when sufficient number of moments are not considered. This is the reason behind the behavior we see here.

Vary N, and L s.t. $L = N - 1$

Finally, we vary N and L together. Eigenvalue plots obtained by Fourier analyses have been presented in Fig. 4.29, 4.30, 4.31 and 4.22. The spectral radius information is summarized in Table 4.12.

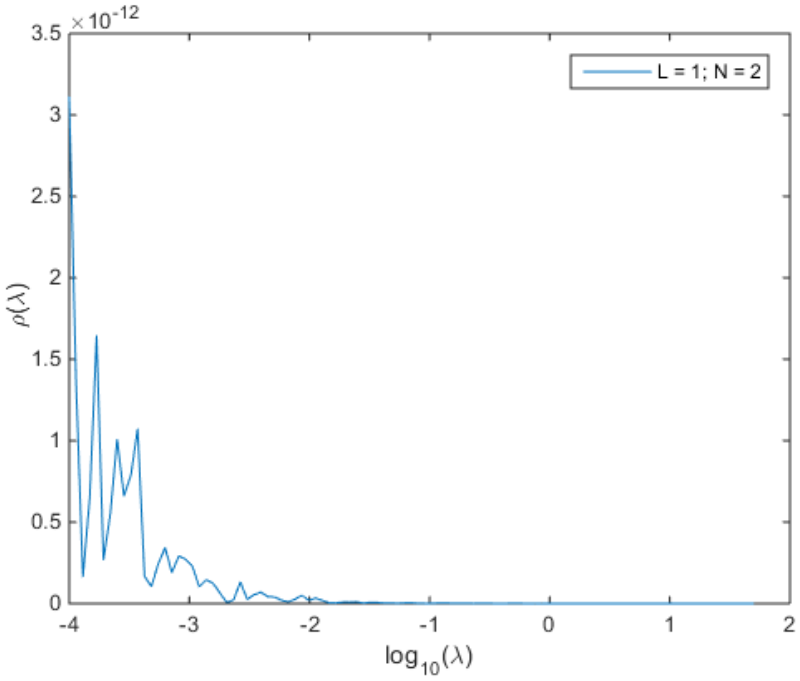

Figure 4.29: SRK - $\eta = 2.836 \times 10^{-6}$ - FPSA - MPD - P_1-S_2 Error Modeled Accurately

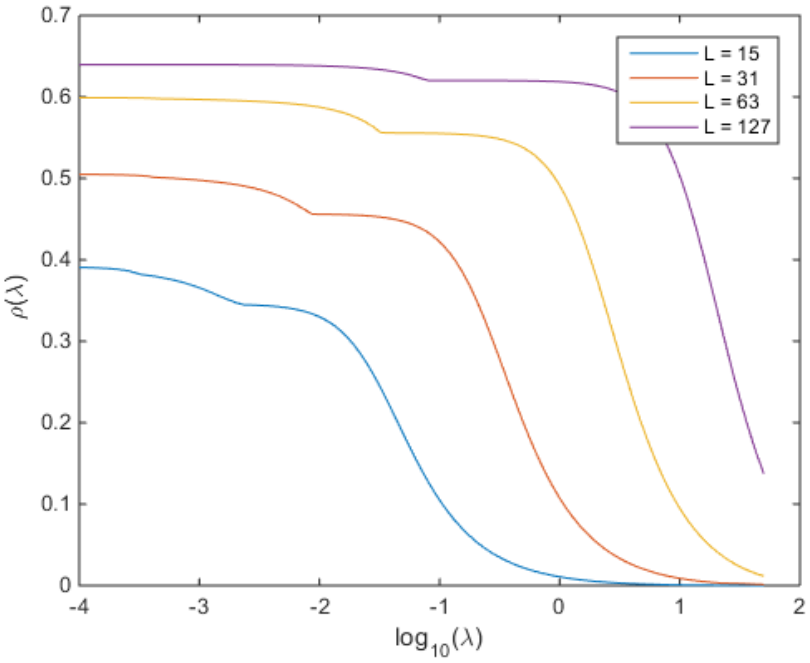

Figure 4.30: SRK - $\eta = 2.836 \times 10^{-6}$ - FPSA - MPD

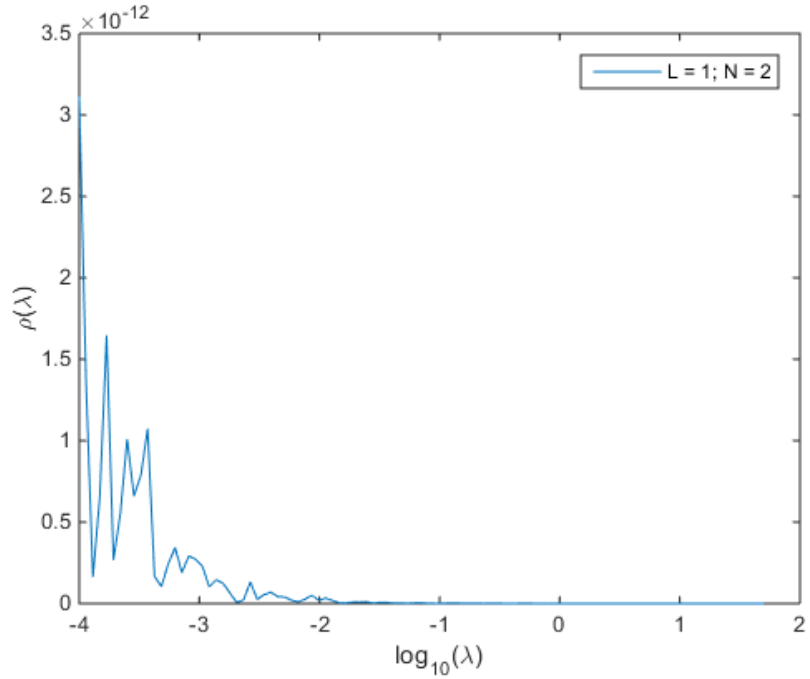

Figure 4.31: SRK - $\eta = 2.836 \times 10^{-6}$ - FPSA - WFD - P_1-S_2 Error Modeled Accurately

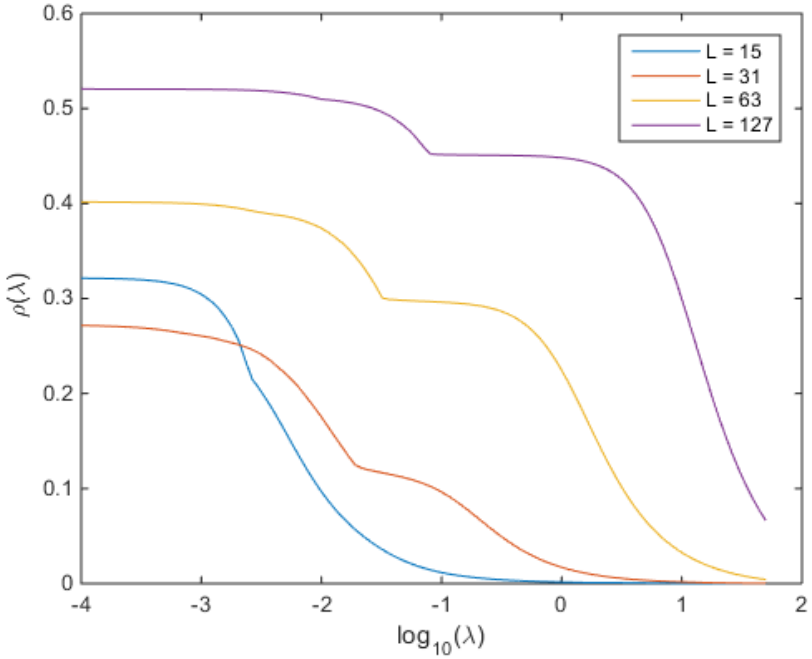

Figure 4.32: SRK - $\eta = 2.836 \times 10^{-6}$ - FPSA - WFD

L	**N**	**FPSA-MPD** ρ	**FPSA-WFD** ρ
1	2	3.1132×10^{-12}	1.2683×10^{-12}
15	16	0.3906	0.3215
31	32	0.5048	0.2727
63	64	0.5990	0.4018
127	128	0.6395	0.5205

Table 4.12: Spectral Radius - SRK $\eta = 2.836 \times 10^{-6}$

We see similar behavior as before. However, here, we see a high spectral radius value for the highest represented L. This is a result of higher error moments not being represented accurately by FP.

In summary we see that for screened Rutherford kernel, FPSA can potentially provide a good speed up (at least with respect to number of iteration to convergence) irrespective of N, L and η.

4.4.2 Exponential Kernel (EK)

Now, we look at the the exponential kernel. we choose parameter Δ [8] to be 10^{-6}, and 10^{-9}. We calculate $\sigma_{s,0}$ using Screened Rutherford Kernel where $\sigma_{s,0} = 13761.95103$. Like for the screened Rutherford kernel, run convergence rate calculations where we keep L constant while increasing N. We will also vary L and N together such that $L = N - 1$. However, we will not present data where we keep N constant and increase L for convenience.

$\Delta = 10^{-6}$

First we choose $\Delta = 10^{-6}$. The scattering cross-section moments for these parameters are given in Table 4.13. Note that we only present data for the first 16 moments. Higher moments are presented in Appendix B.

Parameter	**Value**
S_N order	16, 32, 64
σ_a	1
σ_t	13762.95103 cm^{-1}
$\sigma_{s,0}$	13761.95103 cm^{-1}
$\sigma_{s,1}$	13761.93727 cm^{-1}
$\sigma_{s,2}$	13761.90975 cm^{-1}
$\sigma_{s,3}$	13761.85470 cm^{-1}
$\sigma_{s,4}$	13761.81341 cm^{-1}
$\sigma_{s,5}$	13761.75837 cm^{-1}
$\sigma_{s,6}$	13761.67579 cm^{-1}
$\sigma_{s,7}$	13761.60699 cm^{-1}
$\sigma_{s,8}$	13761.52442 cm^{-1}
$\sigma_{s,9}$	13761.41432 cm^{-1}
$\sigma_{s,10}$	13761.31799 cm^{-1}
$\sigma_{s,11}$	13761.20790 cm^{-1}
$\sigma_{s,12}$	13761.07029 cm^{-1}
$\sigma_{s,13}$	13760.94644 cm^{-1}
$\sigma_{s,14}$	13760.80883 cm^{-1}
$\sigma_{s,15}$	13760.64370 cm^{-1}

Table 4.13: Problem Parameters - EK - $\Delta = 10^{-6}$

Keep L (= 15) Constant, and Vary $N(= 16, 32, 64)$

We keep L constant and vary N. The plots obtained from Fourier analyses are presented in Fig. 4.33, 4.34, 4.35, and 4.36. The information obtained from Fourier analyses is summarized in Table 4.14.

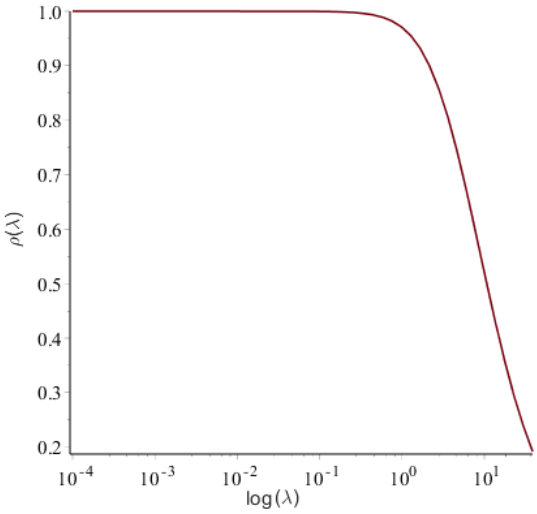

Figure 4.33: EK - $\Delta = 10^{-6}$ - Unaccelerated - $L = 15$

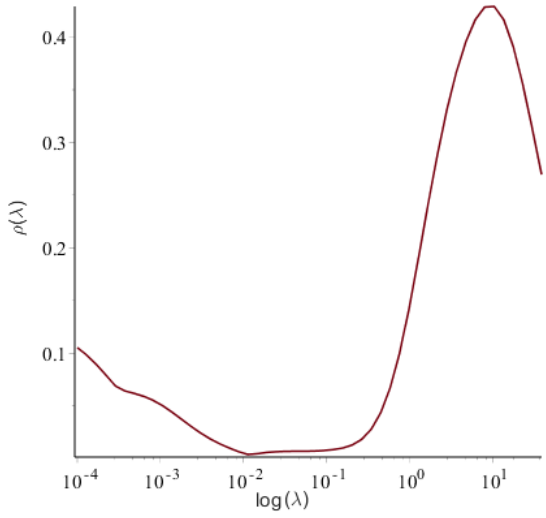

Figure 4.34: EK - $\Delta = 10^{-6}$ - FPSA - $L = 15$

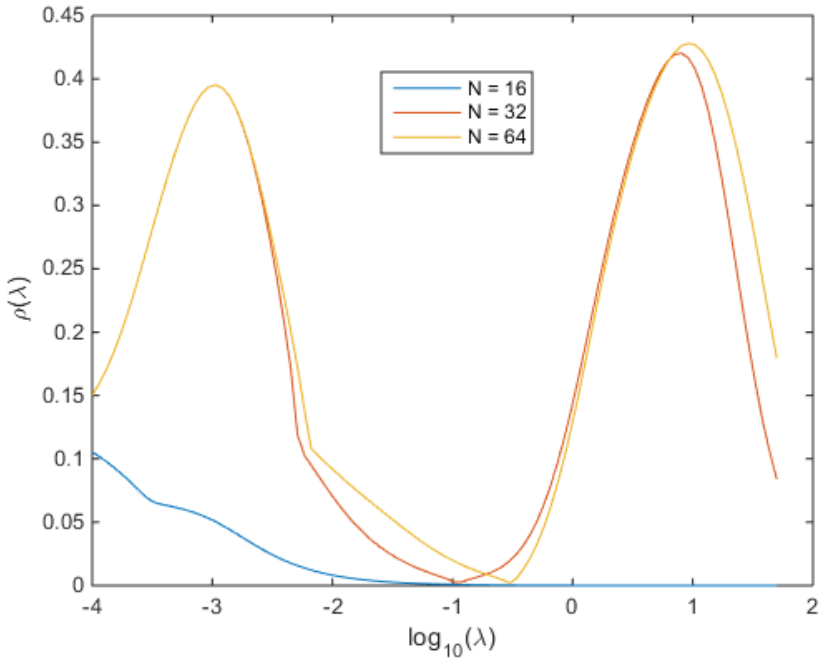

Figure 4.35: EK - $\Delta = 10^{-6}$ - FPSA - MPD - $L = 15$

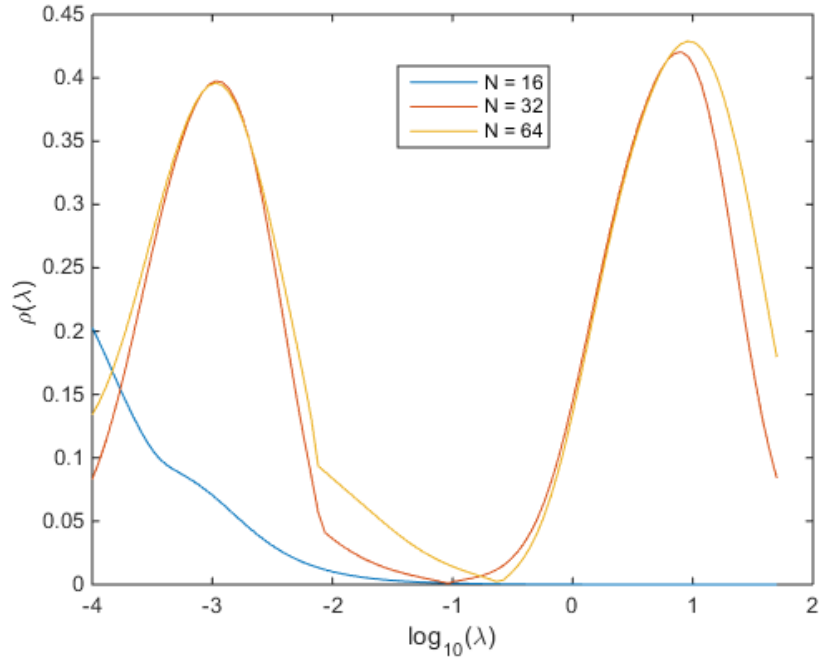

Figure 4.36: EK - $\Delta = 10^{-6}$ - FPSA - WFD - $L = 15$

N	Unaccelerated ρ	FPSA P_N-based ρ	FPSA-MPD ρ	FPSA-WFD ρ
∞	0.9999	0.4291		
16			0.1053	0.3135
32			0.4203	0.4204
64			0.4279	0.4288

Table 4.14: Spectral Radius - EK $\Delta = 10^{-6}$ - $L = 15$

We see converging spectral radius with N. Moreover, they converge to the analytical spectral radius because EK has a valid FP limit.

Vary N, and L s.t. $L = N - 1$

Now, we vary N and L together. $N = 2, 16, 32, 64, 128$ and $L = 1, 16, 31, 63, 127$. Eigenvalue plots obtained by Fourier analyses have been presented in Fig. 4.37, 4.39, 4.39 and 4.40. The spectral radius information is summarized in Table 4.15.

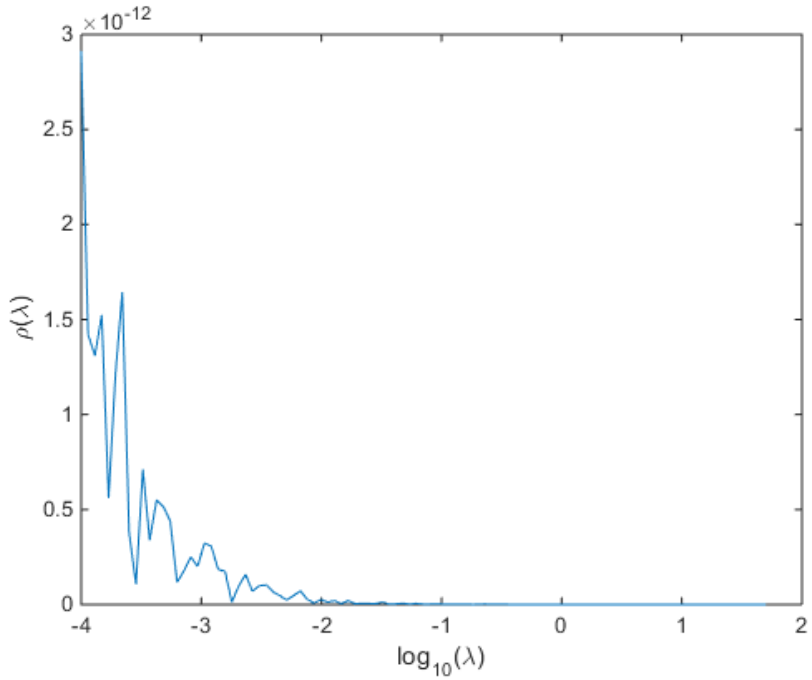

Figure 4.37: EK - $\Delta = 10^{-6}$ - FPSA - MPD - P_1-S_2 Error Modeled Accurately

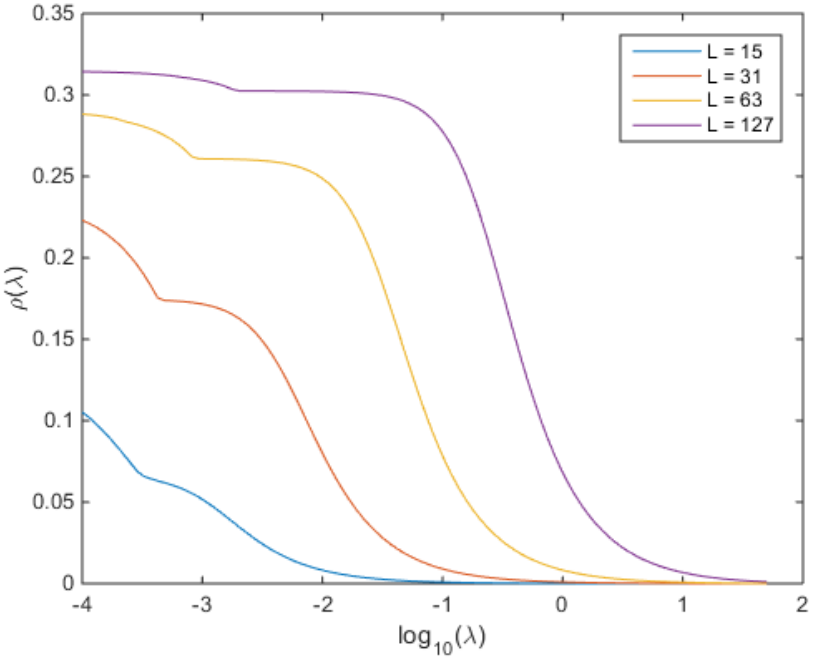

Figure 4.38: EK - $\Delta = 10^{-6}$ - FPSA - MPD

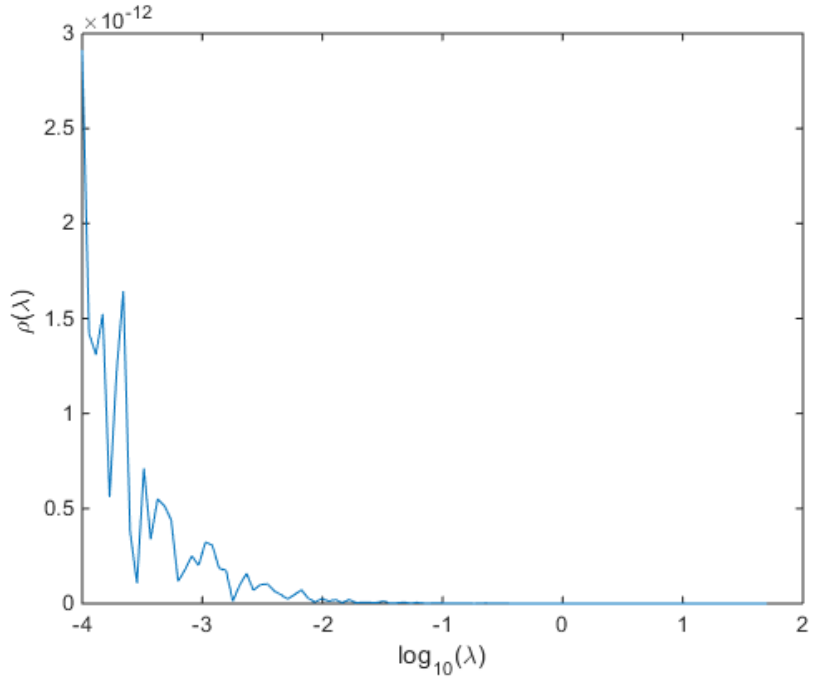

Figure 4.39: EK - $\Delta = 10^{-6}$ - FPSA - WFD - P_1-S_2 Error Modeled Accurately

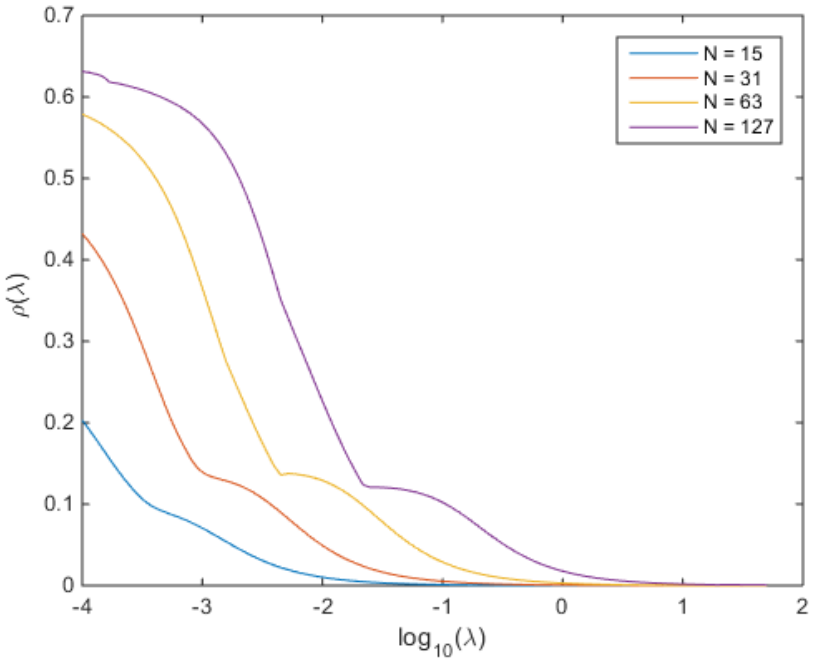

Figure 4.40: EK - $\Delta = 10^{-6}$ - FPSA - WFD

L	**N**	**FPSA-MPD ρ**	**FPSA-WFD ρ**
1	2	2.9131×10^{-12}	2.9131×10^{-12}
15	16	0.1053	0.3135
31	32	0.2230	0.5131
63	64	0.2882	0.6142
127	128	0.3143	0.6352

Table 4.15: Spectral Radius - EK $\Delta = 10^{-6}$

We see an increasing spectral radius with increasing L just like for SRK. The spectral radii are significantly different for MPD and WFD because, for this particular cross-section set because of the difference in the number of FP moments accurately represented by MPD and WFD.

$\Delta = 10^{-9}$

Now, we choose parameter Δ [8] to be 10^{-9}. Note that as $\Delta \to 0$, transport limits to FP because the exponential kernel has a valid FP limit. The scattering cross-section moments for these parameters are given in Table 4.16. Note that we only present data for the first 16 moments. Higher moments are presented in Appendix B.

Parameter	**Value**
S_N order	16, 32, 64
σ_a	1
σ_t	13762.95103 cm^{-1}
$\sigma_{s,0}$	13761.95103 cm^{-1}
$\sigma_{s,1}$	13761.95102 cm^{-1}
$\sigma_{s,2}$	13761.95099 cm^{-1}
$\sigma_{s,3}$	13761.95094 cm^{-1}
$\sigma_{s,4}$	13761.95089 cm^{-1}
$\sigma_{s,5}$	13761.95084 cm^{-1}
$\sigma_{s,6}$	13761.95076 cm^{-1}
$\sigma_{s,7}$	13761.95069 cm^{-1}
$\sigma_{s,8}$	13761.95061 cm^{-1}
$\sigma_{s,9}$	13761.95050 cm^{-1}
$\sigma_{s,10}$	13761.95040 cm^{-1}
$\sigma_{s,11}$	13761.95029 cm^{-1}
$\sigma_{s,12}$	13761.95015 cm^{-1}
$\sigma_{s,13}$	13761.95003 cm^{-1}
$\sigma_{s,14}$	13761.94989 cm^{-1}
$\sigma_{s,15}$	13761.94972 cm^{-1}

Table 4.16: Problem Parameters - EK - $\Delta = 10^{-9}$

Keep $L(= 15)$ Constant, and Vary $N(= 16, 32, 64)$

First, we keep L constant and vary N. The plots obtained from Fourier analyses are presented in Fig. 4.41, 4.42, 4.43, and 4.44. The information obtained from Fourier analyses is summarized in Table 4.17.

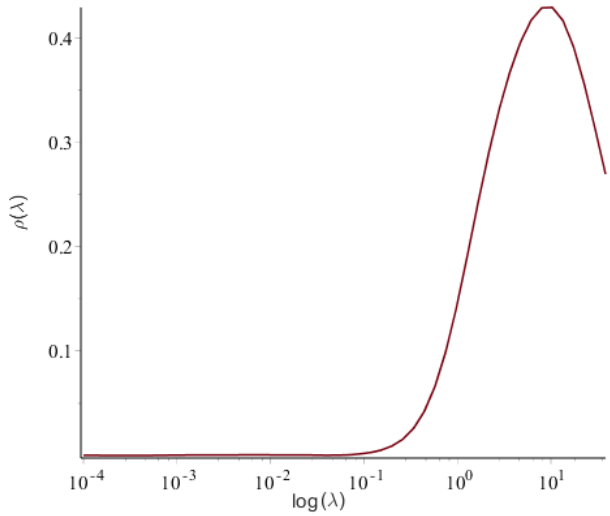

Figure 4.41: EK - $\Delta = 10^{-9}$ - Unaccelerated - $L = 15$

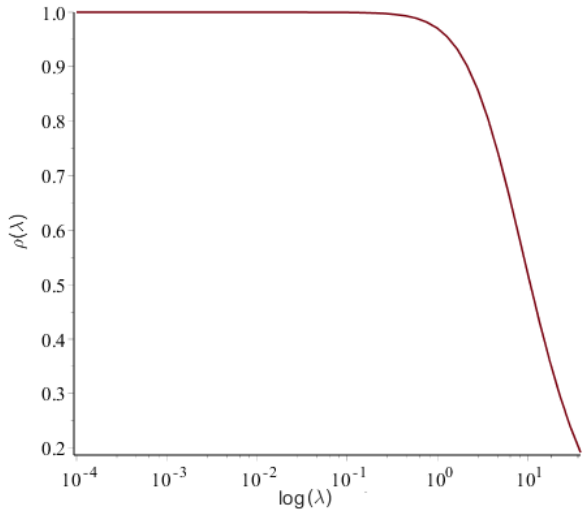

Figure 4.42: EK - $\Delta = 10^{-9}$ - FPSA - $L = 15$

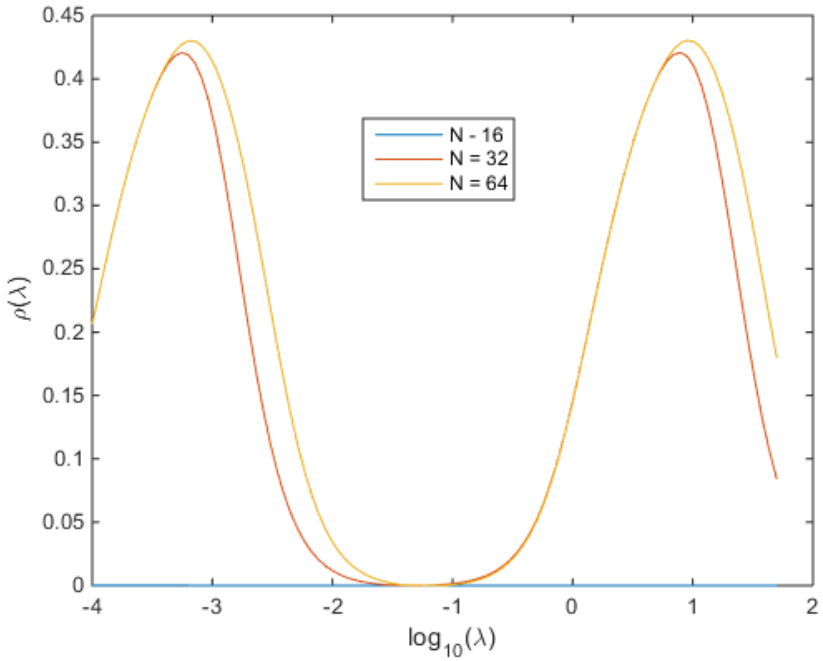

Figure 4.43: EK - $\Delta = 10^{-9}$ - FPSA - MPD - $L = 15$

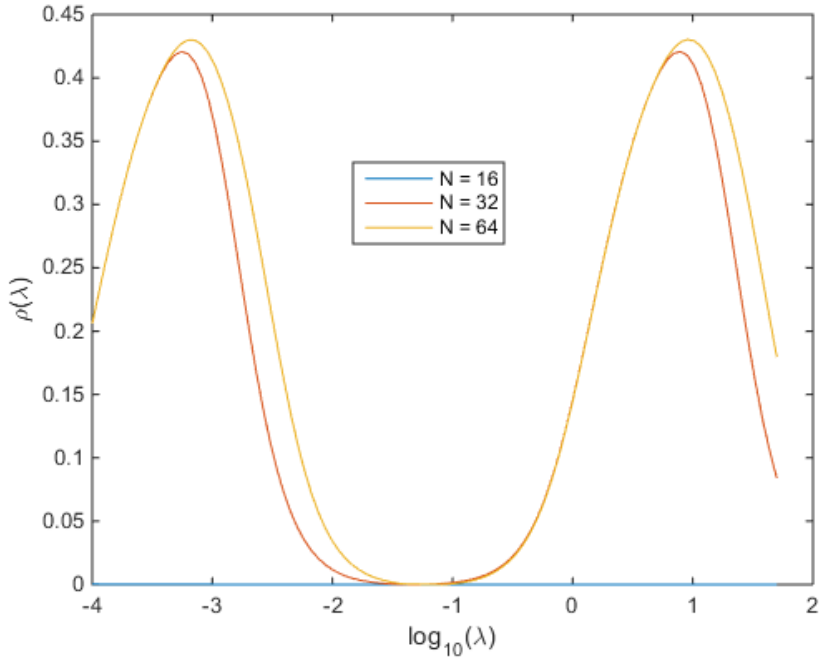

Figure 4.44: EK - $\Delta = 10^{-9}$ - FPSA - WFD - $L = 15$

N	Unaccelerated ρ	FPSA P_N-based ρ	FPSA-MPD ρ	FPSA-WFD ρ
∞	0.9999	0.4291		
16			1.8898×10^{-4}	5.503×10^{-4}
32			0.4206	0.4206
64			0.4303	0.4303

Table 4.17: Spectral Radius - EK $\Delta = 10^{-6}$ - $L = 15$

Vary N, and L s.t. $L = N - 1$

Now, we vary N and L together. $N = 2, 16, 32, 64, 128$ and $L = 1, 16, 31, 63, 127$. Eigenvalue plots obtained by Fourier analyses have been presented in 4.45 and 4.40. The spectral radius information is summarized in Table 4.18.

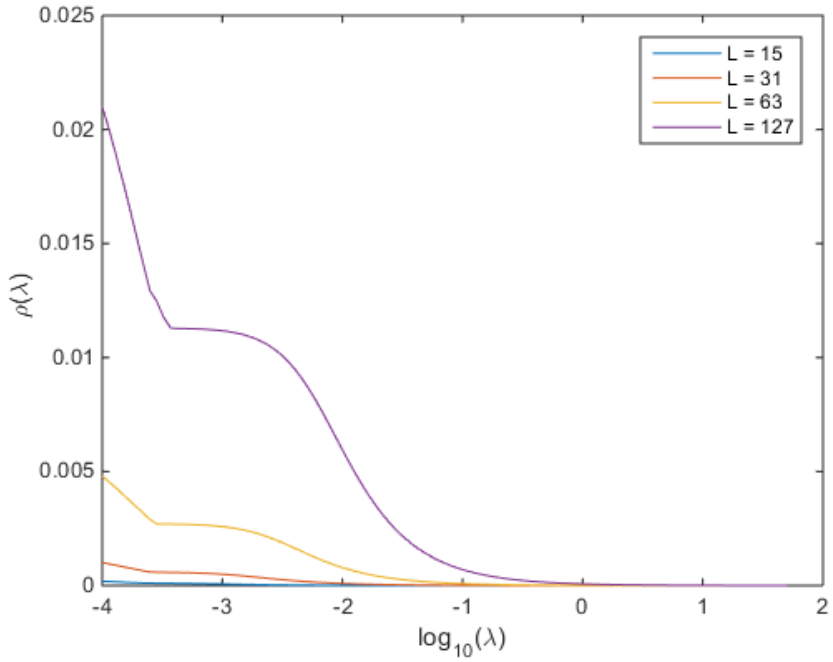

Figure 4.45: EK - $\Delta = 10^{-9}$ - FPSA - MPD

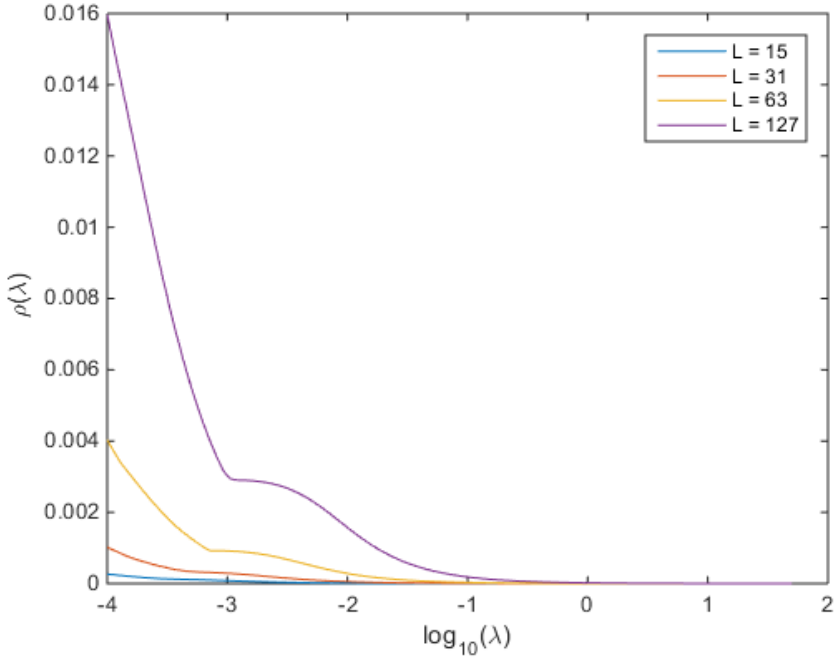

Figure 4.46: EK - $\Delta = 10^{-9}$ - FPSA - WFD

L	**N**	**FPSA-MPD** ρ	**FPSA-WFD** ρ
1	2	1.8800×10^{-12}	1.8800×10^{-12}
15	16	1.8898×10^{-4}	5.5038×10^{-4}
31	32	0.0010	0.0020
63	64	0.0047	0.0076
127	128	0.0210	0.0289

Table 4.18: Spectral Radius - EK $\Delta = 10^{-9}$

We note the extremely small spectral radii with simultaneous increase of N and L such that $N = L + 1$. This is attributed to the fact that the FP approximation, in this case, represents transport error accurately in limit $\Delta \to 0$ because EK has a valid FP limit.

4.4.3 Henyey-Greenstein Kernel (HGK)

The Henyey-Greenstein kernel famously does not have a Fokker-Planck limit [4] as $g \to 1$. First, we choose the asymmetry parameter, g = 0.5 and 0.9999. The scattering cross-section moments for these parameters are given in Table 4.19. Note that we only present data for the first 16 moments.

Parameter	**Value**
S_N order	16, 32, 64
σ_a	0.00001
σ_t	1.00001 cm^{-1}
$\sigma_{s,0}$	1.0 cm^{-1}
$\sigma_{s,1}$	0.5000000000 cm^{-1}
$\sigma_{s,2}$	0.2500000000 cm^{-1}
$\sigma_{s,3}$	0.1250000000 cm^{-1}
$\sigma_{s,4}$	0.6250000000e-1 cm^{-1}
$\sigma_{s,5}$	0.3125000000e-1 cm^{-1}
$\sigma_{s,6}$	0.1562500000e-1 cm^{-1}
$\sigma_{s,7}$	0.7812500000e-2 cm^{-1}
$\sigma_{s,8}$	0.3906250000e-2 cm^{-1}
$\sigma_{s,9}$	0.1953125000e-2 cm^{-1}
$\sigma_{s,10}$	0.9765625000e-3 cm^{-1}
$\sigma_{s,11}$	0.4882812500e-3 cm^{-1}
$\sigma_{s,12}$	0.2441406250e-3 cm^{-1}
$\sigma_{s,13}$	0.1220703125e-3 cm^{-1}
$\sigma_{s,14}$	0.6103515625e-4 cm^{-1}
$\sigma_{s,15}$	0.3051757812e-4 cm^{-1}

Table 4.19: Problem Parameters - HGK - $g = 0.5$

Keep $L(= 15)$ Constant, and Vary $N(= 16, 32, 64)$

First, we keep L constant and vary N. The plots obtained from Fourier analyses are presented in Fig. 4.47, 4.48, 4.49, and 4.50. The information obtained from Fourier analyses is summarized in Table 4.20.

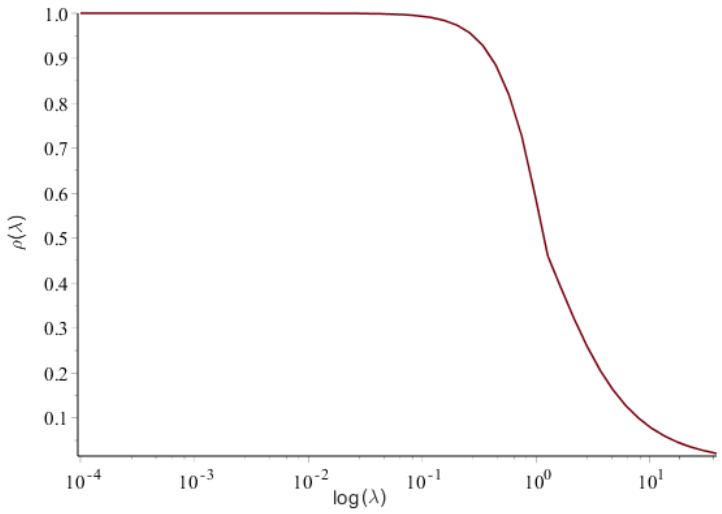

Figure 4.47: EK - g = 0.5 - Unaccelerated - $L = 15$

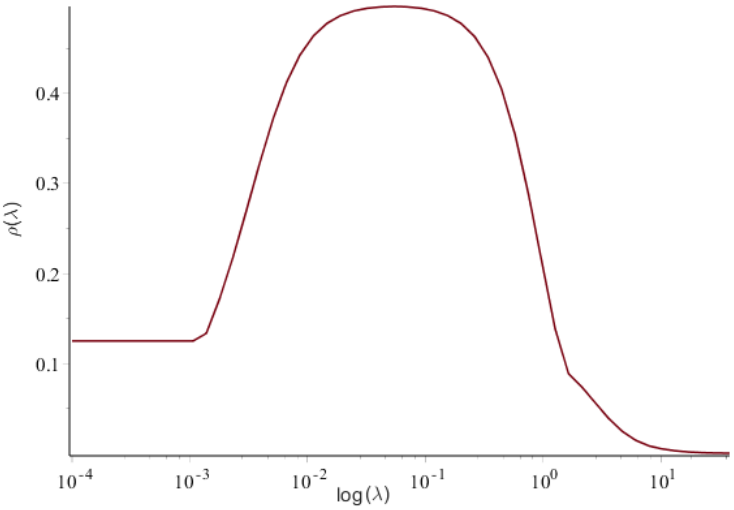

Figure 4.48: HGK - g = 0.5 - FPSA - $L = 15$

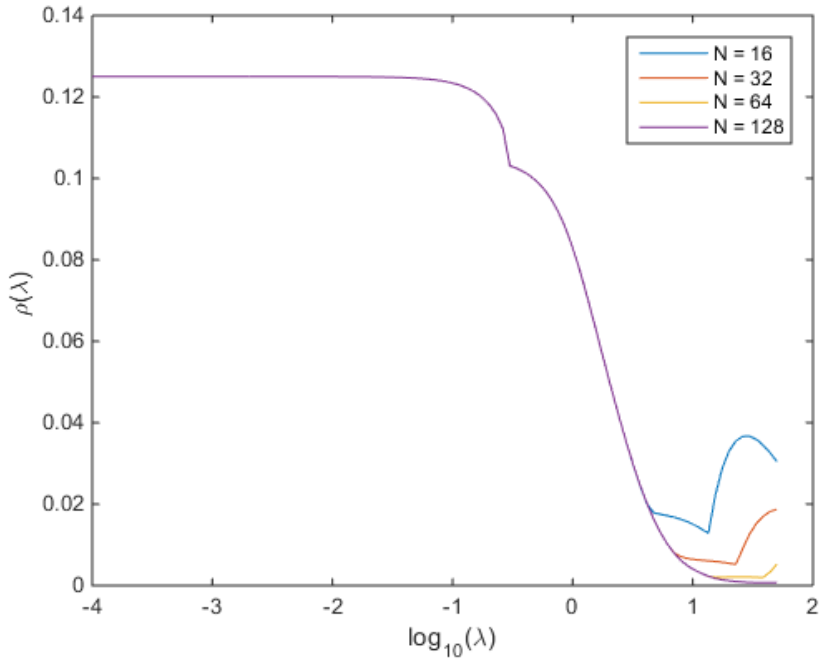

Figure 4.49: HGK - g = 0.5 - FPSA - MPD - $L = 15$

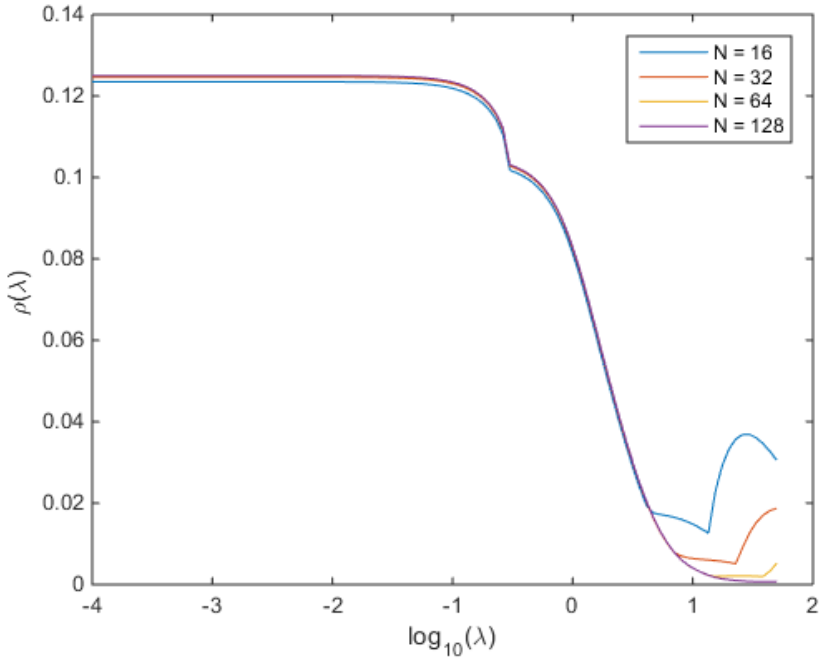

Figure 4.50: HGK - g = 0.5 - FPSA - WFD - $L = 15$

N	Unaccelerated ρ	FPSA P_N-based ρ	FPSA-MPD ρ	FPSA-WFD ρ
∞	0.9999	0.4966		
16			0.1249	0.1234
32			0.1249	0.1246
64			0.1249	0.1248
128			0.1249	0.1249

Table 4.20: Spectral Radius - HGK - g = 0.5 - $L = 15$

Note the drastic difference between the angularly continuous and angularly discrete spectral radii. The scattering kerner, here, does not have a valid FP limit which results in inconsistency between continuous and discrete representation of transport and FP equation. This is the reason behind the difference in spectral radii.

Vary N, and L s.t. $L = N - 1$

Now, we vary N and L together. $N = 2, 16, 32, 64, 128$ and $L = 1, 16, 31, 63, 127$. Eigenvalue plots obtained by Fourier analyses have been presented in Fig. 4.51 and. The spectral radius information is summarized in Table 4.21.

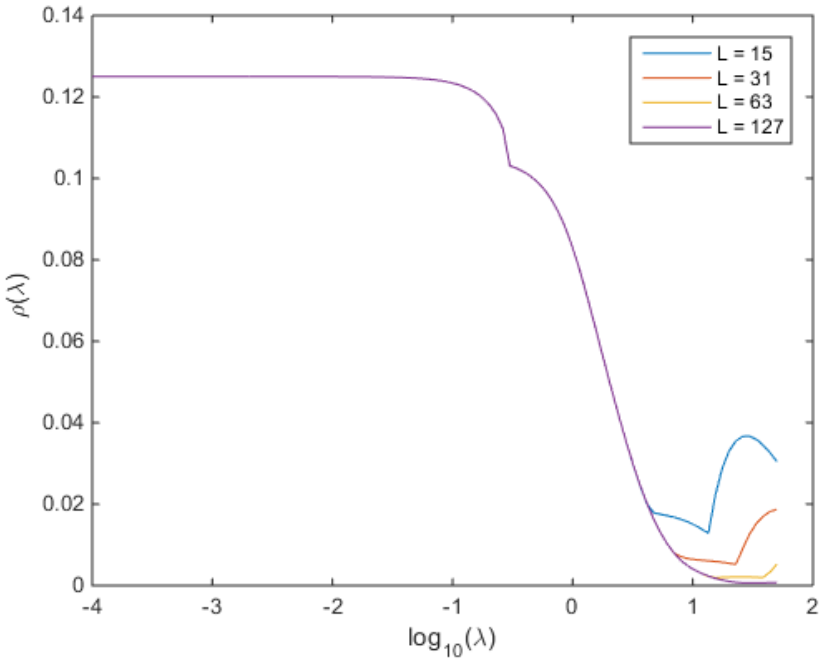

Figure 4.51: Spectral Radius - HGK - g = 5 - FPSA - MPD

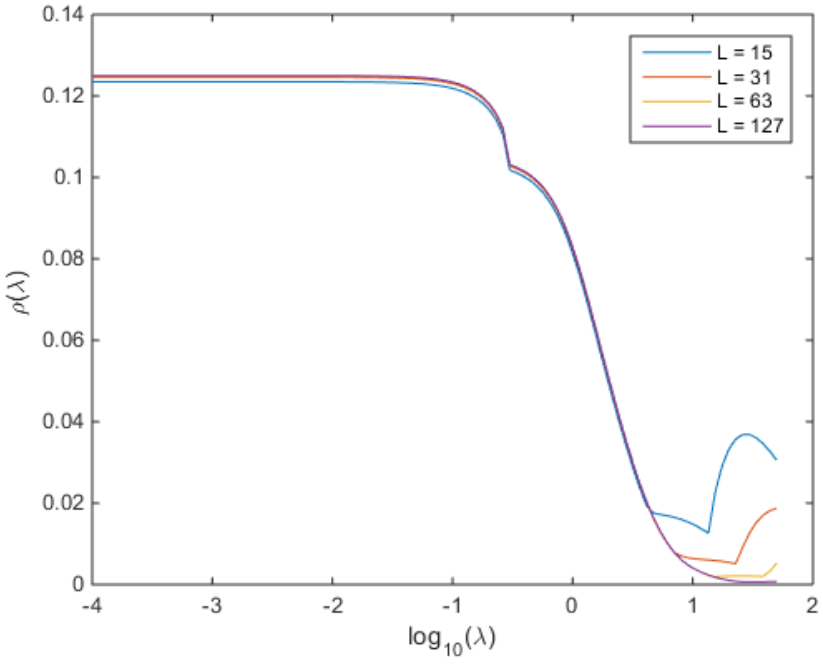

Figure 4.52: HGK - g = 0.5 - FPSA - WFD

L	N	FPSA-MPD ρ	FPSA-WFD ρ
1	2	8.5543×10^{-12}	8.5543×10^{-12}
15	16	0.1249	0.1234
31	32	0.1249	0.1246
63	64	0.1249	0.1248
127	128	0.1249	0.1249

Table 4.21: Spectral Radius - HGK - g = 0.5

We note that for the cross-section set, here, the higher cross-section moments reduce to sufficiently low magnitudes for them to have any significant effect on the spectral radii with increasing L. Therefore, we don't see the spectral radius increase with increasing L. Next we look at a much more Forward-Peaked scattering cross-section.

g = 0.9999

Now, we choose parameter $g = 0.9999$. The scattering cross-section moments for these parameters are given in Table 4.22.

Parameter	Value
S_N order	16, 32, 64
σ_a	0.00001
σ_t	1.00001 cm^{-1}
$\sigma_{s,0}$	1.0 cm^{-1}
$\sigma_{s,1}$	0.9999000000000000 cm^{-1}
$\sigma_{s,2}$	0.9998000100000000 cm^{-1}
$\sigma_{s,3}$	0.9997000299990000 cm^{-1}
$\sigma_{s,4}$	0.9996000599960001 cm^{-1}
$\sigma_{s,5}$	0.9995000999900005 cm^{-1}
$\sigma_{s,6}$	0.9994001499800015 cm^{-1}
$\sigma_{s,7}$	0.9993002099650035 cm^{-1}
$\sigma_{s,8}$	0.9992002799440070 cm^{-1}
$\sigma_{s,9}$	0.9991003599160126 cm^{-1}
$\sigma_{s,10}$	0.9990004498800210 cm^{-1}
$\sigma_{s,11}$	0.9989005498350330 cm^{-1}
$\sigma_{s,12}$	0.9988006597800495 cm^{-1}
$\sigma_{s,13}$	0.9987007797140715 cm^{-1}
$\sigma_{s,14}$	0.9986009096361001 cm^{-1}
$\sigma_{s,15}$	0.9985010495451365 cm^{-1}

Table 4.22: Problem Parameters - HGK - $g = 0.9999$

Keep $L(= 15)$ Constant, and Vary $N(= 16, 32, 64)$

First, we vary N while keeping L constant. The plots obtained from Fourier analyses are presented in Fig. 4.53, 4.54, 4.55, and 4.56. The information obtained from Fourier analyses is summarized in Table 4.23.

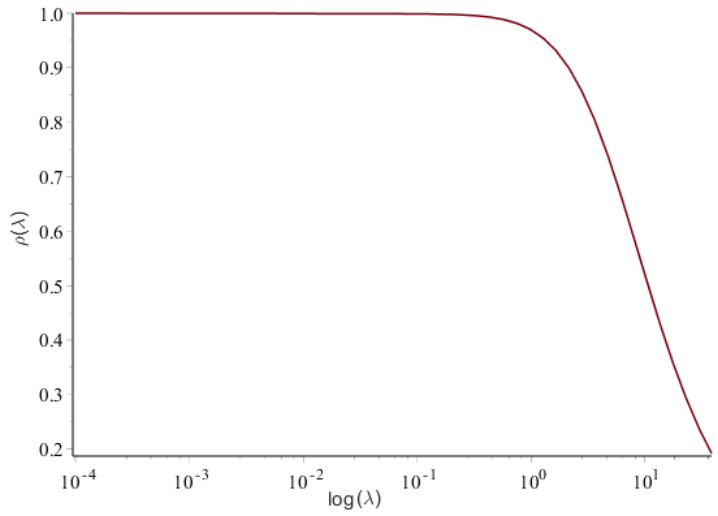

Figure 4.53: HGK - g = 0.9999 - Unaccelerated - $L = 15$

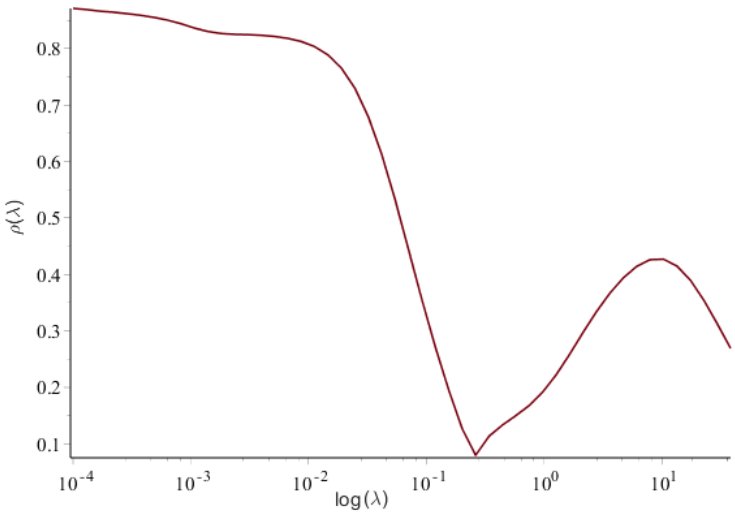

Figure 4.54: HGK - g = 0.9999 - FPSA - $L = 15$

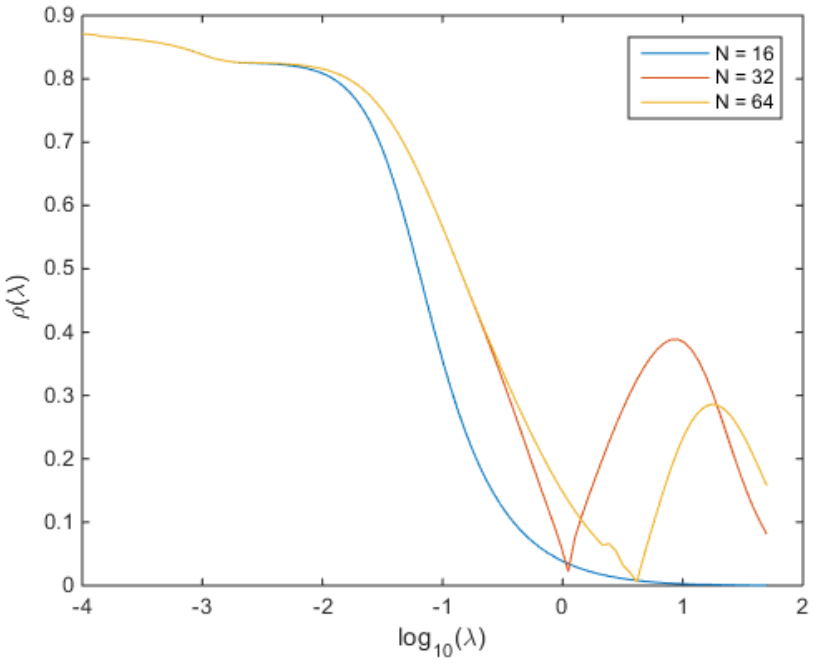

Figure 4.55: HGK - g = 0.9999 - FPSA - MPD - $L = 15$

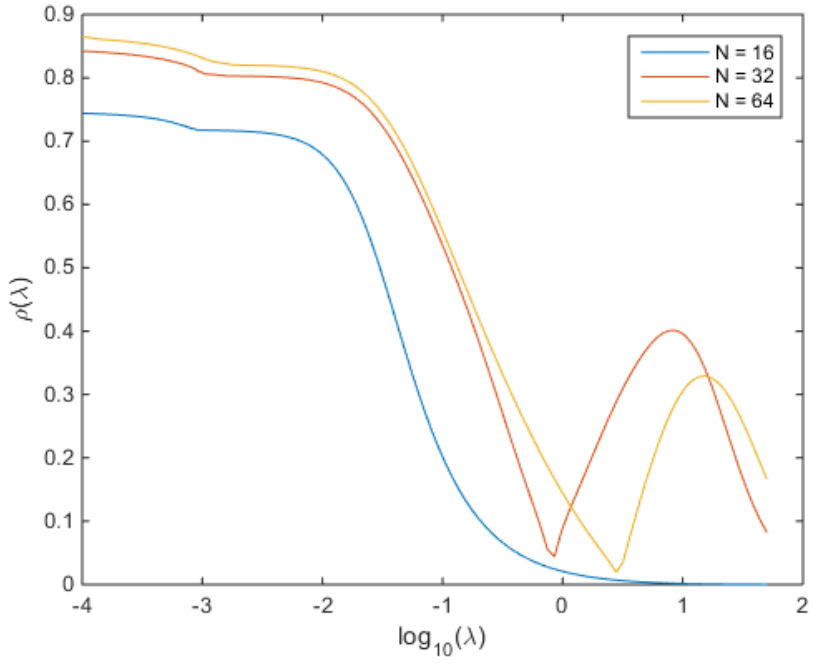

Figure 4.56: HGK - g = 0.9999 - FPSA - WFD - $L = 15$

N	Unaccelerated ρ	FPSA P_N-based ρ	FPSA-MPD ρ	FPSA-WFD ρ
∞	0.9999	0.8709		
16			0.8709	0.7466
32			0.8709	0.8469
64			0.8709	0.8669

Table 4.23: Spectral Radius - HGK - g = 0.9999 - $L = 15$

Vary N, and L s.t. $L = N - 1$

Now, we vary N and L together. $N = 2, 16, 32, 64, 128$ and $L = 1, 16, 31, 63, 127$. Eigenvalue plots obtained by Fourier analyses have been presented in Fig. 4.57 and 4.58. The spectral radius information is summarized in Table 4.24.

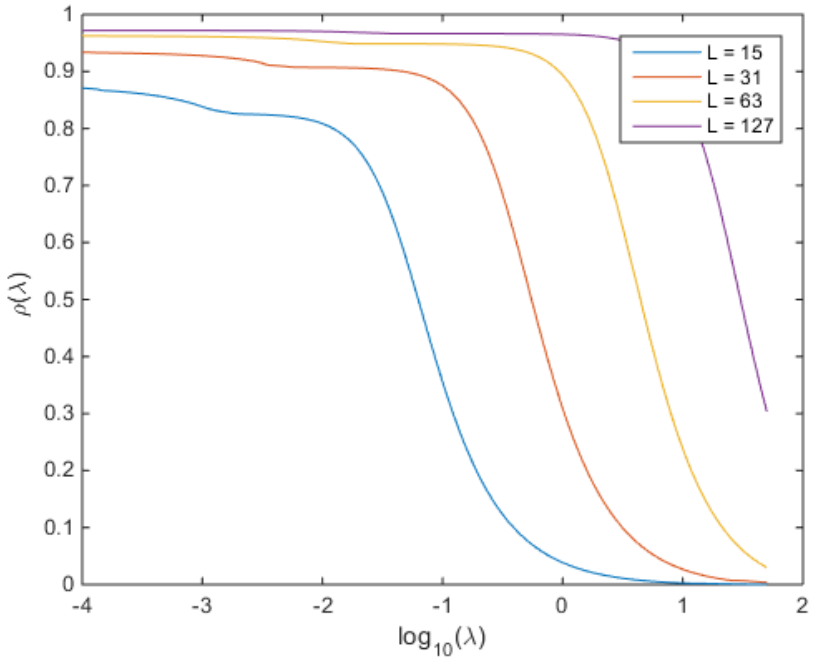

Figure 4.57: Spectral Radius - HGK - g = 0.9999 - FPSA - MPD

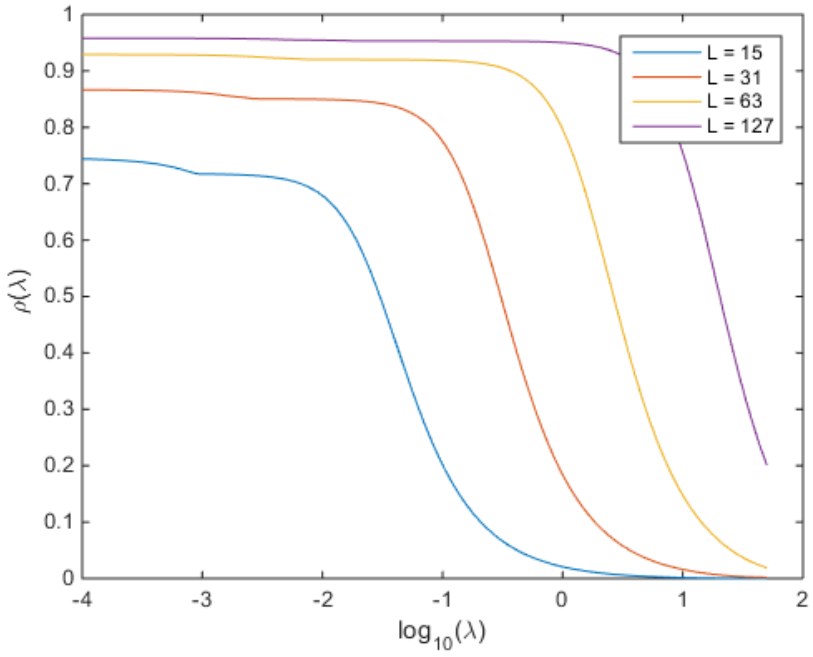

Figure 4.58: HGK - g = 0.9999 - FPSA - WFD

L	**N**	**FPSA-MPD ρ**	**FPSA-WFD ρ**
1	2	1.8692×10^{-12}	6.4026×10^{-12}
15	16	0.8709	0.7466
31	32	0.9338	0.8671
63	64	0.9624	0.9291
127	128	0.9719	0.9579

Table 4.24: Spectral Radius - HGK - g = 0.9999

Note the sudden increasse in spectral radius for this particular cross-section set. This is because Henyey-Greenstein kernel does not have a valid FP limit. This means, the FP approximation does not attenuate transport error moments effectively for source iteration.

To summarize this section, we saw how spectral radius evolves with increasing L, and N for various scattering kernels and corresponding parameters. We note that FP approximation can potentially

be used to precondition S_N equations with SRK and EK. For HGK, FP may not necessarily be an effective preconditioner in case of source iteration. For GMRES, however, this may or may not be the case. We will evaluate the performance of GMRES and FP-preconditioned GMRES solves for fully discretized (LD-S_N) transport equation in the next chapter.

4.5 Summary

In this chapter, we present all the relevant derivations for numerical implementation, testing, and assessment FPSA. We discretized the transport and FP equations in angle and space. We also presented an S_N-based framework for assessing FPSA. We presented spectral radius predictions for FPSA with SRK, EK, and HGK. We note that Fourier analysis predicts FPSA to perform well with SRK, and EK but not with HGK. This is attributed to the conditions under which the FP-limit is valid for different scattering cross-section kernels. In the next chapter, we will present numerical data obtained by analysis of FPSA with different scattering kernels and compare solution run-times of accelerated and unaccelerated solves.

Chapter 5

Numerical Experiments

In this chapter, we will talk about the numerical implementation of FPSA. We compare convergence rates and runtimes for unaccelerated and FPSA-accelerated transport solutions. We will use source iteration, and GMRES for solving the transport equation. We will do our study using three different scattering kernels - exponential kernel, screened Rutherford kernel, and Henyey-Greenstein kernel.

5.1 Solution Setup

In order to setup the problem up such that Krylov methods can be used, we write the matrix system in its operator form. We write spatially-discretized S_N equations in operator form by introducing mass matrix, M_m, which results from the linear-discontinuous finite element discretization from previous chapter, discrete-to-moment operator, D, to convert the angular flux vector into the moment vector, cross-section operator, Σ that holds relevant scattering cross-section moments in the correct order, and a moment-to-discrete operator, M, to the moment vector into the angular flux vector. We rewrite the operator S in Eq. (2.34) as $MM_m\Sigma D$. L will again represent the

streaming-plus-removal operator but this time it will be discretized in space and angle.

$$L\psi = MM_m\Sigma D\psi + q. \tag{5.1}$$

We write the transport equation in the standard linear system form, $A\underline{x} = \underline{b}$, where $\underline{x}$ is the solution vector, $\underline{\text{b}}$ is the source, and A is the global matrix representing the discretized system. We rearrange Eq. (5.1):

$$L\psi - MM_m\Sigma D\psi = q. \tag{5.2}$$

Now, we multiply Eq. (5.2) by DL^{-1} to obtain:

$$DL^{-1}L\psi - DL^{-1}MM_m\Sigma D\psi = DL^{-1}q, \tag{5.3}$$

which reduces to:

$$(I - DL^{-1}MM_m\Sigma)\phi = DL^{-1}q. \tag{5.4}$$

Eq. (5.4) is analogous to the standard linear system form of the transport equation, where:

$$A = (I - DL^{-1}MM_m\Sigma), \tag{5.5}$$

$$\underline{x} = \phi, \tag{5.6}$$

$$\underline{b} = DL^{-1}q. \tag{5.7}$$

We can apply any linear solver to Eq. (5.4) in order to obtain an estimate of ϕ. Obviously, some solvers may be more effective than others. Source iteration, as we showed in previous chapters, will be extremely slow to converge for problems with highly forward-peaked scattering kernel. Other,

more sophisticated Krylov methods, like GMRES, often, but not always converge more rapidly than source iteration. Geometric multigrid method (in space) is not expected to be useful because the transport equation we are solving is not elliptic, however, it may be useful if we use the second order even-parity (elliptic) form or Self-Adjoint-Angular-Flux form of the transport equation. Angular multigrid has been attempted and it has proven to be effective [24]. We have implemented transport solve using source iteration and GMRES. We have verified our implementations thoroughly but we do will not present verification data here for convenience.

In order to solve the Fokker-Planck error equation, we will use GMRES and direct inversion. The spatial discretization of the Fokker-Planck error equation is analogous to that of the transport equation. The standard linear system form of the Fokker-Planck error equation is also analogous to that of the transport equation.

5.1.1 Comparison of Measured and Theoretical Spectral Radii

Here, we will compare the measured [1] and theoretical (from discrete-in-angle Fourier analysis) spectral radii. We will do analysis for SRK, EK and HGK. We choose $L = 15$, $N = 16$. We use a slab of length, 100 cm, discretize it using 100 elements. We will use vacuum boundaries for numerical measurements of spectral radius. The spectral radii have been presented in Table 5.1.

Kernel/Parameter	$\rho^{\text{MPD}}_{\text{FPSA}}$**-FA**	$\rho^{\text{MPD}}_{\text{FPSA}}$**-Measured**	$\rho^{\text{WFD}}_{\text{FPSA}}$**-FA**	$\rho^{\text{WFD}}_{\text{FPSA}}$**-Measured**
SRK/$\eta = 2.85 \times 10^{-5}$	0.4706	0.4706	0.2121	0.2120
SRK/$\eta = 2.85 \times 10^{-6}$	0.3906	0.3898	0.3213	0.3215
EK/$\Delta = 10^{-4}$	0.2101	0.1975	0.6299	0.6301
EK/$\Delta = 10^{-5}$	0.1932	0.1954	0.6246	0.6327
HGK/$g = 0.9$	0.4304	0.4303	0.4177	0.4177
HGK/$g = 0.9999$	0.8709	0.8688	0.7439	0.7369

Table 5.1: Comparison of Numerical and Theoretical Spectral Radii

We obtain similar theoretical and measured spectral radii values for various scattering kernels with varying parameters. The numbers are not exactly the same because the numerical implementation does measurements on a finite slab with vacuum boundaries. As long as we get good-enough agreement between theoretical and numerical spectral radii, like we do here, we can say that our analysis is accurate.

5.2 Efficiency Study

In this section we will assess how the reduction in spectral radius (as seen in previous chapter) results in reduction in runtime of source iteration (SI) and GMRES solves. We run all problems using MATLAB [20] and track runtime using the tic-toc functionality in MATLAB. We will place tic and toc before and after the solver function calls respectively. This means we will not include the stiffness matrix generation time in our calculation. We will only account for the solver runtime.

Specifically, choose problems with $L = 15$, and $N = 16$, 32. We use beam and vacuum boundaries. We will have a unit distributed source for problems with vacuum boundaries and a unit beam source with the beam boundary. We will do this for SRK with $\eta = 2.83 \times 10^{-5}$, for EK with $\Delta = 10^{-5}$, and for HGK with $g = 0.9999$. We will solve the Fokker-Planck error equation (invert the preconditioner) using LU factorization via factorize object [6] in MATLAB, and GMRES [20, 33].

First, we compare unpreconditioned SI and GMRES solves. In order to compare these solves, we choose $\eta = 2.83 \times 10^{-5}$, $L = 15$, $N = 16$, $H = 1$cm, $K = 100$, $tol = 10^{-10}$. We do this to contrast source iteration and GMRES solves. Table 5.2 and 5.3 present this data. It is clear that GMRES is far superior to source iteration for forward-peaked transport problems.

BC/Source	Restart	GMRES	SI
Vacuum/Distributed			168160
	50	3305	
	100	2445	
	150	1875	
	200	1540	
Beam/Zero			did not converge
	50	2602	
	100	2200	
	150	1895	
	200	1735	

Table 5.2: SRK - Number of Iterations

BC/Source	Restart	GMRES	SI
Vacuum/Distributed			3197.49
	50	64.97	
	100	50.41	
	150	37.76	
	200	32.71	
Beam/Zero			did not converge
	50	50.68	
	100	43.99	
	150	41.29	
	200	36.11	

Table 5.3: SRK - Solver Runtime [s]

For problems with extremely forward-peaked scattering and with beam sources, there can be differences between measured and theoretical spectral radius values. The measured spectral radius values may be greater than unity even when the theoretical value aren't. This is due inadequate representation of delta function (scattering and/or source) in the numerical implementation. This precision issue can be remedied by using Galerkin quadrature [23], which integrates delta functions exactly. We have not implemented it here so we see that problems with beam sources diverge with SI.

Next, we will compare solution rutimes and iteration counts. We will compare these for unpre-

conditioned GMRES, FPSA-preconditioned SI, and FPSA-preconditioned GMRES solves. We will not include unpreconditioned source iteration in this study because its ineffectiveness with highly forward-peaked transport problems has already been demonstrated quite elaborately . We will arbitrarily choose our restart parameter for this study to be 150.

Screened Rutherford Kernel

We will compare efficiency data for SRK in this section. We will choose a slab of unit length discretized using hundred elements. We will choose $\eta = 2.83 \times 10^{-5}$ and $\sigma_a = 1$. Scattering cross-section moments are calculated using SRK. Finally, $L = 15$, and $N = 16$ and 32. Number of iterations and overall runtime data has been presented in Table 5.4, 5.5, 5.6, and 5.7.

FP-Solve	**L/N**	GMRES	$\text{FPSA}^{\text{MPD}}_{\text{GMRES}}$	$\text{FPSA}^{\text{WFD}}_{\text{GMRES}}$	$\text{FPSA}^{\text{MPD}}_{\text{SI}}$	$\text{FPSA}^{\text{WFD}}_{\text{SI}}$
GMRES	15/16	1487	9	6	14	10
	15/32	1499	9	7	14	12
Factorize	15/16		9	7	14	10
	15/32		9	8	14	12

Table 5.4: SRK - Vacuum Boundaries/Unit Distributed Source - Number of Iterations

FP-Solve	**L/N**	GMRES	$\text{FPSA}^{\text{MPD}}_{\text{GMRES}}$	$\text{FPSA}^{\text{WFD}}_{\text{GMRES}}$	$\text{FPSA}^{\text{MPD}}_{\text{SI}}$	$\text{FPSA}^{\text{WFD}}_{\text{SI}}$
GMRES	15/16	28.75	8.79	6.15	12.01	5.98
	15/32	28.12	36.76	18.36	54.13	19.77
Factorize	15/16		1.62	2.45	0.3373	0.2501
	15/32		2.75	4.73	0.4244	0.3392

Table 5.5: SRK - Vacuum Boundaries/Unit Distributed Source - Runtime [s]

FP-Solve	**L/N**	GMRES	$\text{FPSA}^{\text{MPD}}_{\text{GMRES}}$	$\text{FPSA}^{\text{WFD}}_{\text{GMRES}}$	$\text{FPSA}^{\text{MPD}}_{\text{SI}}$	$\text{FPSA}^{\text{WFD}}_{\text{SI}}$
GMRES	15/16	1357	12	8	21	13
	15/32	1335	13	10	23	19
Factorize	15/16		12	9	21	13
	15/32		13	11	23	19

Table 5.6: SRK - Beam Source - Number of Iterations

FP-Solve	**L/N**	GMRES	$\text{FPSA}^{\text{MPD}}_{\text{GMRES}}$	$\text{FPSA}^{\text{WFD}}_{\text{GMRES}}$	$\text{FPSA}^{\text{MPD}}_{\text{SI}}$	$\text{FPSA}^{\text{WFD}}_{\text{SI}}$
GMRES	15/16	26.54	11.39	6.975	9.69	5.403
	15/32	27	42.59	20.50	58.3	20.26
Factorize	15/16		1.687	2.547	0.4475	0.3074
	15/32		2.927	5.061	0.611	0.4828

Table 5.7: SRK - Beam Source - Runtime [s]

We observe a significant decrease (almost three orders of magnitude compared to unpreconditioned GMRES and five orders of magnitude compared to SI) in the number of transport-iterations required for convergence due to preconditioning. We also observe a decrease in overall solver runtimes due to preconditioning when FP-solve is done using LU factorization (by upto two orders of magnitude compared to unpreconditioned GMRES). The FP-solve, however, can be extremely expensive and render this preconditioner ineffective with respect to problem's overall runtime if iterative solution schemes are used without proper preconditioning. Here, the number of iterations required for one FP-solve using GMRES was of the same order as an unpreconditioned transport solve using GMRES. It is imperative that we find an effective preconditioner for FP-solves. We will look into this in future. The potential, however, of using FP as preconditioner for transport solves is amply evident from the data presented in this section. Next, we look at efficiency data for similar problems with the exponential kernel.

Exponential Kernel

We calculate scattering cross-section moments using EK for $\Delta = 10^{-5}$. The zeroth moment is calculated using SRK like we did in the previous section. The study, here, is done exactly like we did in the case of SRK. The same parameters are used as we used for SRK except for scattering cross-section moments. Number of iterations and overall runtime data has been presented in Table 5.8, 5.9, 5.10, and 5.11.

FP-Solve	**L/N**	GMRES	$\text{FPSA}^{\text{MPD}}_{\text{GMRES}}$	$\text{FPSA}^{\text{WFD}}_{\text{GMRES}}$	$\text{FPSA}^{\text{MPD}}_{\text{SI}}$	$\text{FPSA}^{\text{WFD}}_{\text{SI}}$
GMRES	15/16	2217	7	8	9	15
	15/32	2256	10	9	17	19
Factorize	15/16		7	9	9	15
	15/32		10	10	17	19

Table 5.8: EK - Vacuum Boundaries/Unit Distributed Source - Number of Iterations

FP-Solve	**L/N**	GMRES	$\text{FPSA}^{\text{MPD}}_{\text{GMRES}}$	$\text{FPSA}^{\text{WFD}}_{\text{GMRES}}$	$\text{FPSA}^{\text{MPD}}_{\text{SI}}$	$\text{FPSA}^{\text{WFD}}_{\text{SI}}$
GMRES	15/16	51.73	10.32	13.34	11.91	18.49
	15/32	56.10	31.14	25.06	42.82	27.85
Factorize	15/16		2.3754	4.5586	0.3762	0.454
	15/32		4.155	8.463	0.6098	0.6424

Table 5.9: EK - Vacuum Boundaries/Unit Distributed Source - Runtime [s]

FP-Solve	**L/N**	GMRES	$\text{FPSA}^{\text{MPD}}_{\text{GMRES}}$	$\text{FPSA}^{\text{WFD}}_{\text{GMRES}}$	$\text{FPSA}^{\text{MPD}}_{\text{SI}}$	$\text{FPSA}^{\text{WFD}}_{\text{SI}}$
GMRES	15/16	2086	9	10	12	35
	15/32	1932	14	12	24	28
Factorize	15/16		14	13	12	35
	15/32		14	13	24	28

Table 5.10: EK - Beam Source - Number of Iterations

FP-Solve	**L/N**	GMRES	$\text{FPSA}^{\text{MPD}}_{\text{GMRES}}$	$\text{FPSA}^{\text{WFD}}_{\text{GMRES}}$	$\text{FPSA}^{\text{MPD}}_{\text{SI}}$	$\text{FPSA}^{\text{WFD}}_{\text{SI}}$
GMRES	15/16	39.55	9.45	11.63	8.335	19.42
	15/32	36.14	24.89	18.57	34.74	24.87
Factorize	15/16		2.842	6.657	0.2929	0.6853
	15/32		2.898	6.799	0.6329	0.6585

Table 5.11: EK - Beam Source - Runtime [s]

We see similar behavior to what we saw in the case of SRK. The solver runtimes differ due to difference in rate at which FP-solve converges for this particular problem. Again, we note a significant decrease in number of iterations but a decrease in solver runtime strongly depends on the efficiency of the FP-solve. Next we will look at the Henyey-Greenstein kernel.

Henyey-Greenstein Kernel

In this section, we let the asymmetry parameter, $g = 0.9999$. The study is carried out in the same way as the previously for SRK and EK. For this section, we will choose $\sigma_a = 0.00001\ cm^{-1}$. The scattering cross-section moments are calculated using HGK. We will choose slab length of 50 cm disretized using 200 elements. Number of iterations and overall runtime data has been presented in Table 5.12, 5.13, 5.14, and 5.15.

FP-Solve	**L/N**	GMRES	$\text{FPSA}_{\text{GMRES}}^{\text{MPD}}$	$\text{FPSA}_{\text{GMRES}}^{\text{WFD}}$	$\text{FPSA}_{\text{SI}}^{\text{MPD}}$	$\text{FPSA}_{\text{SI}}^{\text{WFD}}$
GMRES	15/16	1150	10	7	28	18
	15/32	1461	14	12	32	31
Factorize	15/16		10	8	28	18
	15/32		14	13	32	31

Table 5.12: HGK - Vacuum Boundaries/Unit Distributed Source - Number of Iterations

Invert FP	**L/N**	GMRES	$\text{FPSA}_{\text{GMRES}}^{\text{MPD}}$	$\text{FPSA}_{\text{GMRES}}^{\text{WFD}}$	$\text{FPSA}_{\text{SI}}^{\text{MPD}}$	$\text{FPSA}_{\text{SI}}^{\text{WFD}}$
GMRES	15/16	83.66	288.1	160.9	931.9	373.4
	15/32	102.5	1055	572.7	2618	1428
Factorize	15/16		6.390	12.27	2.193	1.385
	15/32		11.75	28.820	2.651	2.5778

Table 5.13: HGK - Vacuum Boundaries/Unit Distributed Source - Runtime [s]

Invert FP	**L/N**	GMRES	$\text{FPSA}_{\text{GMRES}}^{\text{MPD}}$	$\text{FPSA}_{\text{GMRES}}^{\text{WFD}}$	$\text{FPSA}_{\text{SI}}^{\text{MPD}}$	$\text{FPSA}_{\text{SI}}^{\text{WFD}}$
GMRES	15/16	597	16	12	29	17
	15/32	1634	21	19	32	31
Factorize	15/16		12	9	29	17
	15/32		17	16	32	31

Table 5.14: HGK - Beam Source - Number of Iterations

FP-Solve	**L/N**	GMRES	$\text{FPSA}^{\text{MPD}}_{\text{GMRES}}$	$\text{FPSA}^{\text{WFD}}_{\text{GMRES}}$	$\text{FPSA}^{\text{MPD}}_{\text{SI}}$	$\text{FPSA}^{\text{WFD}}_{\text{SI}}$
GMRES	15/16	42.29	479.9	331.2	1040	285.7
	15/32	115.1	1804	990.6	2408	1315
Factorize	15/16		6.795	12.41	2.131	1.316
	15/32		12.59	29.69	2.945	2.452

Table 5.15: HGK - Beam Source - Runtime [s]

We note that, just like for SRK and EK, preconditioned schemes have significantly less iteration counts. However depending on how the Fokker-Planck error equation is solved, the preconditioning may or may not be effective with respect to runtime reduction. Solving the FP equation with GMRES renders FPSA scheme unviable, however use of factorization reduces to overall runtime significantly.

5.3 Summary

In this chapter we described how to numerically solve the transport equation. We ran several numerical experiments and assessed the speed-ups in iteration count and solver runtime. We saw that preconditioning transport solve using FP resulted in reduction in iteration count by upto three orders (when compared to unpreconditioned GMRES solves). The overall runtime, however, depended completely on how efficiently the FP preconditioner was solved. Direct factorization resulted in a runtime reduction by upto two orders of magnitude. We noted that FP can be a very effective preconditioner for transport solves with highly forward-peaked scattering. However, we must develop an effective solver for FP-solve itself in order to make this an attractive preconditioning method.

Chapter 6

Conclusion and Future Work

We began this dissertation with a basic literature review and introducing the problem at hand. We then went on to provide background required for development of the method presented in this thesis - we went over the transport equation, derived its basic mono-energetic, slab-geometry form. We then described basic source iteration and presented how it can be arbitrarily slow using Fourier analysis. Further, we introduced the idea of synthetic acceleration and demonstrated its equivalence with preconditioning. The first two chapters thoroughly introduced the problem at hand and basic background required to solve it.

In the third chapter, we introduced FPSA. First, we derived the limit of error equation as average scattering angle approached zero. This returned the Fokker-Planck approximation. This led us to the idea of using the Fokker-Planck approximation as a preconditioner (it has already been used widely as an approximation to the transport equation; now we want to accelerate transport using Fokker-Planck). Further we went on to describe where the Fokker-Planck approximation is a valid limit of the transport equation. We introduced the idea of FPSA in this chapter. We presented a P_N based Fourier analysis framework in order to assess FPSA. We also presented how FPSA was

equivalent to P_L acceleration. Under the specific constraint presented in Sec. 3.3, where FPSA became equivalent to P_L acceleration, we expect convergence of transport in one iteration.

In the fourth chapter, we described spatial (LD) and angular (S_N) discretization for the transport equation and the Fokker-Planck equation. We went over WFD and MPD discretizations for the angular Laplacian term in the FP equation. Towards the end of this chapter, we presented an S_N based framework for analysis of FPSA with WFD and MPD and all the convergence rate predictions for SRK, EK, and HGK under with varying parameters - L, N, η, Δ, and g. The fifth chapter constituted the fully numerical part of this dissertation. We also presented a speed-up study towards the end of the chapter for screened Rutherford kernel, exponential kernel, and the Henyey-Greenstein kernel. Essentially, in Ch. 4, and 5, we presented an in-depth study on the viability of using FP as preconditioner for transport problems with highly forward-peaked scattering. In this chapter, we will present our conclusions.

6.1 Conclusion

Information presented in the previous five chapters leads us to believe that a forward-peaked scattering kernel presents significant difficulties in obtaining an efficient solution. Standard techniques including SI and unpreconditioned GMRES can be slow to converge and even diverge. Fokker-Planck approximation is an effective preconditioning tool to accelerate such problems. However, it is imperative that we develop an effective preconditioner to make Fokker-Planck solves efficient.

6.2 Future Work

In future, we would like to develop effective preconditioning techniques for Fokker-Planck solves. We were unable to include that in this dissertation. We have been looking, specifically, at nonlinear techniques for Fokker-Planck solve but nothing conclusively effective has been observed yet. Therefore this was not included in this dissertation. It would be an extremely interesting problem to solve.

Other than that, we note the high spectral radius for FPSA with SI. We note that for kernels with no Fokker-Planck limit, we must incorporate higher order FP operators in our approximation of the error equation. We want to use Generalized Fokker-Planck equation to approximate the error equation. We expect extremely good convergence rates at least with GMRES. The problem, here also would be the solve time of GFP equation since this time we solve a coupled set of equations [17]. If we go this route, we would definitely need an efficient solution technique for the GFP solve.

Other than that we wish to extend and analyze the FPSA technique to multi-D, energy-dependent problems. We would also like to develop a moment-preserving discretization for the angular Laplacian term of the Fokker-Planck equation in multi-D settings.

Appendices

Appendix A

Screened Rutherford Scattering Cross-section Moments

$C = 0.7805$; $\eta = 2.836 \times 10^{-4}$; $L = 127$; $l = 0, 1, ...L$

$\sigma_{s,l} =$ [1375.667689, 1370.072664, 1361.213931, 1349.856033, 1336.498659, 1321.507580, 1305.167316, 1287.707638, 1269.318837, 1250.161346, 1230.372215, 1210.069693, 1189.356585, 1168.322808, 1147.047368, 1125.599937, 1104.042120, 1082.428503, 1060.807519, 1039.222176, 1017.710679, 996.3069614, 975.0411392, 953.9399137, 933.0269180, 912.3230238, 891.8466119, 871.6138124, 851.6387190, 831.9335802, 812.5089707, 793.3739463, 774.5361826, 756.0021013, 737.7769840, 719.8650759, 702.2696799, 684.9932423, 668.0374310, 651.4032071, 635.0908903, 619.1002182, 603.4304017, 588.0801750, 573.0478416, 558.3313168, 543.9281667, 529.8356436, 516.0507192, 502.5701149, 489.3903292, 476.5076638, 463.9182469, 451.6180551, 439.6029328, 427.8686112, 416.4107251, 405.2248278, 394.3064060, 383.6508928, 373.2536796, 363.1101269, 353.2155749, 343.5653525, 334.1547857, 324.9792054, 316.0339545, 307.3143944, 298.8159108, 290.5339186, 282.4638676, 274.6012458, 266.9415843, 259.4804601, 252.2134994, 245.1363807, 238.2448371, 231.5346582, 225.0016926, 218.6418492, 212.4510984, 206.4254742, 200.5610740, 194.8540605, 189.3006619, 183.8971723, 178.6399522, 173.5254291, 168.5500970, 163.7105166, 159.0033154, 154.4251873, 149.9728927, 145.6432574, 141.4331729, 137.3395954, 133.3595457, 129.4901081, 125.7284302, 122.0717219, 118.5172546, 115.0623609, 111.7044333, 108.4409232, 105.2693415, 102.1872553, 99.1922891, 96.2821230, 93.4544919, 90.7071847, 88.0380431, 85.4449608, 82.9258828, 80.4788041, 78.1017690, 75.7928699, 73.5502467, 71.3720855, 69.2566182,

67.2021207, 65.2069129, 63.2693575, 61.3878584, 59.5608610, 57.7868503, 56.0643510, 54.3919255, 52.7681737].

$C = 0.7805;\ \eta = 2.836 \times 10^{-5};\ L = 127;\ l = 0, 1, ...L$

$\sigma_{s,l}$ = [13760.18804, 13752.79625, 13740.35284, 13723.63610, 13703.16340, 13679.32132, 13652.41778, 13622.70811, 13590.40995, 13555.71257, 13518.78311, 13479.77096, 13438.81090, 13396.02553, 13351.52706, 13305.41882, 13257.79638, 13208.74850, 13158.35792, 13106.70201, 13053.85332, 12999.88004, 12944.84643, 12888.81313, 12831.83748, 12773.97383, 12715.27368, 12655.78600, 12595.55733, 12534.63200, 12473.05223, 12410.85833, 12348.08877, 12284.78032, 12220.96812, 12156.68584, 12091.96567, 12026.83848, 11961.33386, 11895.48018, 11829.30467, 11762.83347, 11696.09166, 11629.10336, 11561.89174, 11494.47907, 11426.88676, 11359.13541, 11291.24482, 11223.23408, 11155.12151, 11086.92478, 11018.66090, 10950.34622, 10881.99651, 10813.62695, 10745.25216, 10676.88621, 10608.54268, 10540.23461, 10471.97460, 10403.77475, 10335.64676, 10267.60186, 10199.65088, 10131.80426, 10064.07204, 9996.463883, 9928.989115, 9861.656697, 9794.475260, 9727.453109, 9660.598238, 9593.918336, 9527.420799, 9461.112740, 9395.000997, 9329.092143, 9263.392494, 9197.908118, 9132.644840, 9067.608253, 9002.803724, 8938.236402, 8873.911222, 8809.832914, 8746.006010, 8682.434848, 8619.123579, 8556.076173, 8493.296423, 8430.787952, 8368.554218, 8306.598519, 8244.923997, 8183.533641, 8122.430298, 8061.616669, 8001.095318, 7940.868679, 7880.939051, 7821.308610, 7761.979411, 7702.953388, 7644.232362, 7585.818041, 7527.712026, 7469.915813, 7412.430796, 7355.258269, 7298.399431, 7241.855389, 7185.627157, 7129.715664, 7074.121753, 7018.846184, 6963.889638, 6909.252717, 6854.935949, 6800.939788, 6747.264618, 6693.910754, 6640.878444, 6588.167872, 6535.779158, 6483.712364, 6431.967489, 6380.544478].

$C = 0.7805;\ \eta = 2.836 \times 10^{-6};\ L = 127;\ l = 0, 1, ...L$

$\sigma_{s,l}$ = [1.376053925$\times 10^5$, 1.375962036$\times 10^5$, 1.375801671$\times 10^5$, 1.375580632$\times 10^5$, 1.375304120$\times 10^5$, 1.374976030$\times 10^5$, 1.374599480$\times 10^5$, 1.374177065$\times 10^5$, 1.373711006$\times 10^5$, 1.373203248$\times 10^5$, 1.372655515$\times 10^5$,

1.372069359×10^5, 1.371446189×10^5, 1.370787293×10^5, 1.370093861×10^5, 1.369366996×10^5, 1.368607725×10^5, 1.367817010×10^5, 1.366995756×10^5, 1.366144814×10^5, 1.365264992×10^5, 1.364357053×10^5, 1.363421724×10^5, 1.362459699×10^5, 1.361471638×10^5, 1.360458174×10^5, 1.359419914×10^5, 1.358357438×10^5, 1.357271306×10^5, 1.356162055×10^5, 1.355030204×10^5, 1.353876252×10^5, 1.352700682×10^5, 1.351503960×10^5, 1.350286538×10^5, 1.349048852×10^5, 1.347791325×10^5, 1.346514370×10^5, 1.345218383×10^5, 1.343903752×10^5, 1.342570853×10^5, 1.341220052×10^5, 1.339851706×10^5, 1.338466160×10^5, 1.337063752×10^5, 1.335644811×10^5, 1.334209658×10^5, 1.332758606×10^5, 1.331291960×10^5, 1.329810018×10^5, 1.328313072×10^5, 1.326801406×10^5, 1.325275298×10^5, 1.323735021×10^5, 1.322180840×10^5, 1.320613015×10^5, 1.319031802×10^5, 1.317437450×10^5, 1.315830202×10^5, 1.314210299×10^5, 1.312577975×10^5, 1.310933459×10^5, 1.309276977×10^5, 1.307608750×10^5, 1.305928994×10^5, 1.304237923×10^5, 1.302535743×10^5, 1.300822662×10^5, 1.299098878×10^5, 1.297364590×10^5, 1.295619991×10^5, 1.293865272×10^5, 1.292100620×10^5, 1.290326218×10^5, 1.288542247×10^5, 1.286748884×10^5, 1.284946304×10^5, 1.283134678×10^5, 1.281314174×10^5, 1.279484960×10^5, 1.277647197×10^5, 1.275801046×10^5, 1.273946665×10^5, 1.272084210×10^5, 1.270213833×10^5, 1.268335684×10^5, 1.266449912×10^5, 1.264556663×10^5, 1.262656080×10^5, 1.260748305×10^5, 1.258833476×10^5, 1.256911730×10^5, 1.254983204×10^5, 1.253048029×10^5, 1.251106336×10^5, 1.249158256×10^5, 1.247203914×10^5, 1.245243437×10^5, 1.243276947×10^5, 1.241304567×10^5, 1.239326416×10^5, 1.237342613×10^5, 1.235353274×10^5, 1.233358514×10^5, 1.231358447×10^5, 1.229353185×10^5, 1.227342836×10^5, 1.225327511×10^5, 1.223307316×10^5, 1.221282357×10^5, 1.219252738×10^5, 1.217218562×10^5, 1.215179931×10^5, 1.213136944×10^5, 1.211089700×10^5, 1.209038297×10^5, 1.206982830×10^5, 1.204923395×10^5, 1.202860085×10^5, 1.200792993×10^5, 1.198722209×10^5, 1.196647823×10^5, 1.194569925×10^5, 1.192488601×10^5, 1.190403938×10^5, 1.188316023×10^5, 1.186224938×10^5, 1.184130767×10^5].

Appendix B

Exponential Kernel Scattering Cross-section Moments

$\Delta = 10^{-6}$; $L = 127$; $l = 0, 1, ...L$

$\sigma_{s,l} =$ [13761.95103687960, 13761.93727492856, 13761.90975106778, 13761.85470331868, 13761.81341774080,

13761.75837066604, 13761.67579974425, 13761.60699136524, 13761.52442217744, 13761.41432921141,

13761.31799935237, 13761.20790964787, 13761.07029626143, 13760.94644673881, 13760.80883860928,

13760.64370692158, 13760.49234004714, 13760.32721607954, 13760.13456870500, 13759.95568728571,

13759.76305056222, 13759.54289061045, 13759.33649794843, 13759.11635204636, 13758.86868312205,

13758.63478301448, 13758.38713200615, 13758.11195820898, 13757.85055494796, 13757.57540340062,

13757.27272932513, 13756.98382769755, 13756.68118067321, 13756.35101140867, 13756.03461669608,

13755.70447975140, 13755.34682088165, 13755.00293886010, 13754.64531804619, 13754.26017564948,

13753.88881258934, 13753.50371445161, 13753.09109510041, 13752.69225776618, 13752.27968934415,

13751.83960010495, 13751.41329575507, 13750.97326458214, 13750.50571301526, 13750.05194940188,

13749.58446350513, 13749.08945766447, 13748.60824303321, 13748.11331093316, 13747.59085936598,

13747.08220245570, 13746.55983316605, 13746.00994491270, 13745.47385495522, 13744.92405798261,

13744.34674257625, 13743.78322929609, 13743.20601463979, 13742.60128210613, 13742.01035572020,

13741.40573387183, 13740.77359472882, 13740.15526594613, 13739.52324788935, 13738.86371314685,

13738.21799316818, 13737.55859037837, 13736.87167153784, 13736.19857205539, 13735.51179649931,

13734.79750555346, 13734.09703875053, 13733.38290288595, 13732.64125231838, 13731.91343086897,

13731.17194764433, 13730.40295042915, 13729.64778749761, 13728.87897035161, 13728.08263995306,

13727.30014919368, 13726.50401205490, 13725.68036242695, 13724.87055798355, 13724.04711527003,

13723.19616085595, 13722.35905736146, 13721.50832398027, 13720.63007971222, 13719.76569228823,

13718.88768363504, 13717.98216493361, 13717.09050918992, 13716.18524114855, 13715.25246392228,

13714.33355595645, 13713.40104489837, 13712.44102554331, 13711.49488194016, 13710.53514472403,

13709.54790012322, 13708.57453795433, 13707.58759192550, 13706.57313944848, 13705.57257627170,

13704.55843926168, 13703.51679676397, 13702.48905062287, 13701.44774094881, 13700.37892677138,

13699.32401619471, 13698.25555265887, 13697.15958562757, 13696.07752962873, 13694.98193151791,

13693.85883094293, 13692.74964901937, 13691.62693610433, 13690.47672177962, 13689.34043391228,

13688.19062644716, 13687.01331864984, 13685.84994530254]

$\Delta = 10^{-9}$; $L = 127$; $l = 0, 1, ...L$

$\sigma_{s,l} =$ [13761.95103687960, 13761.95102311765, 13761.95099559375, 13761.95094054594, 13761.95089926009,

13761.95084421229, 13761.95076164058, 13761.95069283083, 13761.95061025913, 13761.95050016352,

13761.95040382987, 13761.95029373427, 13761.95015611476, 13761.95003225721, 13761.94989463772,

13761.94972949431, 13761.94957811286, 13761.94941296948, 13761.94922030218, 13761.94904139683,

13761.94884872956, 13761.94862853837, 13761.94842210913, 13761.94820191797, 13761.94795420290,

13761.94772024977, 13761.94747253473, 13761.94719729578, 13761.94693581876, 13761.94666057985,

13761.94635781702, 13761.94606881612, 13761.94576605334, 13761.94543576663, 13761.94511924186,

13761.94478895521, 13761.94443114464, 13761.94408709600, 13761.94372928549, 13761.94334395106,

13761.94297237856, 13761.94258704419, 13761.94217418591, 13761.94177508955, 13761.94136223134,

13761.94092184921, 13761.94049522900, 13761.94005484695, 13761.93958694098, 13761.93913279693,

13761.93866489105, 13761.93816946125, 13761.93768779337, 13761.93719236367, 13761.93666941004, 13761.93616021834, 13761.93563726483, 13761.93508678738, 13761.93455007187, 13761.93399959455, 13761.93342159330, 13761.93285735399, 13761.93227935287, 13761.93167382783, 13761.93108206473, 13761.93047653982, 13761.92984349100, 13761.92922420412, 13761.92859115543, 13761.92793058284, 13761.92728377219, 13761.92662319974, 13761.92593510338, 13761.92526076898, 13761.92457267278, 13761.92385705267, 13761.92315519452, 13761.92243957458, 13761.92169643073, 13761.92096704885, 13761.92022390519, 13761.91945323761, 13761.91869633201, 13761.91792566464, 13761.91712747335, 13761.91634304404, 13761.91554485298, 13761.91471913799, 13761.91390718499, 13761.91308147025, 13761.91222823157, 13761.91138875490, 13761.91053551649, 13761.90965475414, 13761.90878775381, 13761.90790699175, 13761.90699870574, 13761.90610418177, 13761.90519589607, 13761.90426008643, 13761.90333803883, 13761.90240222951, 13761.90143889625, 13761.90048932503, 13761.89952599211, 13761.89853513525, 13761.89755804043, 13761.89656718392, 13761.89554880348, 13761.89454418508, 13761.89352580500, 13761.89247990100, 13761.89144775904, 13761.89040185541, 13761.88932842786, 13761.88826876236, 13761.88719533520, 13761.88609438412, 13761.88500719509, 13761.88390624442, 13761.88277776983, 13761.88166305730, 13761.88053458314, 13761.87937858506, 13761.87823634905, 13761.87708035142, 13761.87589682987, 13761.87472707039]

Appendix C

Henyey-Greenstein Scattering Cross-section Moments

g = 0.5; $L = 63; l = 1, 2, ...L$

$\sigma_{s,l}$ = [1., .5000000000000000, .2500000000000000, .1250000000000000, 0.6250000000000000e-1, 0.3125000000000000e-1, 0.1562500000000000e-1, 0.7812500000000000e-2, 0.3906250000000000e-2, 0.1953125000000000e-2, 0.9765625000000000e-3, 0.4882812500000000e-3, 0.2441406250000000e-3, 0.1220703125000000e-3, 0.6103515625000000e-4, 0.3051757812500000e-4, 0.1525878906250000e-4, 0.7629394531250000e-5, 0.3814697265625000e-5, 0.1907348632812500e-5, 9.536743164062500e(-7), 4.768371582031250e(-7), 2.384185791015625e(-7), 1.192092895507812e(-7), 5.960464477539062e(-8), 2.980232238769531e(-8), 1.490116119384766e(-8), 7.450580596923828e(-9), 3.725290298461914e(-9), 1.862645149230957e(-9), 9.313225746154785e(-10), 4.656612873077393e(-10), 2.328306436538696e(-10), 1.164153218269348e(-10), 5.820766091346741e(-11), 2.910383045673370e(-11), 1.455191522836685e(-11), 7.275957614183426e(-12), 3.637978807091713e(-12), 1.818989403545856e(-12), 9.094947017729282e(-13), 4.547473508864641e(-13), 2.273736754432321e(-13), 1.136868377216160e(-13), 5.684341886080801e(-14), 2.842170943040401e(-14), 1.421085471520200e(-14), 7.105427357601002e(-15), 3.552713678800501e(-15), 1.776356839400250e(-15), 8.881784197001252e(-16), 4.440892098500626e(-16), 2.220446049250313e(-16), 1.110223024625157e(-16), 5.551115123125783e(-17), 2.775557561562891e(-17), 1.387778780781446e(-17), 6.938893903907228e(-18), 3.469446951953614e(-18), 1.734723475976807e(-18), 8.673617379884035e(-

19), 4.336808689942018e(-19), 2.168404344971009e(-19), 1.084202172485504e(-19)]

g $= 0.9999;\ L = 63; l = 1, 2, ...L$

$\sigma_{s,l} =$ [1., .9999000000000000, .9998000100000000, .9997000299990000, .9996000599960001, .9995000999900005,

.9994001499800015, .9993002099650035, .9992002799440070, .9991003599160126, .9990004498800210,

.9989005498350330, .9988006597800495, .9987007797140715, .9986009096361001, .9985010495451365,

.9984011994401820, .9983013593202379, .9982015291843059, .9981017090313875, .9980018988604843,

.9979020986705983, .9978023084607312, .9977025282298852, .9976027579770622, .9975029977012645,

.9974032474014943, .9973035070767542, .9972037767260465, .9971040563483739, .9970043459427391,

.9969046455081448, .9968049550435940, .9967052745480896, .9966056040206348, .9965059434602328,

.9964062928658867, .9963066522366001, .9962070215713765, .9961074008692193, .9960077901291324,

.9959081893501195, .9958085985311845, .9957090176713314, .9956094467695642, .9955098858248873,

.9954103348363048, .9953107938028212, .9952112627234409, .9951117415971685, .9950122304230088,

.9949127291999665, .9948132379270465, .9947137566032538, .9946142852275935, .9945148237990707,

.9944153723166908, .9943159307794592, .9942164991863812, .9941170775364626, .9940176658287089,

.9939182640621261, .9938188722357199, .9937194903484963]

Bibliography

[1] M. L. Adams and E. W. Larsen. Fast iterative methods for discrete-ordinates particle transport calculations. *Progress in Nuclear Energy*, 2002.

[2] R. E. Alcouffe. Diffusion synthetic acceleration for the diamond-differenced discrete-ordinates equations. *Nuclear Science and Engineering*, 1977.

[3] C. M. Bender and S. A. Orszag. *Mathematical Methods for Scientists and Engineers Asymptotic Methods and Perturbation Theory.* McGraw-Hill.

[4] E. Larsen C. Bogers. On accuracy of fokker-planck and fermi pencil beam for charged particle transport. *Medical Physics*, 1996.

[5] K. S. Smith D. A. Knoll and H. K. Park. Appplication of jacobian-free newton-krylov method to nonlinear diffusion acceleration of transport source iteration in slab geometry. *Nuclear Science and Engineering*, 2011.

[6] T. A. Davis. Factorize: an object-oriented linear system solver for matlab. *ACM Transactions on Mathematical Software*, 2009.

[7] D. A. Dixon. *A Computationally Efficient Moment-Preserving Monte Carlo Electron Transport Method with Implementation in GEANT4.* PhD thesis, University of New Mexico, 2015.

[8] A. K. Prinja G. C. Pomraning and J. W. VanDenburg. An asymptotic model for spreading of a collimated beam. *Nuclear Science and Engineering*, 1992.

[9] W. Gautschi. *Numerical Analysis*. Birkhauser, 2012.

[10] L. A. Hageman and D. M. Young. *Applied Iterative Methods*. Academic Press, 1981.

[11] Kenneth Smith J. E. Morel, T. A. Wareing. Linear discontinuous spatial differencing scheme for S_N radiative transfer calculations. *Journal of Computational Physics*, 1996.

[12] T. A. Wareing J. S. Warsa and J. E. Morel. Krylov iterative methods and the degraded effectiveness of diffusion synthetic acceleration for multidimensional sn calculations in problems with material discontinuities. *Nuclear Science and Engineering*, 2004.

[13] K. M. Khattab and E. W. Larsen. Synthetic acceleration methods for linear transport problems with highly anisotropic scattering. *Nuclear Science and Engineering*, 1991.

[14] H. J. Kopp. Synthetic acceleration method solution of the transport equation. *Nuclear Science and Engineering*, 1963.

[15] M. Landesman and J. E. Morel. Angular fokker-planck decomposition and representation techniques. *Nuclear Science and Engineering*, 1989.

[16] E. W. Larsen. The linear boltzmann equation in optically thick systems with forward-peaked scattering. *Progress in Nuclear Energy*, 1999.

[17] C. L. Leakeas and E. W. Larsen. A generalized fokker planck model model for transport of collimated beams. *Nuclear Science and Engineering*, 2001.

[18] V. I. Lebedev. The iterative kp method for the kinetic equation. *Mathematical Methods for Solving Nuclear Physics Problems*, 1964.

[19] E. E. Lewis and W. F. Miller. *Computational Methods of Neutron Transport*. Americal Nuclear Society, 1993.

[20] MATLAB. *Version 9.1 (R2016b)*. The MathWorks Inc., 2016.

[21] J. E. Morel. Fokker planck calculations using standard discrete ordinates codes. *Nuclear Science and Engineering*, 1981.

[22] J. E. Morel. An improved fokker-planck angular discretization scheme. *Nuclear Science and Engineering*, 1985.

[23] J. E. Morel. A hybrid collocation-galerkin-sn method for solving the boltzmann transport equation. *Nuclear Science and Engineering*, 1989.

[24] J. E. Morel and T. A. Manteuffel. An angular multigrid acceleration technique for s_n equations with highly forward peaked scattering. *Nuclear Science and Engineering*, 1991.

[25] S. Pautz. *Discrete Ordinates Transport Methods for Problems with Highly Forward-Peaked Scattering*. PhD thesis, Texas AM University, 1998.

[26] G. C. Pomraning. The fokker-planck operator as an asymptotic limit. *Mathematical Models and Methods in Applied Sciences*, 1992.

[27] G. C. Pomraning. Higher order fokker-planck operators. *Nuclear Science and Engineering*, 1996.

[28] A. K. Prinja. Charged particle transport. University Lecture, 2012.

[29] A. K. Prinja and E. W. Larsen. *Handbook of Nuclear Engineering*. Springer, 2010.

[30] A. K. Prinja and G. C. Pomraning. A generalized fokker planck model model for transport of collimated beams. *Nuclear Science and Engineering*, 2001.

[31] B. Trucksin. *Acceleration Techniques for Discrete-Ordinates Transport Methods with Highly-Forward Peaked Scattering*. PhD thesis, Texas AM University, 2012.

[32] D. Valougeorgis, M. Williams, and E. Larsen. Stability analysis of synthetic acceleration methods with anisotropic scattering. *Nuclear Science and Engineering*, 1988.

[33] J. S. Warsa. Analytical and numerical transport. University Lecture, 2014.

[34] J. S. Warsa and A. K. Prinja. A moment preserving S_N discretization for one-dimensional fokker planck equation. *Transactions of the American Nuclear Society*, 2012.